University of Nottingham
UK | CHINA | MALAYSIA

In-process monitoring of powder bed fusion with fringe projection

Submitted December 2018, in partial fulfillment of
the conditions for the award of the degree **Doctor of Philosophy.**

Nicholas Southon

Faculty of Engineering

University of Nottingham

I hereby declare that this dissertation is all my own work, except as indicated in the text

Abstract

Additive manufacturing (AM) is a family of manufacturing techniques that are increasingly being used for the production of high performance or highly customised parts. Greater adoption of AM for end-use manufacturing is hampered by unpredictable process outcomes and limitations on both geometry and build orientation. Powder bed fusion is currently used to manufacture end use parts in both metal and polymer, with greater industrial adoption expected. However, it is widely acknowledged in literature that process control and, therefore, process monitoring, are needed to make powder bed fusion more suitable for widespread use in manufacturing. If a defect can be detected during the process, it can either be repaired in-situ or process parameters can be changed to reduce the occurrence of further defects. A record of the detected defects in a part could also contribute to a quality certification procedure for applications with strict certification requirements, such as aerospace part production.

In this work, point cloud data was collected to demonstrate the feasibility of in-process fringe projection measurements of the powder bed surface of laser sintering. Additionally, a fringe projection measurement system was designed to obtain measurements from the powder bed of a high speed sintering machine. Both sets of data were analysed in a similar manner to differentiate between different types of defects and establish indicators of normal processing conditions. However, due to the high dynamic range of the high speed sintering powder bed, only partial comparisons of data could be made with laser sintering.

This thesis demonstrates a novel in-process monitoring system using fringe projection to provide near real-time feedback on the state of the build, potentially enabling process control decisions to be made. This thesis does not demonstrate the calculation or implementation of process control

decisions, but does show how three dimensional measurements of the in-process polymer powder bed can be used to provide high level information about the progress of the build and, therefore, used as feedback for a process control system.

Acknowledgements

This work was supported by the Engineering and Physical Sciences Research Council [grant number EP/M008983/1,EP/L01534X/1]. I am also grateful for the support of both industrial sponsors, BMW Group and Xaar 3D. Their support has been invaluable and it has been a pleasure to collaborate with them.

Working with my university colleagues has enriched my research and I would like to thank academic and technical staff as well as the numerous students I have worked with.

My supervisors, Dr Ruth Goodridge, Professor Richard Leach and Dr Petros Stavroulakis have all contributed to this work and the journey towards it and I am very grateful for their input and support.

My colleagues in both the Centre for Additive Manufacturing and the Manufacturing Metrology Team have welcomed me and introduced me to many things throughout my studies. They are too numerous to name, but I would like them to know that they have made the journey all the more enjoyable. Special thanks go to Joe White, Alex Jackson-Crisp, Mark East and Mark Hardy for ensuring that the experimental work was completed with minimal complications.

I am indebted to my father, Timothy, for proofreading many versions of this thesis. I hope that he will have a much quieter retirement now that my thesis is written.

My wife Jessica and our son Arthur have provided me with a brilliant source of motivation to write this thesis and make sure I can get back to being a husband and a Pappa in time for Christmas. I hope I can show them the same patience they have shown me.

Publications

Journal

N. Southon, P. Stavroulakis, R. Goodridge, R. Leach, In-process measurement and monitoring of a polymer laser sintering powder bed with fringe projection. *Materials & Design* 157 **2018** 227-234.

Conference

A.C.C. Law, N. Southon, N. Senin, P. Stavroulakis, R. Leach, R. Goodridge, Z. Kong, Curvature-Based Segmentation of Powder Bed Point Clouds for In-Process Monitoring. *Proceedings of Solid Free Form Fabrication Symposium* Austin, Texas **2018** 15.

Contents

Abstract i

Acknowledgements iii

Publications iv

List of terms xvi

1 Introduction 1

1.1 Additive manufacturing 1

1.1.1 The seven process categories 3

1.1.2 Improving process quality 7

2 Literature Review 9

2.1 Background on polymer powder bed fusion 9

2.1.1 Processing polymers with powder bed fusion 10

2.1.2 Polymer consolidation dynamics 13

2.1.3 The categories of defects in polymer powder bed fusion 17

2.1.4 Polymer powder bed fusion process parameters . . . 22

2.1.5 High speed sintering (HSS) 24

2.1.6 Process mapping 25
2.2 In-process monitoring 28
2.2.1 In-process monitoring in polymer PBF 29
2.2.2 Categories of in-process data 30
2.2.3 Non-contact form and surface texture measurements of AM surfaces 32
2.2.4 Commercially available in-process monitoring 34
2.2.5 Coaxial monitoring 40
2.2.6 Powder bed monitoring 43
2.3 Fringe projection 49
2.3.1 Underlying mathematical theory 49
2.3.2 Basic phase shifting fringe projection 50
2.3.3 Spatial and temporal phase map unwrapping 52
2.3.4 Calibration 57
2.3.5 Point cloud analysis 60
2.3.6 Conclusion 62
2.4 In-process control 62
2.4.1 In-process control theory 62
2.4.2 Review of In-process control in powder bed fusion . . 66
2.4.3 Conclusion 70

3 Thesis Motivation **71**

3.1 Gap in the knowledge 71
3.2 Research aim 72
3.3 Thesis structure 73

4 In-process monitoring of laser sintering with fringe projection 74

4.1 Experiments 75

4.1.1 Process mapping 75

4.1.2 Fringe projection measurements 79

4.2 Results 82

4.2.1 Process map 82

4.2.2 In-process monitoring 84

4.2.3 Curvature based analysis 93

4.3 Discussion 99

4.3.1 Process insights 101

4.3.2 Segmentation of point cloud data 104

4.3.3 Process signatures 105

4.4 Directions for further research 106

4.5 Conclusion 107

5 In-process monitoring of high speed sintering with fringe projection 109

5.1 Introduction 109

5.1.1 System design 110

5.1.2 System specifications 118

5.2 Methodology 120

5.2.1 Fringe projection measurements 120

5.2.2 Acquisition parameters 120

5.2.3 Build layout 121

5.2.4 Processing parameters 123
5.2.5 Thermal monitoring 124
5.2.6 Tensile test measurements 125
5.2.7 Data management 125
5.2.8 System calibration 126
5.3 Results 127
5.3.1 Calibration 128
5.3.2 High speed sintering build 130
5.3.3 Produced parts 131
5.3.4 XCT measurements 133
5.3.5 Images captured 136
5.3.6 Quality of phase data 140
5.3.7 Phase unwrapping results 140
5.3.8 Point cloud measurements 146
5.4 Discussion 146
5.4.1 Calibration 146
5.4.2 Fringe pattern errors 147
5.4.3 Fringe projection challenges 148
5.4.4 Variation within the HSS build 149
5.4.5 Future improvements 149
5.5 Conclusion 151

6 General discussion and Conclusion **153**

6.1 General discussion 153

6.1.1 Future research 156

6.2 Conclusion 160

References **160**

List of Tables

2.1 Examples of both active and passive monitoring techniques, in PBF, for several data collection regimes 31

2.2 Proposed methods of detecting defects using powder bed surface geometry data. 33

2.3 Commercially available in-process monitoring solutions. In-process monitoring products are not always available across all of a company's machines. 39

5.1 Processing parameters for the HSS builds. 124

List of Figures

1.1 Schematic of a generic LS process. 4

1.2 Schematic of a high speed sintering process 8

2.1 A simplified differential scanning calorimetry trace for a typical semi-crystalline polymer such as polyamide 12 13

2.2 The two main stages of Frenkel-Eshelby sintering. 15

2.3 Porosity in a polymer laser PBF part as measured by XCT. . 18

2.4 The causes and outcomes of necklacing. 19

2.5 A warped HSS part produced in a thermoplastic elastomer. . 20

2.6 Two wavelength coaxial photodiode monitoring offered by Renishaw. 41

2.7 A picture showing the high-speed monitoring system described by Zhang et al. [138]. Figure reproduced with permission. 44

2.8 The geometry of epipolar correspondences in fringe projection. 50

2.9 Wrapped phase from a fringe pattern that repeats five times across the image. 52

2.10 Using a phase map without wrapping to unwrap a higher frequency phase map. 54

2.11 Using phase maps with similar fringe frequencies to create a synthetic phase map with no phase wraps. 55

2.12 One dimensional number theory phase unwrapping. 57

2.13 The effects of phase error on number theory phase unwrapping. 57

2.14 A relationship between projected intensity and measured intensity after gamma calibration. 59

2.15 Process control flowcharts. 64

2.16 The progression of consolidated layers in PBF. 68

4.1 A computer rendering of the ASTM D638-14 Type I tensile test specimen geometry used. 76

4.2 Aerial view of the tensile test specimen locations in the powder bed. 76

4.3 Schematic of an EOS P100 Formiga system. 77

4.4 Representative point cloud from layer 15 of the 17 W build. . 80

4.5 A process map detailing how the failure modes change with both energy density and powder bed temperature. 83

4.6 A plot of ultimate tensile strength against areal energy density at 174 °C. 84

4.7 Height map of the 30th and final layer of a successful build with significant curling, processed at 165 °C, 4 W with a scan speed of 2500 mm s^{-1}. 87

4.8 Height map showing twenty-nine layers of fresh powder after the final sintered layer seen in Figure 4.7. 87

4.9 A profile along the centre of the tensile test specimen, as shown above, processed at 165 °C, 4 W and a scan speed of 2500 mm s^{-1}. 88

4.10 Tensile test specimen at 165 °C, processed at 17 W with a scan speed of 2500 mm s^{-1}. A 0.1 mm to 0.15 mm drop due to sintering is observed. 89

4.11 Mean distance from nominal of consolidated powder. 90

4.12 The data from the 17 W build has the function suggested by Zhang et al. fitted to the first 15 layers of the build. 92

4.13 The evolution of maximum height of the consolidated area for both builds. 92

4.14 Curvature and prominence maps of layer 16 of the build with a 165 °C powder bed surface, 17 W laser power, laser scan speed of 2500 mm s^{-1} and a hatch spacing of 250 µm. 94

4.15 The segmented heightmap of layer 1 of the 17 W build. 95

4.16 The median height map for odd and even layers in the 17 W build. 96

4.17 Height map of a partially consolidated tensile test specimen, powder heaping can be seen around the edges. 96

4.18 XCT slice of a tensile test specimen, produced with a bed temperature of 165 °C, a laser power of 27 W, a scan speed of 2500 mm s^{-1} and a hatch spacing of 250 µm. 97

4.19 Curvature and prominence maps of layer 19 of the 27 W build. 98

5.1 Computer rendering of the fringe projection system showing the optical constraints of the system. 110

5.2 A simplified diagram of the Scheimpflug principle. 113

5.3 The optical distance sensors for triggering the measurement process. 119

5.4 The fringe projection monitoring system attached to the HSS system. 119

5.5 Bitmap used for ink deposition for the first set of geometries built. 122

5.6 Horizontal phase for calibration pose 24. 128

5.7 Co-ordinates for the centres of the white squares on the chequerboard, including interpolated results. 129

5.8 Estimation of extrinsics for calibration. 130

5.9 Root mean squared reprojection error per pose after calibration.130

5.10 Infrared image of the powder bed after the sintering stroke on layer 39 of the build. 131

5.11 Variation of density-artefact density with respect to droplet volume coverage. 133

5.12 Variation of density-artefact porosity with respect to droplet volume coverage. 134

5.13 Variation of ultimate tensile strength with respect to droplet volume coverage. 134

5.14 Variation of tensile test specimen elongation at break with respect to droplet volume coverage. 135

5.15 An overview of the image capture process 137

5.16 Fringe pattern projection errors observed on sinter strokes. . 138

5.17 Fourier space filtering of a captured fringe image for the first powder stroke of stack 7. 139

5.18 Underlying phase noise in captured data. 141

5.19 Number theory phase unwrapping with experimental data, filtered in Fourier-space. 143

5.20 Image of number theory phase unwrapping with experimental data, filtered in Fourier-space. 143

5.21 Number theory phase unwrapping with experimental data, not filtered in Fourier-space. 144

5.22 Image of number theory phase unwrapping with experimental data, not filtered in Fourier-space. 144

5.23 Fourier spectral comparison before and after frequency space filtering. 145

List of terms

Acronyms

2D Two dimensional, in this work often used when referring to traditional images captured by cameras, as opposed to the three dimensional data captured by systems such as fringe projection measurement systems.

AM Additive manufacturing, a group of processes where material is added together, generally layer by layer, to create the final product. This contrasts with common manufacturing techniques such as milling or turning which are subtractive.

CMM Coordinate measuring machine, generally a Cartesian metrology system for accurately measuring points. Commonly used with a physical probe for tactile measurements.

CSI Coherence scanning interferometry, an interferometric microscopy measurement technique where localised interference fringes are used to measure the height of a surface.

DLP Digital light processing, a projection technique that uses an array of micro electromechanical mirrors to selectively turn pixels on and off by reflecting light either through the imaging system or into a heatsink. It is a technique trademarked by Texas Instruments.

DMD Digital micromirror device, a micro electromechanical system consisting of an array of microscopic mirrors that can have their orientation changed between two states by applying an electric charge.

DSC Differential scanning calorimetry, a thermal analysis technique often applied to polymers. A sample and reference are heated simultaneously and the differences between the heatflows provide information about phase transitions and the temperatures they occur at.

FV Focus variation, a measurement technique where a series of images with limited depth of field are used to infer the heightmap of the surface.

GPU Graphics processing unit, a discrete unit (often a coprocessor card) that augments the computer's main processor's handling of large amounts of image manipulation and creation. Initially designed for improving the performance of computer games, they are increasingly being used for general purpose high-speed parallel computing.

HAZ Heat affected zone, the region that is heated by the delivered processing energy. Often larger than the quoted laser spot diameter in laser PBF because the intensity of the laser spot has a Gaussian profile and the diameter contains about 90% of the energy.

HSS High speed sintering, a process that selectively jets a radiation absorbing ink onto the powder bed before illuminating the whole powder bed with an infra-red lamp. Only the areas that have been printed on will consolidate [1].

LS Laser sintering, a common generic term for a polymer PBF process that uses a laser as the heat source for consolidation of the powder bed. Following ISO terminology it would be referred to as polymer laser powder bed fusion. Older literature refers to metal powder bed

fusion as laser sintering. This is rarely correct and generally should be referred to as laser melting or metal laser powder bed fusion.

NN Neural network, a data processing technique that uses layers of linked data processing nodes analogous to brain cells. A training process is required to set up the network for the specific data processing task.

OCT Optical coherence tomography, an interferometry technique that detects subsurface scattering of the measurement laser beam.

PBF Powder bed fusion, a category of AM processes where a focused energy source is used to selectively consolidate regions of the powder bed.

SVDD Support vector data description, a statistical process monitoring technique based on the support vector machine formalism. It finds patterns in the data presented by maximising the difference between different classes of data

TPE Thermoplastic elastomer, a polymer that exhibits rubber-like elastomeric properties as well as being a thermoplastic.

XCT X-ray computed tomography, three dimensional objects are reconstructed from multiple radiographs obtained from different viewpoints using computer algorithms such as back projection.

Glossary

measurand a physical quantity or property that is or will be measured.

microtome to cut a sample into thin sections using an instrument called a microtome. Often used to prepare samples for optical microscopy.

part cake the powder that surrounds the parts being built. Depending on the polymer used and process parameters the part cake can become partially solidified during part creation.

pyrometer a non-contact thermal measurement device that uses optical or infrared wavelengths to estimate the temperature of a surface.

Python A general purpose, high level programming language that is Open Source

sintering the term is normally applied to polymer powder bed fusion where sintering is the act of consolidation in the powder bed. Not to be confused with solid state sintering where atomic diffusion occurs.

Chapter 1

Introduction

This thesis investigates the potential of using 3D in-process measurements of AM processes to quantify the state of the build. In this introduction the processes studied and their main features will be introduced. Following on, the general requirements of an in-process measurement system for the specific processes studied will be outlined along with introductions to relevant concepts.

1.1 Additive manufacturing

As defined by EN ISO/ASTM 52900:2017, AM is the 'process of joining materials to make parts from 3D model data, usually layer upon layer, as opposed to subtractive manufacturing and formative manufacturing methodologies' [2]. Examples of subtractive techniques are milling and turning, whilst formative techniques include rotational moulding and injection moulding.

Subtractive techniques are mainly used at room temperature without the need for an inert atmosphere [3], and are often used to produce close

tolerances and good surface finish [4]. However, depending on the part design, significant material wastage can occur [5].

Formative techniques often rely on plastic deformation of materials which are heated to a liquid state. Producing near net shape parts can be a challenge for some production techniques, although parts can be machined afterwards to achieve desired geometrical tolerances and surface finish [6].

Examples of the general advantages of AM include lightweighting, producing complex structures with multiple functions and customising each individual part produced. Lightweighting is the process of redesigning components or assemblies to save weight. When AM is used for lightweighting of aircraft components, weight savings of 50 % or more are common [7]. Reduced aircraft weight leads to large fuel and cost savings across the lifetime of an aircraft, which is why AM lightweighting is widely reported for aviation applications. The complex structures required for lightweighting can also be optimised to produce structures that have graded properties throughout their volume, enabling complex biomimetic structures to be produced [8]. AM can produce individually customised components at no extra cost, making it attractive for medical applications because every patient's body is different. The global manufacture of in-ear hearing aids has almost completely transitioned to AM because of the economic benefits. Previously, hearing aid shells were handcrafted and now AM enables mass customisation at a lower cost than traditional techniques [9]. However, individual parts have high costs because of minimal economies of scale and slow production [5, 10]. Also, defects can be common unless onerous and stringent limitations of processing variables are maintained [11]. It can therefore be said that AM 'has many more degrees of freedom than other manufacturing processes' but 'if a part can be fabricated economically using a conventional manufacturing process and can meet requirements, then it is not likely to be a good candidate for AM' [12]. If the quality and consistency of AM parts could be

improved, the industrial case for using AM for end-use components would be much stronger.

1.1.1 The seven process categories

When discussing AM, it is useful to refer to the seven AM process categories as defined by EN ISO/ASTM 52900:2017 [2].

- Binder jetting: a ‘process in which a liquid bonding agent is selectively deposited to join powder materials’.
- Directed energy deposition: a ‘process in which focused thermal energy is used to fuse materials by melting as they are being deposited’.
- Material extrusion: a ‘process in which material is selectively dispensed through a nozzle or orifice’.
- Material jetting: a ‘process in which droplets of build material are selectively deposited’.
- Powder bed fusion: a ‘process in which thermal energy selectively fuses regions of a powder bed’.
- Sheet lamination: a ‘process in which sheets of material are bonded to form a part’.
- Vat photopolymerization: a ‘process in which liquid photopolymer in a vat is selectively cured by light-activated polymerization’.

Both AM techniques considered in this thesis are powder bed fusion (PBF) processes. The two different polymer PBF processes analysed are laser sintering (LS) and high-speed sintering (HSS).

LS, the first polymer PBF process, was developed and patented by Dr Carl Deckard in the mid-1980s [13]. First finding use for rapid prototyping

[14], LS has increasingly been shown capable of end-use part manufacture [15] and is the most widely used of the polymer PBF techniques.

LS relies on the consolidation of thin layers of polymer powder through the application of a heat source, a laser spot scanned by galvanometers. The laser provides just enough thermal energy to consolidate the preheated powder bed through melting and solidification of the polymer particles. Each new layer of powder is typically 100 µm thick, spread by either a counter rotating roller or a blade [16]. The part is built up layer by layer and over many hundreds or thousands of layers the part is completed. Post processing consists of removing the part cake (the parts and the surrounding powder bed) and cleaning powder from the surfaces of the parts. A diagram of a typical LS system can be seen in Figure 1.1.

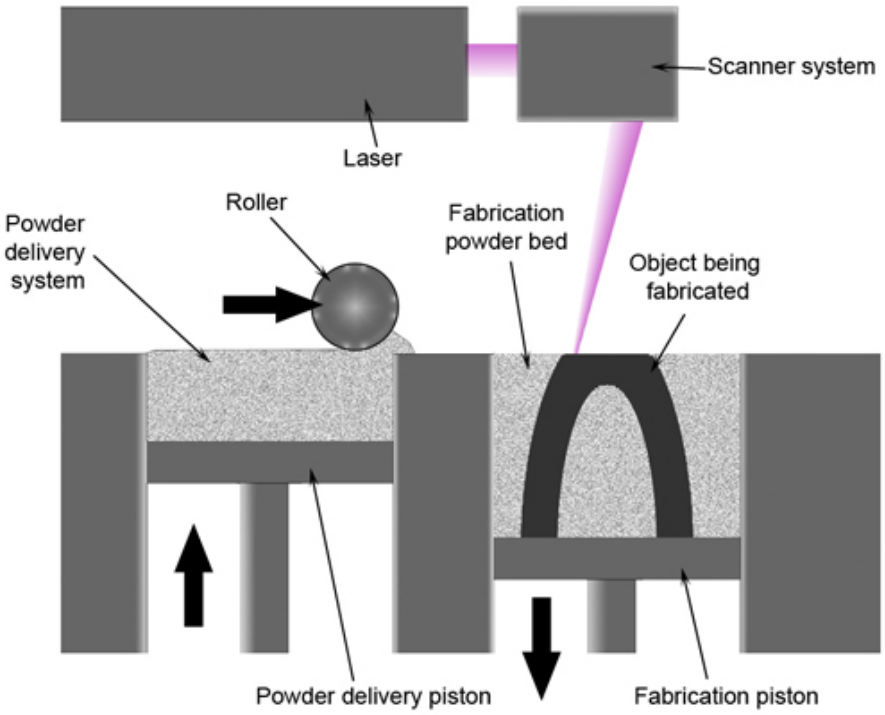

Figure 1.1. Schematic of a generic LS process. A counter-rotating roller is shown for the powder spreading system, but blade based systems are also used. Reproduced with permission from [17].

In the course of part production, thermal stresses can build up and cause

warping and potentially cause build failures [18]. Their magnitude is reduced by pre-heating the powder bed close to the polymer's melting point but there are still some geometries that cause significant warping, such as geometries with large contiguous cross sectional areas [16]. Even if the part is produced without visible issues, there are other types of defects that could be present inside the finished part [19].

In addition to the generic AM advantages such as short lead times and economical suitability for small runs of production, LS requires no support material when building parts. Support material is needed in processes such as material extrusion and metal PBF, to prevent build failure when unsupported overhangs are deposited or consolidated. In metal PBF, supports are also used to reduce warping caused by residual stresses. The unconsolidated powder bed in LS supports overhanging regions that have been consolidated, increasing the range of geometries that can be produced with the technique. However, process instability has a significant impact on the economies of production [10].

HSS is a more recently developed polymer PBF process that selectively jets a radiation absorbing ink onto the powder bed before illuminating the whole powder bed with an infra-red lamp. Only the areas that have been printed onto will consolidate, because the surrounding powder with no deposited ink reflects enough thermal energy to not consolidate [1]. A diagram of a typical HSS system can be seen in Figure 1.2.

HSS was developed specifically to improve upon the economics of series manufacturing of parts with LS [21]. A significant portion of the production cost of each part produced in LS is related to the purchase and maintenance of the LS system, therefore, a consolidation method cheaper than a laser was developed [21]. However, the potential cost reduction offered by HSS is not only predicated on a cheaper consolidation process. The lack of a point scanning energy source also increases the processing speed, thus

further reducing the cost per part through reduced amortisation per part. Jetting radiation absorbing ink, however, introduces new challenges such as maximising the ink's loading of the radiation absorbing material. Also, when a drop of ink lands on the powder bed surface it will spread because of the influence of surface tension. Therefore, the resolution of features that can be created could be lower than suggested by the spacing of droplets on the powder bed. HSS delivers thermal energy to the whole powder bed, instead of just the parts as seen in LS, therefore, the powder bed gets hotter than in LS. This increased temperature of the powder bed can lead to unwanted consolidation of the powder surrounding the parts produced [22]. This is a problem because of the additional post processing required for part removal, as well as increased thermal ageing of the part-consolidated powder [23]. HP have developed a polymer PBF technique similar to HSS called multi-jet fusion, which is commercially available and claims mechanical performance similar to that of LS [24]. If HSS, or processes similar to HSS, can produce cheaper parts at a greater rate, it is expected that they will become more widely adopted by industry.

The wider use of polymer PBF for manufacturing end use parts is partly limited by the variability of the process outcomes [25]. Reducing the frequency and severity of defects will help reduce process variability. The literature shows that in-process monitoring and control are needed to improve the reliability and industrial usage of the polymer PBF process. The task of detecting defects with in-process monitoring requires both knowledge of the monitored process, its parameters and the selection of an appropriate monitoring process.

1.1.2 Improving process quality

Process control can be used to modify process inputs to stabilise and modify the properties of created parts, improving the quality and consistency of parts. AM process control is still in the early stages of development [25, 26], but there are many opportunities over the course of a build to observe the consolidated surface of a layer, and therefore the process state, before it is incorporated into the bulk of the part. There is a measurement opportunity when the powder bed is not covered after consolidation on each layer, before powder for the next layer is spread on top. Optical observations are selected because their measurements are non-contact and can have a sub-millimetre measurement pitch on the powder bed. It should be noted that the analysis of the process monitoring of a layer needs to inform process control decisions before the next layer is processed.

This thesis will focus on implementing and analysing data from a process monitoring system incorporated into polymer powder bed fusion systems. The motivation is to enable comprehensive process control by providing insight into the process state by measuring the powder bed surface in-process.

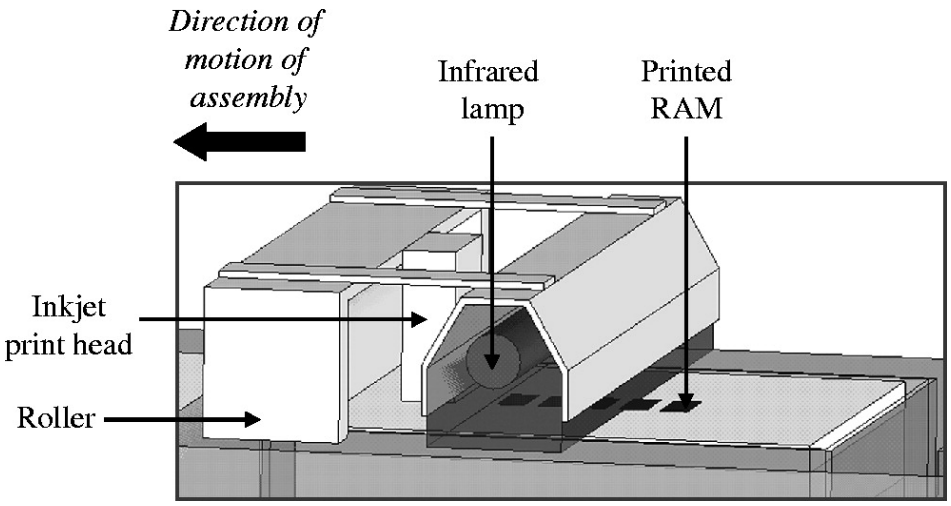

Figure 1.2. Schematic of a high speed sintering process. The powder delivery system is the same as in Figure 1.1. Reproduced from [20] under a Creative Commons Attribution-NonCommercial-No-Derivs license.

Chapter 2

Literature Review

2.1 Background on polymer powder bed fusion

When reviewing the literature for in-process monitoring of powder bed fusion, there are two main areas for consideration. Firstly, an understanding of the process dynamics and the potential defects is required, see Sections 2.1.2 and 2.1.3, before interpretation of in-process monitoring data is possible. This is because preventing future defects or repairing current defects, with future process control, requires an understanding of the root cause of the defects. Secondly, the method of in-process monitoring will depend on the types of defects that need to be detected and the specification of the monitoring solution will define the lateral defect detection resolution, see Section 2.2.

The requirements on the data being produced by the in-process monitoring system are put in the context of process control and, therefore, some background on process control is provided. Finally, in Chapter 3, the gap in the knowledge covered by this thesis will be presented along with the remaining structure of the thesis.

2.1.1 Processing polymers with powder bed fusion

Defects are the result of unsuccessfully processing material, which for polymer PBF is polymer powder. Reviewing the mechanisms of successful material processing in polymer PBF will help identify some mechanisms of defect generation and the morphologies of defects that could be detected by in-process monitoring. The main desirable characteristic when assessing polymers for their suitability for polymer PBF is the ability to successfully produce a part using a wide range of process parameters. The freedom to choose many combinations of process parameters allows optimisation of parameters, such as laser scan speed, or optimisation of process outcomes, such as mechanical properties.

When optimising the process parameters, the thermal ranges the polymers can be processed in are an important consideration. A technique commonly used to quantify such thermal ranges is differential scanning calorimetry (DSC). DSC is a thermal analysis technique where a sample and reference are heated simultaneously and the differences between the heatflows into the samples provide information about phase transitions and the temperatures they occur at. A typical DSC cycle consists of heating the samples from below the glass transition temperature to above melting temperature, followed by cooling the samples back down to the original starting temperature. The two phase transitions illustrated in Figure 2.1 are fusion, when the polymer melts and the polymer chains are are free to move, and crystallisation, where the polymer chains solidify into crystalline regions. The energy released or absorbed in these transitions can be calculated from the area under the DSC curves for the relevant regions, shaded in Figure 2.1. The three main thermal processing ranges of interest are also illustrated in Figure 2.1. The three ranges are the thermal window, the stable sintering region and super-cooling region.

The thermal processing window is the temperature range between the highest and lowest possible powder bed temperatures that still produces acceptable parts, without causing the part cake, see glossary, to consolidate, or the part to warp unacceptably. This range is partly affected by inhomogeneities in the powder bed surface temperature, which can easily reach a 5 ℃ variation across the powder bed [27].

The stable sintering region is defined by Vasquez et al. [28] as the temperature range between the onset of polymer flow and the temperature at which 1% thermal degradation occurs. Wegner et al. [29] reported that keeping the scanned area in this stable sintering region for up to 10 s improves density and mechanical properties. It should be noted that Wegner et al. did not state their calibration routine for thermal measurements or report any errors associated with their thermal measurements, which tracked regions from spherical solid powder particles to hot polymer melt and back to a consolidated solid polymer region with no apparent consideration of changes in emissivity [29].

The super-cooling region is defined by Deckard as the region between the onset of melting upon heating and the onset of recrystalisation on cooling [13]. It is reported that keeping the powder bed temperature in the super-cooling region allows for controlled crystalisation of the whole part when processing is finished and the part slowly cools down relatively uniformly. This should reduce warping due to shrinkage caused by crystallisation. Peyre et al. refer to this region as the work temperature range [30] and Ghita et al. refer to this region as the operating window [31]. The apparent lack of the super-cooling region does not seem to prevent a polymer from sintering [31], but Kruth et al. state that whilst slightly overlapping peaks of melting and recrystallisation could be beneficial for sintering performance, peaks that strongly overlap will prevent a polymer from being able to be processed with polymer laser PBF [32].

Polymers are commonly classified as either crystalline, amorphous or semi-crystalline. A semi-crystalline polymer was chosen as the example in Figure 2.1 because semi-crystalline polymers form the majority of polymer PBF materials, namely polyamide 12 [16]. Semi-crystalline polymers contain both crystalline and amorphous regions, giving them some of the properties of both. Crystalline polymers or regions are rigid, do not elongate and shrink significantly upon recrystallisation. Amorphous polymers or regions do not exhibit a melting point, merely exhibiting increased melt flow beyond the glass transition point. Therefore, considering the processing possibilities of an amorphous polymer does not require the same scrutiny of recrystalisation dynamics. However, when processing amorphous polymers the powder bed cannot be kept at a temperature above which the melt flow will cause powder flowability issues. If this happens, the powder becomes ‘sticky’ which causes problems with spreading new layers of powder. Because of the several competing thermal considerations, experimentation in the specific processing machine is commonly required to define the suitable processing temperatures.

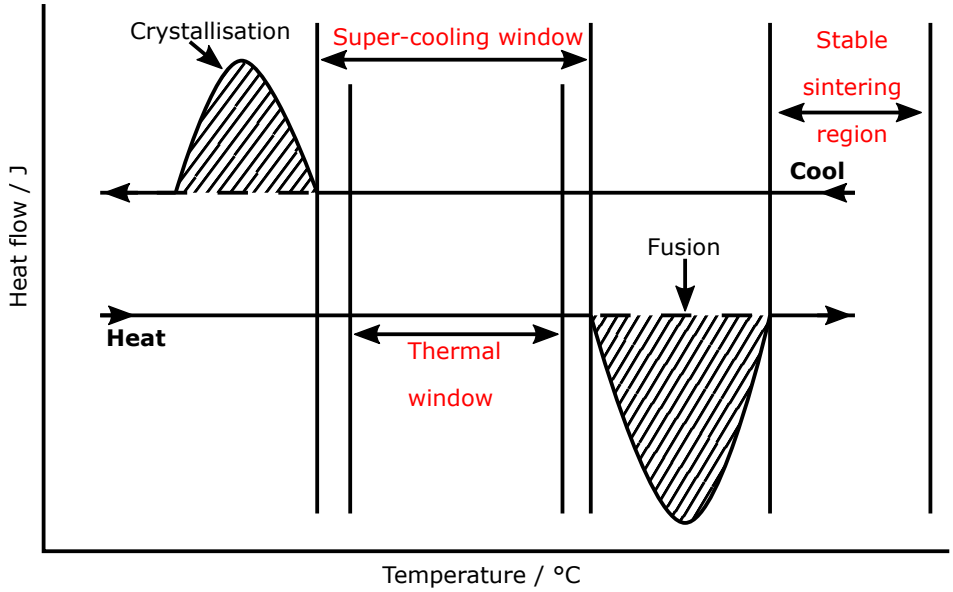

Figure 2.1. A simplified DSC trace for a typical semi-crystalline polymer such as polyamide 12. The low temperature boundary of the thermal window is the temperature at which the powder bed is too cold for sintering because all builds will fail due to curling caused by excessive differential cooling and/or shrinkage caused by recrystallisation. Adapted from Vasquez et al. [33]

2.1.2 Polymer consolidation dynamics

Polymer PBF is a dynamic process and simply selectively heating the powder bed to the ranges discussed above is not enough to consolidate a part. Successful consolidation fundamentally requires molten polymer particles to flow into the gaps in the powder bed, so if the melt viscosity is too low it can lead to greater rates of shrinkage and geometrically inaccurate parts [32]. However, a higher molecular weight and, therefore, increased melt viscosity, increases mechanical performance [34]. The compromise between the mechanical properties of the bulk polymer and the ability to consolidate because of a low enough viscosity led Kruth et al. [32] to suggest laser PBF polymers have an optimum molecular weight range.

Predicting the optimal molecular weight range in advance requires a predictive model of polymer sintering. The first analytic description of particles melting into each other was by Frenkel [35] in 1945. He considered two circular liquid drops of equal size, touching at time $t = 0$. This initial situation

is illustrated in Figure 2.2a. By conserving the total volume of the system and considering the forces driving coalescence, Frenkel derived an equation for the evolution over time of the angle marked θ in Figure 2.2b. It can be seen in Figure 2.2b that as the particles coalesce the 'neck' between them grows in size and θ grows too. The equation for the evolution of θ over time is

$$\theta^2 = \frac{3}{2}\frac{\sigma}{a_0\eta}t \tag{2.1}$$

where θ is the angle shown in Figure 2.2b, σ is the surface tension of the liquid, a_0 is the initial drop radius, η is the liquid's viscosity and t is the time since the onset of sintering. Transforming equation (2.1) into a more convenient form requires using the small angle approximation to state $sin(\theta) = \frac{y}{a} \approx \theta$ and, therefore,

$$\frac{y}{a} = \sqrt{\frac{3}{2}\frac{\sigma}{a\eta}t} \tag{2.2}$$

where y is the sintering neck's width, see Figure 2.2b.

The small angle cosine approximation is used twice in the main derivation of the Frenkel equation, so care must be taken for angles greater than approximately 40°. This is a consequence of the small angle sine approximation having a 10 % error at this angle, whilst the cosine approximation error has a relative error of about 2 % for that size of angle.

With equation (2.1) in the commonly quoted form of equation (2.2), the evolution of y/a with respect to time can be plotted to investigate the effects of surface tension and viscosity. In 1949, in the discussion section of Shaler's written notes of a seminar on sintering, Eshelby proposed a more rigorous derivation which improved on Frenkel's derivation by conserving the condition of incompressibility of the fluid [36]. This leads to an equation very similar to equation (2.2)

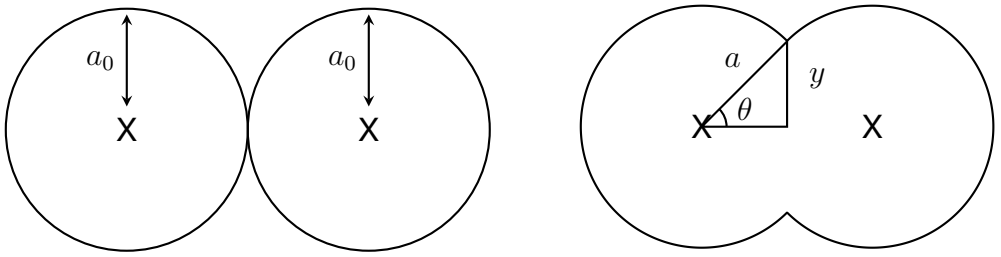

(a) Initial position of sintering. **(b)** Half way point of sintering.

Figure 2.2. The two main stages of Frenkel-Eshelby sintering. The point of contact between the two droplets is a sharp bend and the radius of the spheres, a, increases as coalescence progresses.

$$\frac{y}{a} = \sqrt{\frac{\sigma}{a\eta}t}. \tag{2.3}$$

It should be stated that equation (2.1) was only ever conceived as being valid for the first stage of sintering, ending at the point shown in Figure 2.2b, because pore closing dynamics are the dominant regime once the pores become disconnected. Frenkel states that disconnection of pores happens at the end of the first stage [35].

Models more complex than Frenkel's have been proposed that closely predict the two-particle coalescence; notable examples are Bellehumeur et al. [37]; Pokluda et al. [38] and Balemans et al. [39]. There is only one reported set of measurements of the actual rate of sintering with near in-process conditions, see [40]. Steinberger et al. used a laser beam with an angle of incidence of 76.5° and exposure times of approximately 300 ms to study the rate of consolidation of the polymer powder bed [40]. It is unclear how comparable the results are for conditions in the polymer powder bed in modern commercial systems as in-process measurements of drop due to consolidation have not been reported. Despite the progress made since Frenkel's seminal work, and Eshelby's correction, it is common for experimental polymer PBF literature to use the Frenkel-Eshelby model when discussing consolidation times or comparing hot-stage melting experiments to theory. This is probably because the Frenkel-Eshelby model is simple

to state and easy to manipulate. For example, to find an estimate for the consolidation times Peyre et al. set $y/a = 1$ in equation (2.3), but referred to it as the Frenkel model, yielding

$$t_C = \frac{a\eta}{\sigma} \tag{2.4}$$

where t_C is the time for full consolidation [30]. These estimates are likely to be inaccurate because of the several small angle approximations used, but there is no mention of this caveat in Peyre et al. In contrast to Peyre et al., it is stated in Shi et al. [18] that full sintering occurs when $y/a = 0.5$, but it is unclear what the evidence for this statement is. Haworth et al. [41] use the Frenkel-Eshelby model to simply demonstrate the large effect that the polymer melt viscosity has on the rate of sintering, by plotting the evolution of y/a. A further explanation for continued use of the Frenkel-Eschelby model is that the temperature profile in polymer PBF is not isothermal (a general assumption of many analytic models), so using fixed values for the polymer melt's surface tension and viscosity may well cause as many inaccuracies in these analytic models as the small angle approximations.

Therefore, the Frenkel-Eschelby model appears to give an acceptable approximation of the timescales required to sinter a polymer, which helps to inform polymer grade selection. It is clear from the approximate timescales quoted in the literature, and the limited experimental data, that full consolidation in polymer powder bed fusion happens over the course of at least 1 s [41], many orders of magnitude longer than the laser-polymer interaction time of at least 10 µs [18]. Steinberger et al. used laser interaction times of 300 ms and 400 ms in their experiments, but this does not appear to be representative of modern systems.

2.1.3 The categories of defects in polymer powder bed fusion

In this thesis, the term defect refers to a non-designed feature or imperfection in the built material. Defects have the potential to exist in any manufactured part, but the quantity and impact of defects in polymer laser PBF parts makes defect detection and prevention an important part of the processes. For a detailed overview of typical classes of metal powder bed fusion defects and the literature on measuring them in-process see Grasso and Colosimo [25], Everton et al. [26] and Spears and Gold [42]. When discussing defects and their detection, quantitative metrics are useful. A quantitative methodology for quantifying the capabilities of defect detection is outlined in Hirsch et al. [43]. Their suggested comparison metrics are based on the time penalty of capturing in-process measurements and the defect detection spatial resolution of the measurement process.

Porosity

Control over the porosity of polymer PBF parts is critical for manufacturing reliable components for end use with good mechanical properties [44]. Porosity consists of voids in the bulk consolidated material of the part, which can have more than one cause. However, the most likely causes of porosity in polymer PBF are insufficient fusion for full consolidation, thermally aged powder with too high melt viscosity, or gas trapped in the polymer melt [45]. See Figure 2.3 for an example of pores in a polymer PBF part. Porosity can dominate the mechanical properties of the bulk consolidated material [44], but there is no consensus on the formation and location of pores. Stichel et al. [45] stated that whilst co-planar pores were present in almost all samples tested, the pores did not form at layer boundaries. Pavan et al. [46] reported porosity periodicity in the build direction as having characteristic

length scales of one or two layers, but they did not explicitly state if the pores measured were concentrated at layer boundaries. They did suggest pores would be located on layer boundaries, but that was based on simulation results that show a clear thermal gradient, with the bottom of each layer being cooler than the top [47]. The pore formation mechanism suggested in Stichel et al. is bubbles rising through the polymer melt being pinned in place by the non-molten cores of some particles. Non-molten cores were observed to have co-planar alignment, which would explain the spatial periodicity of pores that are not concentrated at layer boundaries.

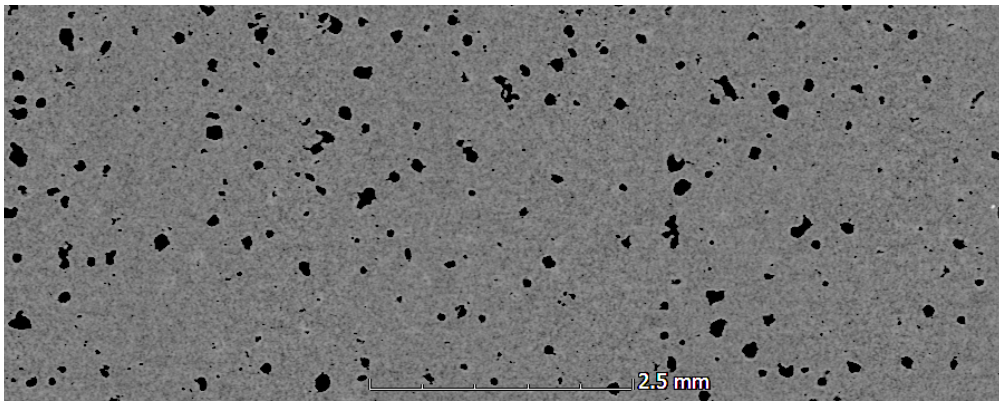

Figure 2.3. Porosity, dark regions, in a polymer laser PBF part as measured by XCT. The high porosity is due to the excessive laser power used for the build.

Degree of particle melt

The extent of non-molten particle cores in a processed part is known as the degree of particle melt [20]. It has been shown to correlate with ultimate tensile strength and elongation at break [20], and can be measured with DSC of a sample of the produced part to measure the relative size of melting peaks. Degree of particle melt can also be seen in microtomed samples [45], by looking for cores of polymer that do not exhibit the spherulite crystal structure. However, degree of particle melt is not a defect detectable by in-process monitoring of the powder bed unless a surface penetrative technique is used that can detect the change in crystal structure. Indirect

measurements of the amount of consolidation are unlikely to be successful since Stichel et al. [45] reported no clear correlation between non-molten cores and porosity and, therefore, density.

Lack-of-fusion

Non-molten cores are not the only possible defects caused by imperfect consolidation of the powder bed. Lack-of-fusion defects can also be caused by poorly optimised laser scan paths, where a curved scan path intersects with a region of hatched paths for scanning the bulk of the part [48]. A diagram of necklacing along with examples from a part can be seen in Figure 2.4.

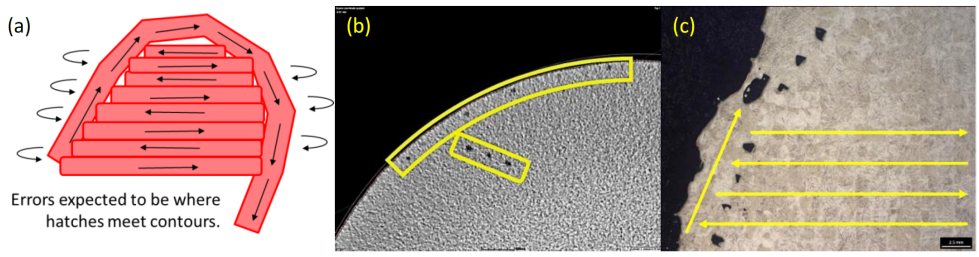

Figure 2.4. (a) Diagram of how necklacing can arise through errors in path overlap (b) necklacing observed in an X-ray computed tomography (XCT) scan of a part produced at 70 % of the recommended power (c) optical micrograph of necklacing errors in a part built with recommended parameters. Figure reproduced with permission from Foster et al. [48].

Surface texture

Final part surface texture can impact the end user's perception of an AM part [49]. In polymer PBF, using a high percentage of recycled powder can lead to increased surface roughness in a phenomenon known as 'orange peel' [23]. The recycled powder has an increased melt viscosity because of polymer degradation caused by thermal ageing by being in the powder bed during processing [50], notably hydrogen bonding cross-linking causing

chain growth [32, 51, 52]. Increased melt viscosity means the rate of consolidation reduces, following the Frenkel-Eshelby model of equation (2.3). Some post-process measurements of surface texture have been briefly compared on laser sintered parts [53]. Whilst surface texture measurements have been demonstrated using techniques which could be implemented in-process, [54–56], they have not been demonstrated in-process. As excess particles stick to the outside of the consolidated part during processing, it is expected that in-process surface texture of the consolidated region will be less than that measured post-process [55].

Warping

The high thermal gradients possible in polymer PBF can lead to warping, resulting in build failures due to the recoater mechanism interacting with the sintered part. Figure 2.5 shows a successfully built but warped polymer PBF part. Three factors contributing to warping have been identified in the literature: densification, shrinkage upon cooling and and thermal differentials causing differential stress [57, 58]. Mitigation strategies for warping include increased powder bed temperatures, part re-orientation and multiple low-power laser scans [59]. Whilst increased powder bed temperatures can reduce warping, they can also degrade the polymer in the powder bed and limit powder recycling possibilities [16].

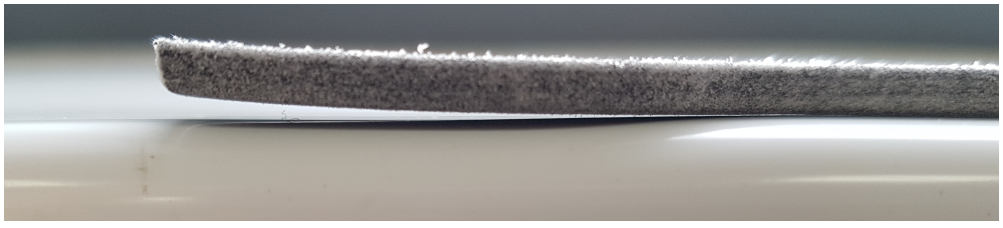

Figure 2.5. A warped HSS part produced in a thermoplastic elastomer. The part is 3.2 mm thick.

In-plane distortions

Geometric deviations from specifications in polymer PBF can be difficult to predict, and most approaches to counteract this involve the optimisation with design of experiments [60] or Taguchi methods [61], discussed further in Section 2.1.6. In this work, geometric distortions are separated from warping because the out-of-plane distortions of warping require different detection mechanisms (e.g. depth sensing measurements) to the in-plane distortions of geometric deviations (e.g. 2D imaging of the powder bed). Also, warping can cause a build failure which potentially damages all parts in a build, whereas geometric deviations are likely to only affect the acceptability of the individual part involved.

Quantifying the fidelity of geometric replication is commonly measured with a artefact consisting of multiple categories of features at different sizes and suitable for measurement with a high accuracy measurement technique such as a CMM [62]. The successful reproduction of features informs design guidelines for specific material-machine combinations [63]. Part orientation and process parameters are the main variables responsible for geometric deviations, but design choices such as machining post-process can mitigate their effect. It should be noted that commercial software for predicting part distortions before building are available, but currently only for metal PBF systems [64–66].

Powder flow

Successful processing requires each new layer of powder to be both thin enough and evenly spread, so the powder flow is important [16]. Poor powder flow results in an uneven surface and is likely to prevent the beginning of the build, as well as being detrimental to mechanical properties of produced

parts due to the reduced powder bed density. Therefore, whilst not a defect, poor powder spreading can have a negative impact on the PBF process.

There is some limited quantitative evidence to show that powder flowability of a pure polymer will decrease when the chamber temperature increases [67]. However, it is also the case that polyamides are hygroscopic to varying extents and that an increase in chamber temperature to above 100 ℃ can drive off absorbed water [28], presumably improving the material flowability since moisture can have a negative impact on powder flowability [68].

2.1.4 Polymer powder bed fusion process parameters

Whilst there are several processes under the umbrella term of polymer PBF, LS is the most common technique in the literature and will be the focus of literature presented. There are over 50 input process parameters with interdependent influences on outcomes [42] but there are three main process parameters that are commonly used to describe builds. These are laser power, laser scan speed and laser hatch spacing. Often only laser power and laser scan speed are varied when investigating the effects of delivered energy on mechanical properties of produced parts [28, 69, 70]. Laser scan strategies, laser spot size, temperatures of the powder bed and the powder bed surface, laser wavelength, and powder layer thickness are commonly optimised for the material being used and are unlikely to change significantly between builds if difficult to produce features such as thin walls are not introduced or removed between builds.

Even with a suitable polymer grade designed for use in PBF it can be a time consuming process to find the best combination of parameters for the specific machine used. Examples of such investigations from literature rarely sample the whole parameter space possible for building parts and often

only investigate parameter combinations close to the optimum combination [28, 69–71]

Measurements of parts after the process, beyond the standard tensile test procedures [72], can be used for evaluating the success of the parts produced at specific combinations of parameters. These evaluations can then be fed into formalised optimisation strategies such as Taguchi evaluated with ANOVA [61, 71]. Evaluation of processing success through statistical techniques is a well studied field of research. The evaluation often requires post-process measurements of external features of parts to inform the measurement of process success. External measurements of parts are most common because internal measurements by techniques such as X-ray computed tomography are generally slow and expensive. However, information gained from X-ray computed tomography includes measurements of porosity distribution in polymer PBF parts as well as a potential mechanism for their spatial distribution [45]. One example of external measurements post-process can be found in [53]. Launhardt et al. used both tactile and optical surface texture measurements of a laser sintered surface, with focus variation microscopy found to produce surface texture parameters most comparable to tactile probing of the surface [53].

Computer simulations of the PBF process can be used to predict process outcomes in advance, reducing the number of physical experiments and measurements required to optimise processing parameters [47, 73]. Simulations can also predict physical properties such as temperature in locations and on timescales that are impractical to measure. However, simulations can require large amounts of computational power and they can not predict the outcomes of process variability. For the locations and timescales that are accessible to measurements, in-process monitoring of PBF, covered in section 2.2.1, can provide detailed information about the evolution of the process.

2.1.5 High speed sintering (HSS)

HSS was patented in 2004 and first described by Hopkinson and Erasenthiran [21]. The process combines some of the features of binder jetting with the thermal consolidation of PBF. The motivation for the development of HSS was to find a polymer PBF process that could produce parts faster using less expensive equipment than laser PBF. By removing a laser and galvanometer scanning system, HSS improves the economics of producing large runs of AM polymer parts. Instead of the scanning laser spot in laser PBF, HSS selectively jets a radiation absorbing ink onto the powder bed. The whole powder bed is then irradiated with an infrared lamp, but only the regions of powder with the ink will absorb enough thermal energy to melt and consolidate. Multijet fusion is a similar process that has been commercialised by HP and introduces a detailing agent that is jetted around the border of the part to inhibit oversintering of the consolidated region [74].

From a polymer processing perspective, the main difference between HSS and LS is the linear heating provided by the consolidation lamp. This eliminates hatch strategy considerations and potentially reduces thermal stresses by heating more of the consolidated region at the same time. The extended, roughly 1 s, heating time of the consolidated region appears to improve mechanical properties [75]. Any issues with jetting of the radiation absorbing ink can be categorised as a lack-of-fusion defect, even if the source is dissimilar to lack-of-fusion defects in polymer laser PBF. Apart from the consolidated region being dark, which might cause problems for optical measurements, HSS is expected to be as equally amenable to in-process monitoring as polymer laser PBF. It is also expected that indications of process state in polymer laser PBF will also be present in HSS. This is because the powder beds are very similar between both processes, as are the consolidation dynamics. Despite the similarities of the process powder beds, in-process monitoring of HSS has not been reported in the literature.

This is probably because of the historical lack of commercial HSS systems.

2.1.6 Process mapping

In-process measurements of a polymer PBF powder bed need to be made in the context of determining the appropriate process parameters and evaluating process outcomes. Increasing understanding of the impacts that process inputs (for example temperature or processing time) have on process outputs (for example mechanical strength or geometric accuracy) is a common goal when optimising an industrial process. This type of analysis can also provide academic insight into the dominant mechanisms underlying the process. A process map is one way to visualise the information gathered about a process's response to inputs [76, 77].

A process map is defined as a record of the combination of input parameters and outputs with the goal of detecting which ones lead to specific process outcomes such as a successful build or a build failure due to curling. Within the region of successful processing, quality envelopes can be defined by contours of constant part quality [78]. Other visualisations similar to process maps include process diagrams [79], processing window [80] or simply the variation of a process output with the variation of single or multiple input parameters [28, 80].

However the data is recorded and visualised, an efficient input parameter selection protocol is required to reduce the number of experiments needed to obtain a clear understanding of the process as it is impractical to record all combinations of inputs. To this end, efficient sampling and analysis of input parameter selection is a well studied problem and the most common solutions in literature include Taguchi methods, response surfaces and analysis of variation (commonly known as ANOVA) [81–83]. It is possible to combine Taguchi methods, response surfaces and ANOVA to gain maximum insight

into optimal processing conditions and the interdependence of parameters. Whilst all the discussed process mapping literature evaluated the process outcomes, the same analysis techniques could be applied in-process to measurements of the process state.

Another application of process mapping is to investigate the variability of outcomes even when nominal processing conditions remain constant. Some potential sources of such variability are powder bed surface inhomogeneities, laser variation and temperature variation across the build volume. Powder bed surface inhomogeneities can arise from poor powder flowability during spreading [16] and laser absorption variations of approximately 10 % have been simulated for realistic metal PBF scenarios, with correctly spread powder [84]. Modulation of laser output power is accounted for in some commercial metal PBF systems [85]. Variation of temperature across the powder bed is a widely reported issue in polymer PBF [16] and can lead to improper consolidation because the amount of energy required for correct consolidation is dependant on the initial temperature of the polymer before processing. Whilst process mapping provides an estimate of variability, only in-process monitoring can account for it during the process.

A disadvantage of almost all of the formalised ‘design of experiments’ methodologies is the focus on rectangular regions of the process map. That is to say a process parameter range is chosen and all combinations of these parameters could be tested, depending on the completeness of the sampling. This can cause problems when the extremes of two or more parameter ranges enter into a process map region associated with process failure. If build failures are to be avoided, the parameter ranges and the coverage of the process map must be limited.

Process mapping literature for polymer PBF is common, but each report generally focuses on a relatively novel polymer. Therefore, the number and breadth of comparable process maps of the commonly processed nylon

polymer for polymer PBF is small given the wide usage, and it is desirable to collect mechanical property and build outcome information across as broad a range of parameters as possible.

In the literature, it is common to vary both laser power and laser speed together to obtain a broad range of delivered energy densities [28, 69, 70]. Energy density, also known as the Andrew number, is a frequently used measure of delivered energy in PBF [86, 87]. Despite being a common metric to compare different process parameter combinations, there are various issues with energy density as a normalising value. Firstly, the areal energy density parameter is generally used since layer height is commonly kept constant in experiments, but varying layer height will invalidate comparisons based on areal energy density. Dividing the areal energy density by the layer height gives the volume energy density, the measure of delivered laser irradiation per unit volume. Using the volume energy density corrects for layer height variation, but it still does not address fundamental issues with the complexities of the process, such as varying thermal properties between materials, that are ignored when only the laser energy input is considered. Energy density proves a popular normalising value because collapsing two-dimensional parameter variations into a single value creates clearer graphs. However, two sets of process parameters with equal energy density can lead to two different processing outcomes. Additionally, different materials cannot be easily compared due to the variations in required energy delivery to melt the powder bed. The inability to make simple comparisons across materials reduces the utility of previous material studies for new materials. It is also worth noting that processing with multiple laser passes cannot be completely captured with energy density because heat loss is not taken into account. This shows that energy density is an incomplete reduction of the energy delivery process into a single value [86]. Hann et al. [88] proposed normalising with respect to enthalpy and melt pool

depth for laser welding. The utility of their approach has been validated for experimental and simulated laser melting data [89]. However, if only scan speed, laser power and hatch spacing are varied, energy density can be useful as a normalised value with which to compare properties across various builds. These energy density comparisons allow a wide range of process parameters to be considered when optimising builds.

2.2 In-process monitoring

In-process monitoring is essential for any manufacturing process with the importance increasing for processes with narrow operating parameter ranges [90]. With a firm understanding of process dynamics, in-process monitoring coupled with in-process control can apply the information acquired by full process mapping in real time to improve part quality and account for process variability. Closed-loop control is using the process state data from in-process monitoring to control the process parameters and therefore improve the process. If the parameter modification happens during the process, it is in-process control, which is discussed in Section 2.4.

Process monitoring is defined by Stavropoulos et al. as ‘the manipulation of sensor measurements (e.g. force, vision, temperature) in determining the state of the process’ [91]. It is vital that in-process monitoring should provide at least the same quality of information as an experienced user observing a process. This critical quality requirement allows for more effective use of operator time, and reduces processing costs. Once the state of a process is known, manual or automatic modifications of process parameters can be made through process control if needed, see Section 2.4. Machining is an example of a manufacturing technique where mature applications of process monitoring can be found [91–93].

It is desirable for process monitoring not to interrupt the manufacturing process as any reduction in productivity could counteract the benefits of monitoring. Therefore, the speed of data acquisition is another critical requirement of in-process monitoring. The speed, sensing area, sensing mode, precision and environmental requirements are very important when considering which monitoring techniques to use. For polymer PBF, the sensing needs to be non-contact because the environment is hot and dusty, the region of interest needs to be at least $100\,\text{mm} \times 100\,\text{mm} \times 1\,\text{mm}$, to cover a significant fraction of a standard polymer PBF print bed surface [16], and the standard deviation of height variations expected of the measured surfaces is approximately 60 µm [94].

2.2.1 In-process monitoring in polymer PBF

The in-process monitoring of metal PBF is widely reported in literature and methods of both process monitoring and process control can be applied to polymer PBF. Therefore, metal PBF literature is included in this review of the state of the art literature for in-process monitoring and control.

In-process monitoring techniques can be separated into two broad categories, Lagrangian and Eulerian [42]. The terms originate from fluid dynamics, and in this context they refer to the reference frame used to monitor the powder bed. The Lagrangian monitoring approach uses a frame of reference that moves with the heat source since that is the region where processing of the powder bed occurs. This is analogous to the laser spot on the powder bed being a fluid parcel travelling through the space and time. This makes the monitoring of the powder bed the Eulerian approach. Lagrangian data collection requires a very high acquisition rate to scan across the whole powder bed, in the order of metres per second, before a new powder layer is spread. The complexities of scanning the field of

view across the powder bed can be partially avoiding by integrating sensing into the optical path of the laser scanning system used for powder fusion. This also ensures the data is always obtained synchronously with the movement of the heat affected zone (HAZ) across the powder bed. However, the information is only ever obtained with the HAZ, so defects that develop after the HAZ has passed will not be detected. The Eulerian monitoring approach uses a frame of reference fixed to the machine that often covers the whole powder bed, though some sensors, such as pyrometers, only observe a small portion of the powder bed. Eulerian monitoring is ideally suited to observing defects across the whole powder bed, including thermal inhomogeneity and defects in the surface of the powder bed. However, there are optical challenges in measuring a whole build area (typically about 300 mm on each side) to a suitably high resolution, with particle-level lateral resolution requiring a pixel pitch of 50 µm or less on the powder bed. For the recently described technique of projection sintering [95], the two monitoring approaches are identical, since the heat source is stationary and the whole layer is consolidated at once.

No single process monitoring technique can provide perfect information about the state of the PBF process. However, the two main categories of Eulerian and Lagrangian monitoring provide a useful framework for discussing the different types of in-process data possible.

2.2.2 Categories of in-process data

PBF is a complex process with many in-process measurements possible. The choice of monitored quantity determines what aspects of the process state can be determined. For example, if the temperature of the powder bed is measured after consolidation, warping of the part might be indirectly inferred from significantly colder edges of the consolidated region. How-

ever, powder spreading irregularities are unlikely to be detected. Within the broad in-process measurement data categories of thermal, optical, acoustic sensing, there are large differences between data collected with active or passive emission. Table 2.1 gives some examples of active and passive data collection in the literature.

Category of Data	**Passive emission**	**Active emission**
Thermal	Thermal camera taking pictures of the powder bed [96, 97] Thermal in-line with laser beam [99–101]	Flash thermography of consolidated regions [98]
Optical (qualitative)	Images of the powder bed, potentially with machine learning [67] Meltpool emissions monitoring [104]	Dark field imaging [102, 103]
Optical (quantitative)	Photogrammetric reconstruction of the powder bed surface [105]	Fringe projection [106] In-line white light interferometry [107, 108]
Acoustic	Acoustic emission monitoring [109, 110]	Laser ultrasound [111] Spatially resolved acoustic spectroscopy [112]

Table 2.1. Examples of both active and passive monitoring techniques, in PBF, for several data collection regimes

Because of the possibilities of polymer chain degradation during PBF processing, it is important to be aware of the effects of thermal history on both unprocessed powder and consolidated regions. One consequence

of thermal history is that the proportion of recycled powder used needs careful monitoring as it can adversely affect parts produced [16, 41]. For consolidated regions, the thermal history can predict mechanical properties [29], demonstrating the importance of thermal monitoring in polymer PBF.

From Table 2.2, it can be seen that most of the listed defects can be measured with geometric monitoring of the powder bed surface. Quantitative information on the powder bed surface also allows for process signatures, such as drop due to consolidation, to be measured. Therefore, quantitative geometric monitoring of the powder bed surface was chosen for its wide range of detectable defects as well as suitability for measuring drop due to consolidation. Drop due to consolidation is an important process signature because it is a direct measure of the degree of consolidation.

2.2.3 Non-contact form and surface texture measurements of AM surfaces

Measurements are often categorised as form measurements or surface texture measurements. Form measurements are of the macroscopic geometric form of a part whilst surface texture measurements are measurements of the surface of a part, ignoring the contribution of form to the measurement. There are numerous non-contact form and surface texture measurement techniques that warrant consideration for geometric in-process monitoring of the polymer PBF powder bed. A brief overview of such techniques and their uses for measuring AM surfaces will be followed by a more detailed introduction to the theory and literature of the chosen measurement technique.

Notable measurement techniques used to study PBF surfaces ex-situ include XCT [45], focus variation (FV) and coherence scanning interferometry (CSI) [113, 114]. XCT can measure both internal and external surfaces

Defect	Morphology	Measurand
Porosity	Pores in the bulk of the part, likely under the in-process surface	Drop due to consolidation
Unmelted cores	Unmelted cores of particles in the bulk of the part, likely under the in-process surface	Unlikely to be measureable
Final part roughness	Surfaces of parts are not smooth	Agglomeration of particles on the edges of consolidated regions
		Solidified polymer melt surface is rough in-process due to high over recycling of powder
Geometric deviation	Part is distorted from nominal in the x-y plane	Agglomeration of particles on the edges of consolidated regions
Warping	Consolidated region protrudes above the powder bed	Height of regions that are expected to be consolidated
Local overheating	Consolidated region has areas of significantly higher temperatures	Spatial distribution of surface temperature of the powder bed
Powder spreading irregularities	Powder bed surface has streaks left by recoater	Height variations across the powder bed

Table 2.2. Proposed methods of detecting defects using powder bed surface geometry data. Defect categorisation is taken from section 2.1.3

[115, 116]. This unique capability makes the technique desireable for post-process measurements of complex parts produced by AM, despite the slow and expensive nature of XCT measurements [117]. However, it would not be feasible to incorporate an in-process monitoring X-ray CT based imaging system similar to the synchrotron and laser powered systems reported in literature [118, 119], mainly for reasons of geometrical constraints and the complexity of measuring from sufficient viewpoints for three dimensional reconstruction. FV measurements of AM surfaces have also been investigated, with a detailed study of the effect that acquisition settings have on the measured surface [120]. As well as being rough like polymer parts, metal AM parts have varying surface reflectivity which can complicate measurements. Though historically not suited for measuring surfaces such as metal AM parts, CSI has been shown capable of high quality surface measurements when techniques such as oversampling are used [121]. The optical measurements mentioned share short working distances and small fields of view similar to that of an optical microscope. Therefore, whilst these techniques are capable of post-process measurements, they are not suitable for in-process monitoring because of the requirements for high speed measurement and not blocking the optical access to the powder bed.

2.2.4 Commercially available in-process monitoring

Before discussing the many possible ways of monitoring the polymer powder bed, it is useful to briefly mention the commercially available in-process monitoring solutions for PBF. Table 2.3 shows an overview of the currently available in-process monitoring in industrial systems. For clarity, systems which monitor the environmental parameters (chamber temperature, powder bed surface temperature, oxygen content, etc.) have been excluded. Also excluded were systems that provide a live view of the machine

powder bed for qualitative monitoring purposes without any quantitative information.

Company	Product name	Monitoring technique	Notes
Addup	N/A	Likely laser power monitoring, a camera and gas sensors	Monitoring of 'lasing, layering, inerting'
Arcam (GE)	LayerQam™	High res camera	Tracks porosity
	xQam	X-ray detection	For autocalibrating electron beam
Stratonics (3rd party)	ThermaViz Melt Pool Sensor	2 wavelength high speed CMOS camera	Co-axial or stationary, 1000 ℃ to 2500 ℃
	ThermaViz Global Heat Flow Sensor	Thermal camera	1000 ℃ to 2500 ℃ (lower resolution than meltpool camera)
Trumpf	TruPrint Powder Bed Monitoring	Dark field imaging	

Table continued

Company	Product name	Monitoring technique	Notes
	Truprint Melt Pool Monitoring	Presumed coaxial photodiode	
3D Systems	DMP Vision	2D camera	Information is provided to the user, no automatic decisions are made
	DMP Meltpool	Presumed coaxial photodiode	Information is provided to the user, no automatic decisions are made
Renishaw	LaserVIEW	Coaxial photodiode	
	MeltVIEW	2 coaxial photodiodes	NIR and IR wavelengths
SLM Solutions	Melt Pool Monitoring	2 coaxial photodiodes	Different wavelengths, possibly same ranges as Renishaw?

Table continued

Company	Product name	Monitoring technique	Notes
EOS	EOSTATE Exposure OT	sCMOS NIR or IR (unclear)	Heat distribution of processed layers can apparently be measured
	EOSTATE Meltpool	Coaxial and non-coaxial (photodiode?)	
	EOSTATE Powder bed		User decision on quality of powder spreading. Available for some polymer systems
	Online Laser Power Control	Presumed coaxial photodiode	Available for some polymer systems
Concept Laser (GE)	QM Meltpool 3D	Coaxial photodiode and camera	

Table continued

Company	Product name	Monitoring technique	Notes
	QM Coating	Dark field imaging	Automated decision if recoating is required
	QM Fibre Power	Coaxial photodiode	Monitors output of the laser
	QM Cusing Power	Laser powder sensor at powder bed	Separate manual calibration equipment for measuring delivered laser intensity at the powder bed
Sigma Labs (3rd party)	PrintRite3D SENSORPAK®	Multiple coaxial sensors	Mention of spectral monitoring of the melt pool and relative but not absolute melt pool temperatures. Also provides in-process monitoring for Additive Industries systems

Table 2.3. Commercially available in-process monitoring solutions. In-process monitoring products are not always available across all of a company's machines. Unless specified, all systems are metal PBF.

EOS appears to be the only manufacturer offering some advanced in-process monitoring in polymer PBF, but even with the greater variety of implemented in-process monitoring techniques for metal PBF, there are still gaps in capabilities. The powder bed monitoring is limited to dark field imaging with only two companies seeming to trust the powder bed monitoring system to trigger recoating strategies when issues are detected. There is significant room for improvement in industrial in-process monitoring and in-process control as shown by the almost complete lack of closed-loop in-process control for systems other than the laser. Geometric powder bed measurements would increase the range of defects detectable in-process, as well as providing more qualitative data for the in-process control that is expected to be implemented in industrial systems soon [25].

2.2.5 Coaxial monitoring

A laser delivers the energy to heat the powder bed in the most common PBF techniques, for both metals and polymers. This existing optical system provides an optical path that inherently tracks the processing region at all times. Therefore, coaxial monitoring provides direct, high speed information about the ongoing process of consolidation at the moment of melting. Passive observation of the meltpool via reflected light has been widely reported for metal PBF [99–101]. The integration into the processing laser's path is achieved with a beamsplitter diverting some of the reflected light into the detectors. Both individual photodiodes and arrays of photodiodes have been used to provide information about the meltpool emissions. Arrays also provide information on irregularities in the meltpool as well its shape. From reports in literature, it is unclear if geometric measures of the melt pool, such as length and width, give better information than just photodiode response [99, 100], because there will always be a general correlation between melt pool area and overall intensity. All major metal PBF machine

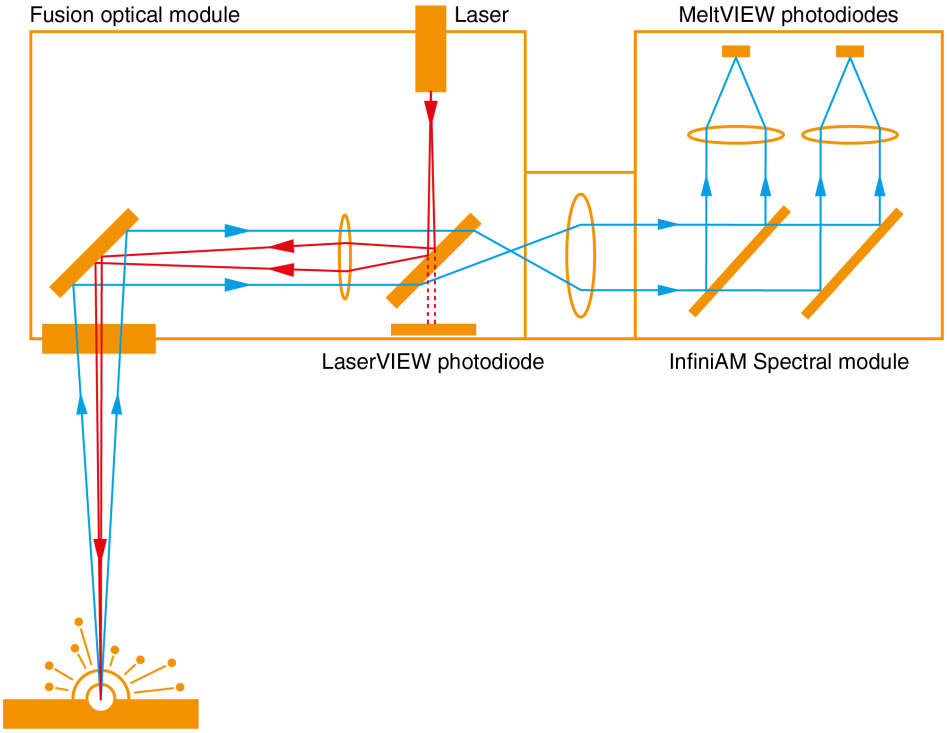

Figure 2.6. Two wavelength coaxial photodiode monitoring offered by Renishaw. One MeltVIEW photodiode is sensitive to visible light and the other is sensitive to nea-infrared light. Reproduced with permission from [85].

manufacturers offer in-process monitoring for at least some of their systems, coaxial monitoring often being combined with powder bed monitoring. See Table 2.3 for an overview of the commercial in-process monitoring solutions. A diagram of Renishaw's dual wavelength meltpool monitoring solution is shown in Figure 2.6. Renishaw state that the visible light photodiode detects plasma emissions from the meltpool and the near-infrared photodiode detects emissions due to the temperature of the melt pool [85]. Also pictured is a photodiode for monitoring the power output of the processing laser, ensuring consistent power delivery to the powder bed. Two wavelength monitoring of the metal PBF melt pool is offered by several manufacturers, see Table 2.3.

Eulerian measurements of the powder bed surface geometry have been achieved coaxially with the processing laser, with three systems described in the literature. Although they are described using different terminologies (low coherence interferometry [107], inline coherent imaging [122] or spec-

tral domain optical coherence tomography [108]), they are all broadband interferometers measuring coaxially with the processing laser. For polymer PBF there are several descriptions of optical coherence tomography (OCT) measurements that could be integrated into the processing beam. Guan et al. evaluated a medical OCT microscope for monitoring the polymer powder bed [56]. Whilst the measured surfaces were not in-situ, seeded subsurface defects of less than 100 µm were identified at the same time as the surface was determined. The surface defect lateral resolution was stated to be approximately 9 µm. The technique would require state of the art OCT equipment to be able to scan across a significant portion of the powder bed quickly enough to keep pace with the processing laser [123]. Lewis et al. [124] collected data from the central region of a test bed polymer PBF system by boresighting into the CO_2 laser path. Measurements were taken approximately 1 mm behind the laser spot on the powder bed and data was collected before and after consolidation of both one and two layers. Lewis et al. stated that the reduced scanning area, caused by defocusing as the distance to the powder bed increased, could be mitigated by using a field flattening lens in the sample path [124]. The polymer PBF OCT results presented in literature have high levels of noise and a penetration depth in air approximately equal to the layer height [125]. Therefore, despite the potential for penetrative in-process measurements, observations would still need to be taken every layer. It is unclear if the light emitted from the polymer melt zone is sufficient for passive in-line monitoring, since there are no reports in literature of its implementation. However, there does not appear to be a fundamental limitation of the particular measurement technique.

Laser ultrasound has a different measurement regime that has been demonstrated as viable for in-process monitoring of metal PBF. The technique induces localised thermal shock with a scanning laser beam. The shock waves that propagate through the part and along the surface are de-

tected by the deflection of a second, detection laser spot. Laser ultrasound has been investigated for in-process monitoring of metal PBF, detecting sub-surface defects [111], but reliably seeding defects into parts was challenging [126]. Spatially resolved acoustic spectroscopy is a laser ultrasound technique that has normally been carried out on polished surfaces, but recently it has been demonstrated to work with an as-built metal PBF surfaces [112]. The main barrier for further development of laser ultrasound techniques in metal PBF is getting enough signal from the rough surface's diffuse reflections. If the signal is not strong enough, data collection scans are slow and require multiple averages. Laser ultrasound techniques have been demonstrated with polymer samples [127], including optical detection of the propagating waves [128]. However, a consolidated part in a polymer powder bed fusion build chamber has poor signal propagation and signal return characteristics meaning it is not a practical in-process measurement technique for polymer PBF.

2.2.6 Powder bed monitoring

In contrast to Lagrangian coaxial monitoring, powder bed monitoring provides a stationary overview of the process before and after the consolidation of each layer. The monitoring is often implemented with optical techniques using infrared or visible wavelengths. This Eulerian viewpoint has the advantage of easier detection of defects such as warping, which occurs on a longer timescale and a larger length scale than the scanning of the HAZ of the laser spot. Other defects, such as improper powder spreading, can be detected with single camera views and standard image processing techniques [129]. This range of techniques is also suitable for polymer PBF.

High-speed camera observation of the metal PBF melt pool interacting with the powder bed provides a monitoring approach that has elements of

both melt pool and powder bed monitoring [130–132]. See Figure 2.7 for an example of a high speed camera configured to record the powder bed surface. The viewpoint allows for observations of melt pool dynamics whilst also allowing for the tracking of material ejected away from the melt pool, also known as spatter [133, 134], which is a common issue in metal PBF [135]. Other examples of Eulerian in-process monitoring include acoustic emission [109] and emissions from the processing plume [136]. Lagrangian powder bed monitoring has been reported, with a laser profilometer attached to a metal PBF system's powder recoating blade providing detailed 3D measurements of a 15 mm strip of the powder bed [137].

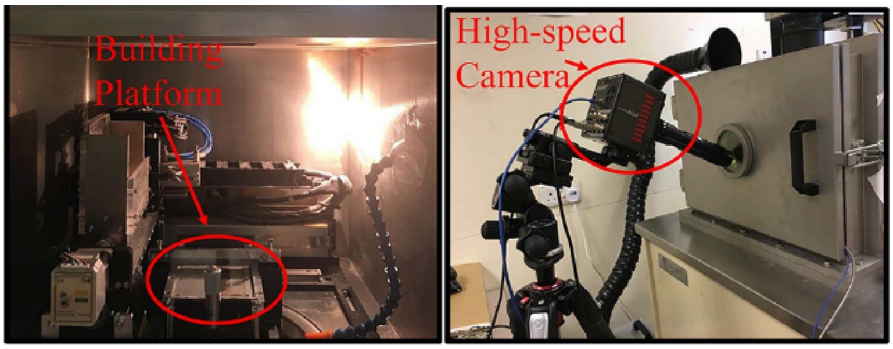

Figure 2.7. A picture showing the high-speed monitoring system described by Zhang et al. [138]. Figure reproduced with permission.

Computer vision methods

The task of a control system analysing the ongoing polymer PBF process could be considered as an application of computer vision. Computer vision is concerned with processing two dimensional (2D) and 3D images to provide high-level information about the world to computers. It is a mature field with applications such as informing robots of their environment [139], quantitative biological analysis [140] and interpolating medical images such as XCT measurements [141]. Utilising computer vision, photogrammetry is a method of reconstructing 3D geometry from multiple 2D images taken from different viewpoints. It uses scale-invariant feature detection to determine the relative

positions and orientations of each viewpoint. It has applications ranging from cultural heritage preservation [142] to post-process measurements of AM parts [143].

One application of computer vision for in-process monitoring of the PBF powder bed is using dark field lighting conditions to deduce the location of defects on the powder bed surface. This technique has been implemented in Trumpf's TruPrint range of metal PBF systems, for in-process monitoring without in-process control [144]. The lighting highlights features which deviate from the surface of the powder bed, with multiple angles being used to reduce the impact of shadowing on the results. The images of the multiple distinct lighting angles can be input for machine classification of defect type and severity [102]. Whilst abnormal areas of the powder can be detected, no quantitative measurements of heights of surface features are made. This constrains the process insight to detecting only potentially catastrophic failures, such as warping, but not more subtle process signatures such as drop due to consolidation.

Machine learning is a diverse and extremely powerful family of techniques for computerised recognition of patterns in data that has already been applied in some in-process monitoring situations. Neural networks (NN) originated as a biomimetic data processing technique, and have been used in control systems for decades [145]. Deep learning uses many-layered NNs [146], and has been applied to medical image analysis [147], traffic sign recognition [148] and playing the board game Go [149].

Any of the monitoring techniques discussed could be used as input for machine learning [102], NN [150] or deep learning [129, 134, 151]. However, there are some added complexities that arise from the use of machine learning identification and classification of defects. Supervised learning techniques require expert input through data sets labelled with previously identified errors which can represent a significant investment

of time, especially if there are a large number of categories of error [129]. Unsupervised learning techniques can avoid the requirements for a labelled training data set, but these techniques are more complex to implement and there is less control over the learning process, especially when the training dataset is small [147]. Whichever learning technique is chosen, descriptors, or features [152], are one technique to reduce the data into a manageable stream of information for the network [146]. This is because the larger the size of each input into a network, the larger a network needs to be to process the information, which can lead to instabilities and difficulties in training the network [153]. Generic 3D convolutional neural networks have been demonstrated for point cloud data but such high resolution points clouds created in-process might cause issues with process speed [154]. One specific machine learning method proposed for processing PBF data in the literature is a technique known as support vector data description (SVDD) [155]. SVDD can be trained with in-process monitoring data from multiple identical successful builds, creating an internal classification scheme for identifying the process state. When in-process monitoring data for an new identical part is analysed, the SVDD technique can classify the process as being successful or out-of-control. An application of deep learning to spatially resolved acoustic spectroscopy was demonstrated by Williams et al. [156], where acoustic spectrograms were processed to create a binary image, highlighting defects. Features such as pores appeared to be retained, but no quantitative analysis of defect detection was presented.

Comparatively cheap and easy to implement monitoring systems based on 2D imaging and computer vision techniques show some promise for fast detection of anomalies in the powder bed [67], but there is generally a lack of quantitative in-process monitoring that could improve insights into the consolidation process. It should also be noted that current state of the art techniques cannot demonstrate detection classification as accurate as a

human expert [129]. This raises the question of how accurate the defect classification of in-process monitoring needs to be in order to be beneficial. Not having in-process monitoring is equivalent to assuming that all regions of the powder bed have no defects being produced during the process. Therefore, if process improvement is the aim of in-process monitoring, then any correctly identified defect improves the process, even if only marginally. However, if the aim of in-process monitoring is to produce a certificate of quality that quantifies the expected performance of the part, then one missed classification per thousand layers could be a suitable accuracy threshold for industries such as aviation or medical implants. This is because even one defect has the potential to drastically decrease part performance and one thousand layers is a suitable approximation for an average PBF build.

Structured light

Structured light is a a family of active optical measurement techniques capable of measuring the powder bed surface in-process in PBF. It relies on the distortion of known patterns of light by the surface being measured. A simple example of pattern distortion for 3D measurements is the consumer product Kinect version one sensor which uses a known pseudo-random grid of dots projected onto a scene to take measurements. The pattern of dots is known because it is created by an infrared laser projecting through a diffraction grating, with known relative geometry [157]. The disparity of each dot from the known projected pattern therefore becomes a triangulation process to measure the distance to the infrared dot [158]. Because the number of dots is significantly less than the number of imaging pixels, a required feature for unambiguous recognition of the pattern, the resultant measurement has relatively low volumetric resolution. Pattern ambiguity has to be minimised otherwise surface measurements will not be a unique description of a measured surface. One strategy for reducing pattern ambiguity is measuring

the distortion of multiple patterns on the same surface, commonly found in phase-shifted fringe projection [159]. There are analysis techniques that only require a single fringe image, such as Fourier transform profilometry [160], but they can have issues if the spatial frequencies of the measured object are similar to the carrier frequency of the fringes [161]. Because structured light measurements can be obtained with consumer hardware, it has the potential to be cheaper to implement than more optically complex measurement techniques such as co-axial broadband interferometery.

If implemented in laser PBF, it is likely that only the eventual consolidation state of the layer would be measured, not the progress of consolidation from warmed powder to consolidated polymer part, because the processing area travels too quickly to be accurately captured. Two of the most important measurement requirements as mentioned in Section 2.2 are the speed of measurement and the measurement area. The measurement of the powder surface needs to happen in 1 s to 10 s and the measured volume is likely to be at least 100 mm $\times$ 100 mm $\times$ 1 mm. Also, the height resolution needed, perpendicular to the measurement plane, is likely to need to be in the order of 10 µm or less.

Fringe projection is a candidate for areal monitoring of the surface features of the laser sintering powder bed because the measurement volumes required are achievable at the level of resolution needed. Speed of measurement is highly dependant on the data acquisition method, of which several are discussed below. The method of fringe projection has been applied to ex-situ part measurements of polymer AM parts [53]. In-process measurements have also been made in metal PBF [106] and polymer PBF [94]. A system has been described by Dickins et al. [105] that fuses the data from fringe projection, photogrammetry and photometry . Fringe projection has been shown to be capable of detecting geometric defects as well as surface irregularities in the powder bed [94, 106]. The proposed mechan-

isms for defect detection with fringe projection do not differ from the generic suggestions for geometric measurements in Table 2.2. However, a fundamental limit of fringe projection is that it can only measure the surface of the powder bed, potentially limiting the detection of defects, such as porosity or poor inter-layer adhesion. In addition, the rate of measurement is many orders of magnitude slower than other in-line monitoring systems, such as photodiodes, which could limit the monitoring of dynamic events such as viscous flow of the polymer melt [75]. Despite the limits of fringe projection, the technique was chosen for further investigation in this project because of the combination of detailed powder bed height measurements, and a wide enough field of view, with typical equipment, to view the whole powder bed without scanning.

2.3 Fringe projection

There are many methods of obtaining fringe projection data. To help in choosing the most appropriate fringe projection method, the fundamental theory of the measurement technique first needs introducing.

2.3.1 Underlying mathematical theory

Fringe projection is a multiple viewpoint areal optical triangulation technique relying on diffuse reflection of light from a surface. A projector superimposes a fringe pattern onto the surface to be measured [159, 162], whilst a camera records the resultant pattern as distorted by the surface. When sinusoidal fringes are projected a minimum of three phase shifted images are required to reconstruct the surface's absolute phase unambiguously. Conversion of the absolute phase of points on the surface to real-world

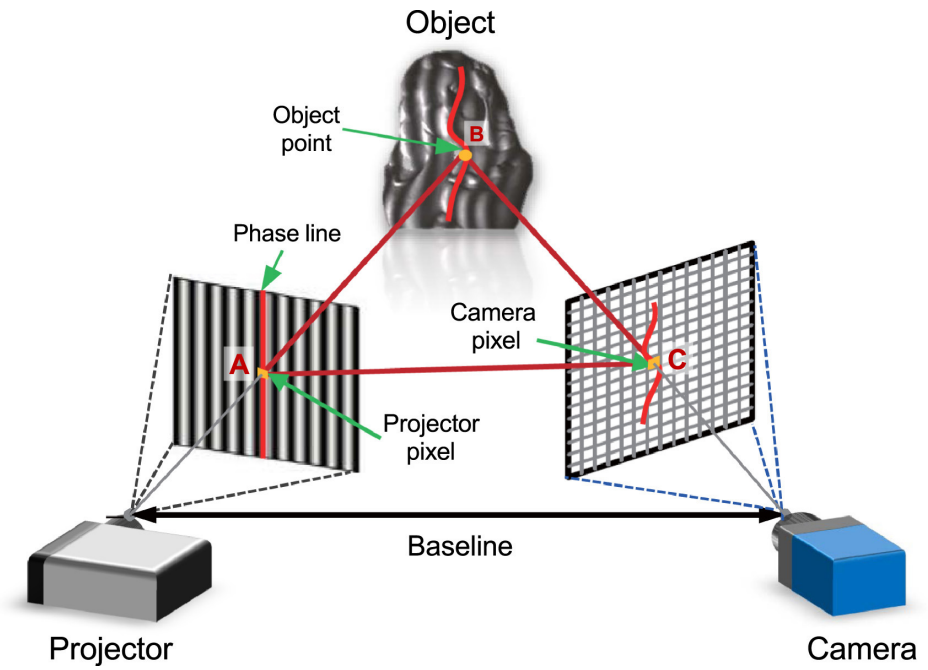

Figure 2.8. The geometry of epipolar correspondences in fringe projection. A single pixel in the camera image and a line of pixels in the projected image provide a unique triangulation of a point on the object's surface. Reproduced with permission from Zuo et al. [163].

co-ordinates relies on a calibration procedure. Epipolar geometry, the geometry of stereo vision which relates how a point's location in a scene can be constrained by it's recorded location in both images, underlies all calibration techniques. See Figure 2.8 for an illustration of the geometry of projector and camera pixel correspondences.

2.3.2 Basic phase shifting fringe projection

Whilst there are many different categories of patterns that could be used, sinusoidal patterns allow for every camera pixel to have a unique height measurement. Sinusoidal patterns are often used for high speed fringe projection because only three phase-shifted patterns are needed to collect data [162].

The irradiance distribution of the nth projected sinusoidal fringe pattern

in a sequence can be written as

$$I_n(x,y) = A(x,y) + B(x,y)cos[\phi(x,y) - 2\pi n/N] \tag{2.5}$$

where $I_n(x,y)$ is the spatial distribution of the nth fringe pattern, $A(x,y)$ is the static irradiance of the surface, $B(x,y)$ is the irradiance of the surface due to the varying fringe pattern (modified by surface reflectivity), $\phi(x,y)$ the wrapped phase map to be extracted and N is the total number of phase shifts used. The simplest case of three equally phase shifted fringe patterns allows for the solving of the three unknowns in equation (2.5), namely $A(x,y)$, $B(x,y)$ and $\phi(x,y)$. The wrapped phase map can be calculated with the following equation

$$\phi(x,y) = arctan\frac{\sum_{n=0}^{N-1} I_n(x,y)sin(2\pi n/N)}{\sum_{n=0}^{N-1} I_n(x,y)cos(2\pi n/N)} \ . \tag{2.6}$$

A one dimensional example of wrapped phase can be seen in Figure 2.9. Because the arctangent function has a range of $-\pi$ to π, the extracted phase needs the 2π discontinuities removing, a process called phase unwrapping. After phase unwrapping produces absolute phase, the results of a pre-existing calibration can then be used to relate this to real world co-ordinates in physical units.

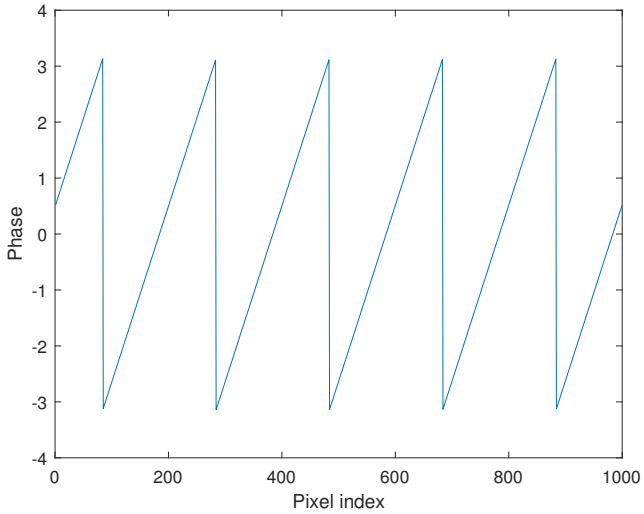

Figure 2.9. Wrapped phase from a fringe pattern that repeats five times across the image. The vertical 2π discontinuities are the wrapping points that will be removed in phase unwrapping.

2.3.3 Spatial and temporal phase map unwrapping

Because most fringe projection techniques produce wrapped phase maps, there is a a large body of literature on the process of phase unwrapping [162]. There are numerous approaches to phase unwrapping, with the two main categories of approaches discussed here being spatial and temporal unwrapping.

Spatial unwrapping requires a local neighbourhood search of each pixel to locate the phase discontinuities introduced by the arctangent function in equation (2.6). Once located, the required integer multiple of 2π is added or subtracted to the wrapped phase to give the unwrapped phase:

$$\Phi(x, y) = \phi(x, y) + 2\pi k(x, y) \tag{2.7}$$

where $\Phi(x, y)$ is the unwrapped phase and $k(x, y)$ is the integer multiple of phase jumps required to wrap the phase. The aim of all phase unwrapping algorithms is to quickly and accurately determining $k(x, y)$ for every pixel in the image. Spatial unwrapping is commonly used in high speed applications

because of the minimal number of fringe images required for phase unwrapping [162]. The local searching nature of spatial unwrapping has problems dealing with both local discontinuities and global discontinuities because of the lack of a continuous surface to move the wrapped phase towards. Local discontinuities can be overcome by algorithms that unwrap the most reliable phase data first, thus ensuring that the least reliable data regions are the areas of the measurement that suffer the most from accumulated unwrapping error [164]. Overcoming global height ambiguities requires extra information, often obtained through capturing extra images, extending the capture time and therefore requiring the measured surface to remain stationary for longer. The unwrapping techniques that use this extra information are commonly referred to as temporal unwrapping techniques.

There are a wide range of possible temporal unwrapping techniques that could be used for in-process fringe projection measurements. Because it is not possible to cover all possible techniques, three related techniques will be described and compared in this section. The unwrapping techniques are also covered and compared both experimentally and computationally in Zuo et al. [163]. Temporal phase unwrapping techniques seek to unambiguously determine $k(x, y)$, often using a second fringe frequency and relying on the temporal stability of the surface measured. A simple method is to project one set of high frequency fringe patterns to collect low phase noise wrapped phase data and to also project one set of fringe patterns that have a spatial period equal to that of the projected image, see Figure 2.10. Therefore, the wrapped phase of the high frequency data can be moved to coincide with the single period fringe data. This is mathematically represented by

$$k_h(x, y) = Round\left[\frac{(\lambda_l/\lambda_h)\phi_l(x, y) - \phi_h(x, y)}{2\pi}\right] \tag{2.8}$$

where $Round[\ ]$ rounds to the nearest integer, λ_l is the wavelength of the

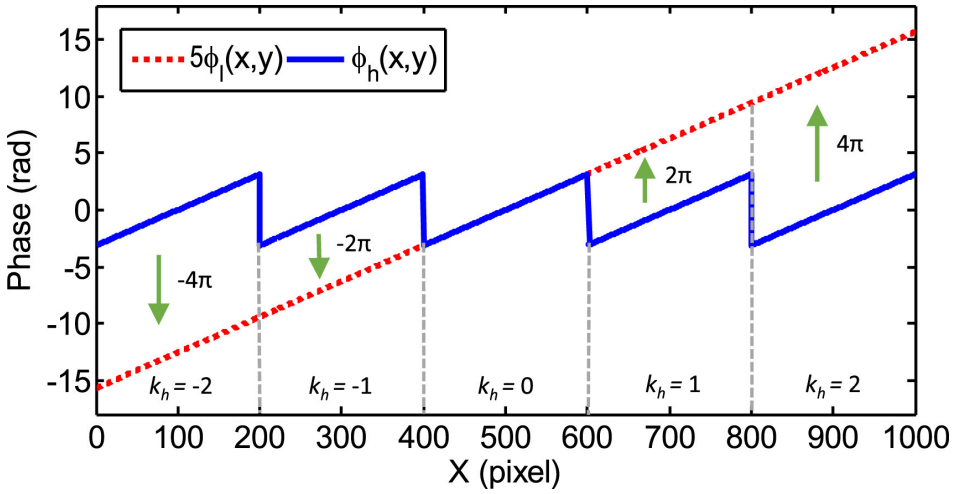

Figure 2.10. Using a phase map without wrapping to unwrap a higher frequency phase map. Reproduced with permission from Zuo et al. [163].

low frequency fringe, λ_h is the wavelength of the high frequency fringe, $\phi_l(x, y)$ is the low frequency wrapped phase, $\phi_h(x, y)$ is the high frequency wrapped phase and $k_h(x, y)$ is the integer fringe order function for the high frequency phase. This technique is shown in Figure 2.10. A serious limitation of this technique is that fringe patterns with a low spatial frequency have a higher relative phase noise than high spatial frequency fringe patterns [163]. Therefore, in some situations the low frequency fringe data has so much noise in it that the correct determination of $k(x, y)$ is not possible [163].

A different approach is to use two similar frequencies to create a synthetic wavelength phase map with no wrapping points, and then use this as an artificial low frequency phase map to unwrap with respect to the higher frequency data [165]. The synthetic phase data is calculated as

$$\phi_{eq}(x, y) = \phi_h(x, y) - \phi_l(x, y) \tag{2.9}$$

and the wavelength of the synthetic data is

$$\lambda_{eq} = \frac{\lambda_l \lambda_h}{\lambda_l - \lambda_h} \, . \tag{2.10}$$

The relationships between the phase maps can be seen in Figure 2.11.

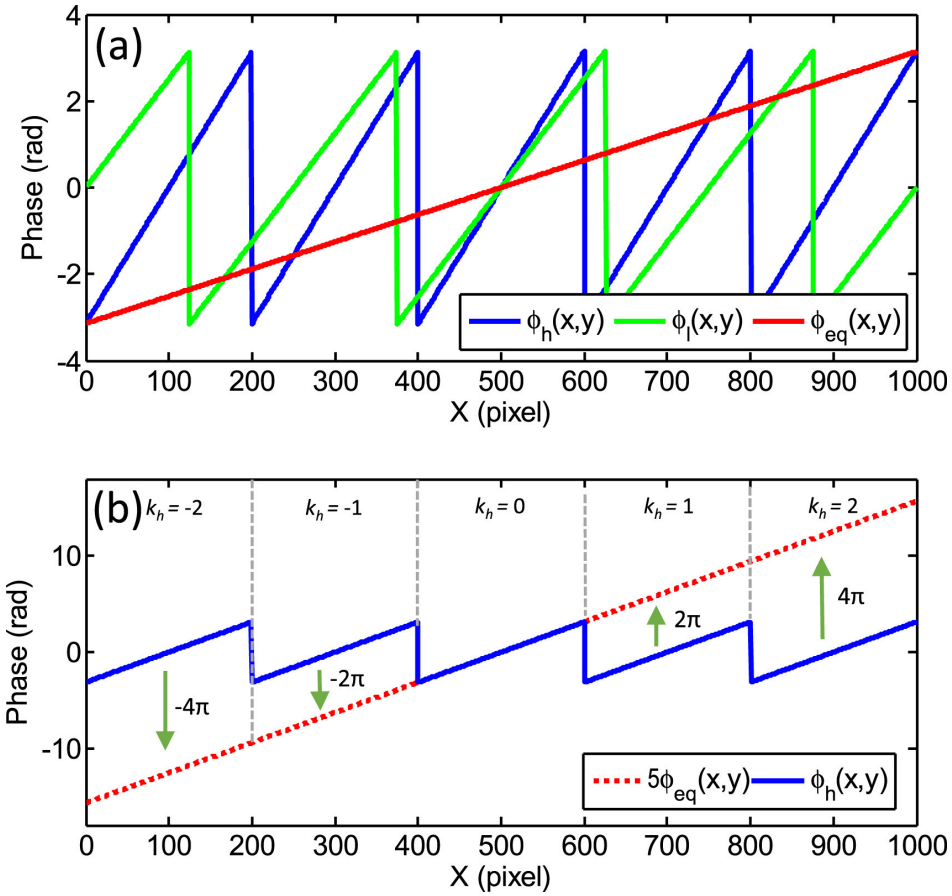

Figure 2.11. Using phase maps with similar fringe frequencies to create a synthetic phase map with no phase wraps. Reproduced with permission from Zuo et al. [163].

Because the difference of the two wrapped phase maps is used to create the synthetic, unwrapped phase map, the noise levels of the synthetic data are higher that the original data.

Number theory phase unwrapping combines some elements of both of the previously described methods. It uses a high frequency phase map and a lower frequency phase map, but the lower frequency has a period shorter than the size of the projected image [163]. The relationship between the two wrapped phase maps is

$$\Phi_h(x,y) = (\lambda_l/\lambda_h)\Phi_l(x,y)\ . \tag{2.11}$$

Given that we will be working with integer fringe frequencies, we can rewrite

equation (2.11) as

$$f_h \Phi_l(x,y) = f_l \Phi_h(x,y) \ . \tag{2.12}$$

Combining equation (2.12) with equation (2.7) leads to

$$(f_h \phi_l - f_l \phi_h)/2\pi = k_h f_l - k_l f_h \ . \tag{2.13}$$

Consideration of equation (2.12) shows that both sides can be integer values. f_h and f_l are freely chosen so they can both be integer values. Since $k(x,y)$ is defined to be an integer, it follows that the left hand side of the equation is an integer. f_h and f_l are known, and both ϕ_l and ϕ_h are measured. Therefore, the integer value of the right hand side of equation (2.12) is a unique value not repeated for other physically sensible combinations of the four values, and can be calculated by the following equation

$$(k_h, k_l) = LUT \left\{ Round \left[\frac{f_h \phi_l - f_l \phi_h}{2\pi} \right] \right\} \tag{2.14}$$

where LUT is the lookup table proposed by Zhong and Wang [166] as an efficient way to find the $k(x,y)$ value combination that corresponds to each pixel in the phase map [163]. A pictorial representation of number theory unwrapping can be seen in Figure 2.12. Zuo et al. showed that when implemented with suitably chosen fringe frequencies, the performance of number theory phase unwrapping was superior in experiments. Choosing the two frequencies to balance the poor quality of low frequency data and the noise sensitivity is covered by Ding et al. [167], who propose the following equality for assessing the suitability of fringe frequency selection

$$\Delta\phi_{max} \leq \frac{\pi}{f_l f_h} \tag{2.15}$$

where $\Delta\phi_{max}$ is the maximum phase error possible before erroneous phase unwrapping occurs and f_l, f_h are the number of fringes in a pattern for the

low and high frequency respectively, which can also be referred to as the normalised spatial frequencies. The effects of phase error on number theory unwrapping are shown in Figure 2.13.

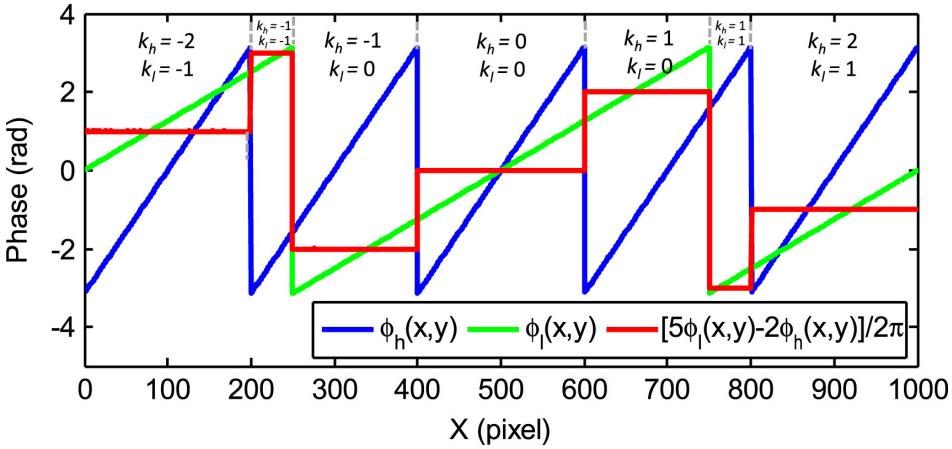

Figure 2.12. One dimensional number theory phase unwrapping, showing the relationship between the two phase maps, the lookup table value and the calculated values of k for both phase maps.

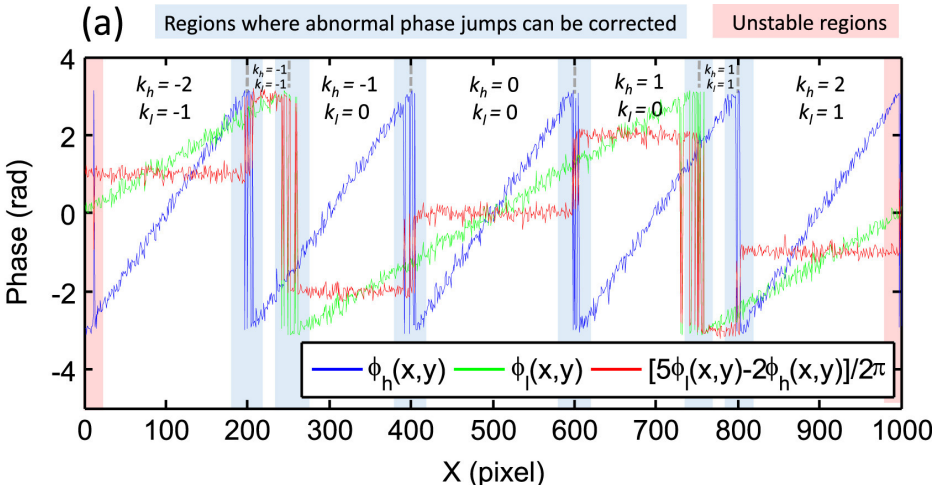

Figure 2.13. The effects of phase error on number theory phase unwrapping. Reproduced with permission from Zuo et al. [163].

2.3.4 Calibration

Once the unwrapped phase is calculated for the surface, a conversion into real world units is performed. This requires prior calibration of the camera and projector pair, though with some techniques it is possible to adjust their relative positions after calibration without requiring recalibration [168]. One

naive calibration process consists of an artefact of known dimensions and the deviation of phase from the reference plane is divided by the artefact's dimension to give a linear phase per millimetre conversion value. This technique is only valid for small deviations from the calibration plane [169]. It relies on assuming the distance between camera and projector is much larger than the distance between the projections of the point's camera and projector pixels onto the reference. This distance increases as the object's surface gets further away from the reference plane. A further issue with this calibration technique is that it ignores optical distortions of the camera and projector.

A more rigorous calibration routine is described in Zhang [162]. It uses a chequerboard target to calibrate the camera, followed by using the now calibrated camera to calibrate the association between phase and chequerboard. The camera and projector parameter matrices are then both used for converting from unwrapped phase to real world coordinates. A more detailed explanation is given in section 5.2.8.

A non-geometric aspect of the relationship between projector and camera is the so-called gamma calibration. Gamma calibration requires measurement of the relationship between the projected intensity and the intensity recorded by the camera. Gamma calibration is performed to ensure that the sinusoidal pattern recorded by the camera is as close to a true sinusoid as possible [162]. If incorrect gamma calibration is performed, periodic errors appear in the measurements performed by the system [170]. This is because the deviations from a true sinusoid are converted into measured deviations from the true surface. Gamma calibration requires projecting multiple intensities of light onto a representative surface and comparing the projected intensities with the the intensities measured by the camera. Once such a gamma curve has been established a lookup table can be created to enable a modified fringe pattern to be projected so it is captured

by the camera as a sinusoidal pattern [171]. This can also be seen as linearising the relationship between projected and measured intensities, see Figure 2.14.

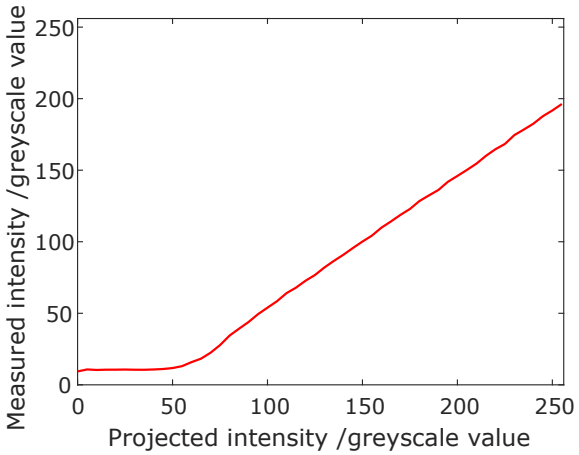

Figure 2.14. A relationship between projected intensity and measured intensity after gamma calibration.

Beyond calibration, international standards are often used for performance verification of structured light measurements systems. The current ISO standard most relevant to performance verification of a structured light measurement systems is ISO 10360-7:2011, which covers coordinate measuring machine (CMM) systems with imaging probing systems [172]. Another similar standard is VDI/VDE 2634 part 2 [173]. Both will be superseded by ISO 10360-13 which is currently being drafted with specific reference to optical volumetric measurement techniques such as fringe projection. Obtaining the required reference artefacts for either standard can be difficult because structured light systems struggle with reflective surfaces [174] so a precisely machined metal surface, such as that found on a gauge block, could be difficult to measure.

Performance verification of a fringe projection system does not enable traceable measurements to be made with that measurement system, only measurements that are similar to those performed during verification are traceable. Traceable measurements for a variety of objects require a rigorous

analysis of error sources and their influence on measurements. Such an investigation of fringe projection has not been reported.

2.3.5 Point cloud analysis

A common output of measurements of a powder bed surface geometry is point clouds, a common form of 3D data. A basic point cloud has no information other than the location of points, requiring processing to infer quantities such as surface normals and information such as which object a point belongs to. Estimations of surface normals and surface features are often carried out to improve the performance of point cloud alignment algorithms [175]. Point cloud alignment merges information from multiple point clouds to produce a unified measurement of the region of interest [176]. However, no registration is required when analysing the point clouds from in-process monitoring of the polymer PBF as the viewpoint is stationary and the measured region is what changes. One method of analysing the point clouds produced by these in-process methods is to use differential geometry, specifically curvature, to characterise the changes between points across the surface.

The common analysis metric of gradient is not well suited to point cloud analysis because a transform of the point cloud changes the gradient whilst curvature is an intrinsic property of the surface. For each considered point the calculation of curvature begins with the identification of the directions along the surface that experience the greatest and smallest rate of change of gradient. These vectors are notated as $\boldsymbol{\kappa_1}$ and $\boldsymbol{\kappa_2}$. Gaussian curvature, K, is defined as the dot product of these two vectors $\boldsymbol{\kappa_1} \cdot \boldsymbol{\kappa_2}$ whilst mean curvature, H, is defined as the mean of the two vectors $\frac{1}{2}(\boldsymbol{\kappa_1} + \boldsymbol{\kappa_2})$. As can be seen from their definitions, Gaussian curvature values are high for both peaks and troughs but mean curvature values differentiate between

them, with the choice of normal deciding which have positive values. When calculating curvatures of discrete surfaces such as point clouds, a quadratic approximation of the continuous sampled surface is used for each point [177]. An early overview of curvature estimation for point cloud surfaces can be found in Kreysig's book of 1968 [178] and Jovančević et al. demonstrated curvature being used to highlight manufacturing defects from point cloud measurements of objects - aircraft wings in their case [179].

A PBF powder bed is a nominally flat surface with highly rough surface texture and features that are raised or lowered above the powder bed surface by small amounts. Therefore, the regions of interest are those where the surface is changing height rapidly and thus have non-zero curvature.

Features identified with curvature analysis can highlight regions of a point cloud that deviate from their surrounding surface. Other techniques such as edge detection with gradient based metrics could be used, but the simple and robust technique of curvature analysis is described here. Whilst some edge detection techniques require multiple threshold values to be optimised, curvature analysis only requires a kernel size for reducing computational time if a faster processing speed is required. This reduces the subjective nature of choosing thresholds, as well as reducing the complexity of applying the analysis to a different situation such as a new material to be measured. Another reason to investigate curvature based analysis is for the input for machine learning algorithms similar to those described in literature [102, 155]. This is because pre-processing the data to identify features reduces the complexity of NNs required to successfully detect and classify defects [146]. Whilst machine learning has already been used for defect detection in PBF [102, 134, 180], 3D input data has not been demonstrated because of the increased complexity compared to processing 2D images, see Section 2.2.6.

2.3.6 Conclusion

Fringe projection can measure a polymer powder bed in-process without interrupting the manufacturing process and the cost of integrating such a monitoring system is a fraction of the total cost of an industrial PBF system. However, there are several challenges to overcome before useful in-process measurements can be achieved. At easily achievable viewing distances of roughly 500 mm and common bed sizes up to 250 mm, the depth of field of most imaging and projection systems will limit observations to be from above the powder bed only. As well as this, calibration will generally be carried out at room temperature, but given processing temperatures of around 200 °C, thermal expansion of the structure, along with convection currents in the build atmosphere could reduce calibration accuracy. Therefore, a robust calibration routine is required.

2.4 In-process control

As stated in Chapter 1, process control is desirable in all PBF, and is enabled by process monitoring. Having covered in-process monitoring, the capabilities and requirements of in-process control are covered in this section. Before discussing current literature it is useful to cover the fundamental theory and interactions of in-process monitoring and in-process control.

2.4.1 In-process control theory

A simple process to which process monitoring and control can be applied is the task of filling an open water tank. If the process is well characterised it would be possible to turn the valve on for a fixed time to fill the tank without risking the tank overflowing. This is an example of open-loop control, which

is simple to implement but it is potentially very sensitive to variations in input quantities (i.e. flow rate of the valve, shape of the container or height of residual water in the tank). Closed-loop control consists of taking feedback from the state of the process to inform any changes in process parameters that are required. At the most basic, an operator could control a valve that is either on or off and judge the water level by eye. In this situation, when the water level reaches the maximum permissible height, the valve is turned off. The state of the valve is, therefore, a process variable, the operator's judgement of the height of the water in the tank is a process measurement and turning the tap off to maximise the water in the tank is a process control decision. A more realistic example can be considered by increasing the complexity of the hypothetical system. One example of this is having a variable flow rate valve, the water height being measured by an ultrasonic distance sensor and computer implemented process control. Both levels of complexity for this system are shown in Figure 2.15.

It should be emphasised that there are many different approaches to process control and not all of them involve in-process control. There are five process control strategies described by Vlasea et al. in the context of metal PBF, three of which involve in-process control [181]. They are described here in the context of polymer PBF process control.

Pre-processing for predictive control requires computational models that can predict geometric distortions and optimised parameter sets based on part geometry and other specified constraints. The outcome of this control strategy is a pre-distorted part and optimised process parameters to produce the best possible part [182].

In-situ defect or fault detection and handling responds to measured defects or faults by interrupting the process to apply corrective actions. An example of this would be ridges left in the powder spread for a new layer. This is commonly caused by powder particles adhered to the recoating

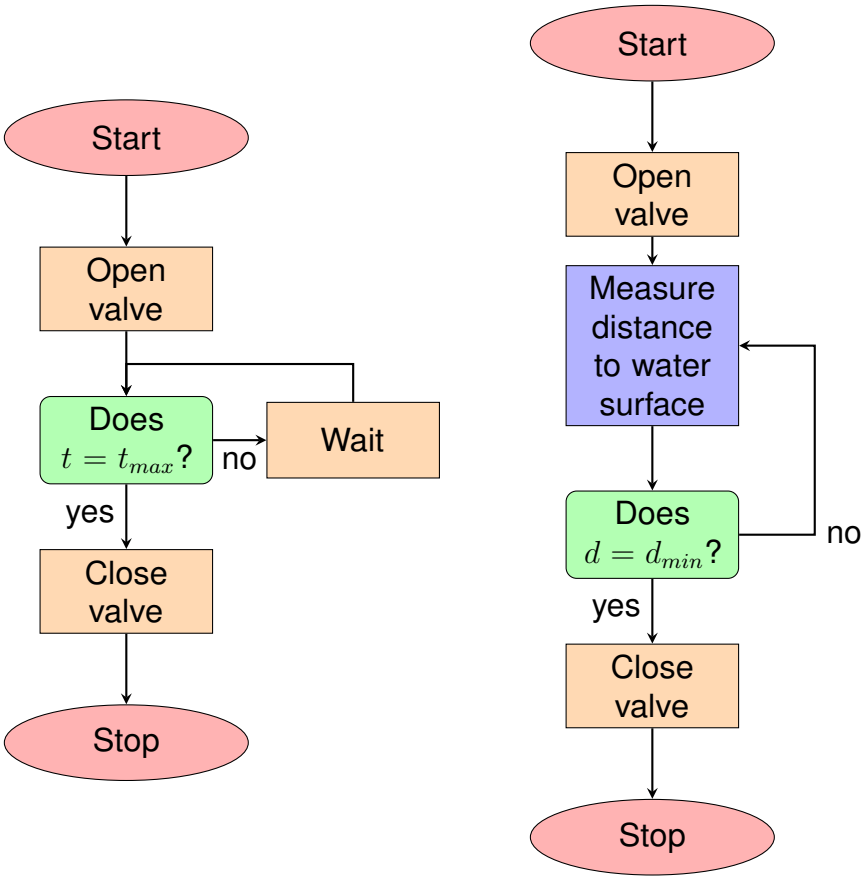

Figure 2.15. Process control flowcharts. (a) Open-loop process control example (b) Closed-loop process control example

mechanism. The corrective action in this case would be to initiate an automatic wipe of the recoating blade or roller, followed by spreading powder again to ensure a smooth, even powder bed surface. Another example would be detecting regions with poor consolidation and performing targeted reworking of the surface to repair the defects detected. This has been demonstrated for metal PBF by Hirsch et al. [183].

In-situ continuous feedback control receives in-process monitoring data and constantly modifies process parameters to maintain a stable process. A common example of this strategy in polymer PBF is using the information from pyrometers to vary the power output of powder bed surface heaters [16]. This helps to ensure a stable setpoint temperature, although their limited view of the powder bed does not ensure an even temperature across the powder bed. Another example is to use a photodiode constantly monitoring the output power of the processing laser to continuously modulate the laser beam power, ensuring consistent energy delivered to the powder bed [104].

Process signature derived process control through models or simulations uses in-process data to either run or update detailed process simulations or algorithms to predict the values of unmeasureable quantities. These predicted in-process signatures can then serve as input for other process control strategies. A hypothetical example would be predicting laser penetration depth from other in-process monitored variables. A hypothetical example is given because no literature appears to exist for PBF process control, Vlasea et al. [181].

Finally, part qualification through process monitoring and analysis produces a record of in-process measurements along with the control system's estimation of process state throughout the build. This can serve as an individual declaration of quality to state that the specific part was produced in the intended manner and should therefore conform with the expected part performance. Also, in the case of failure, the record of production could be

used to identify the cause of failure. It should be clear that any system could benefit from aspects of all process control strategy categories, but clearly delineating them allows for their individual dependencies on in-process monitoring data to be assessed.

2.4.2 Review of In-process control in powder bed fusion

In-process control of powder bed fusion has not been fully implemented in any system in literature [25]. Control systems for keeping the size of the laser meltpool constant have been demonstrated [100, 184], but the powder bed has had numerous monitoring techniques implemented without full control [67, 94, 129]. The most mature example of powder bed aware process control is powder spreading systems in Concept Laser's industrial machines. A camera captures a single image after a new layer of powder has been spread, and the decision is made as to whether it needs to be spread again to improve the powder bed surface ready for consolidation, see Table 2.3. This system does not measure the consolidated region and therefore can only be categorised as partial powder bed process control. Despite the lack of current progress, process control in powder bed fusion is expected to progress rapidly due to industry needs [25].

Abdelrahman and Starr demonstrated predictive process control by using the layerwise cross-sectional area of consolidation. Through three trial and error iterations, a set of laser power settings were developed that produced very little variation in average maximum temperature of the consolidated region. Wroe et al. demonstrated that the coldest layers in a tensile specimen gauge length partially correlated with the fracture location [185]. This shows that thermal control of all consolidated layers can be used to to ensure optimal mechanical properties.

With little process control demonstrated, it becomes important to highlight

process signatures that are good candidates for informing in-process control decisions. Zhang et al. reported the drop in height due to consolidation as a potential process signature for metal PBF [106]. Drop due to consolidation is observed in both polymer and metal PBF and is a consequence of the powder packing density being significantly lower than that of the final consolidated part. The evolution of consolidation over multiple layers is shown in Figure 2.16. Berzins et al. [186] illustrated the process in a similar manner, though with an emphasis on simulating densification during LS and describing the thickness of each layer as an integral. The application of heat to consolidate a new layer of powder must also provide enough energy to melt at least the top portion of the previous layer, otherwise inter-layer adhesion would fail. Therefore, when the first layer is consolidated, the excess energy creates a thicker layer and can cause excess part size in this direction. The overall thickness of the layer t_1 is unknown but the drop due to consolidation for layer 1, h_1, is the difference between t_1 and the height of powder bed the unconsolidated powder occupied. With a few added assumptions, this relationship can be expressed in a form that is easier to generalise across all layers. Therefore it is assumed that every layer is the same thickness, that each layer has the same geometry and that only the powder above a previously consolidated layer is consolidated. This final simplification assumes both that no powder adjacent to the consolidation is entrained and that all powder is fully consolidated without porosity. These assumptions are used implicitly by Zhang et al. [106] to construct the following series.

$$\begin{aligned} h_1 &= -t \times \alpha \\ h_2 &= -\left(t + h_1\right) \times \alpha \\ &\vdots \\ h_n &= -\left(t + h_{n-1}\right) \times \alpha \end{aligned} \tag{2.16}$$

where n is the layer number of the part being consolidated, h_n is the height

drop due to consolidation for layer n, t is the nominal layer thickness and α is $1-\beta$ where β is the powder bed volume fraction in comparison to the bulk material [106]. Each term in Equation (2.16) is a constant multiplied by

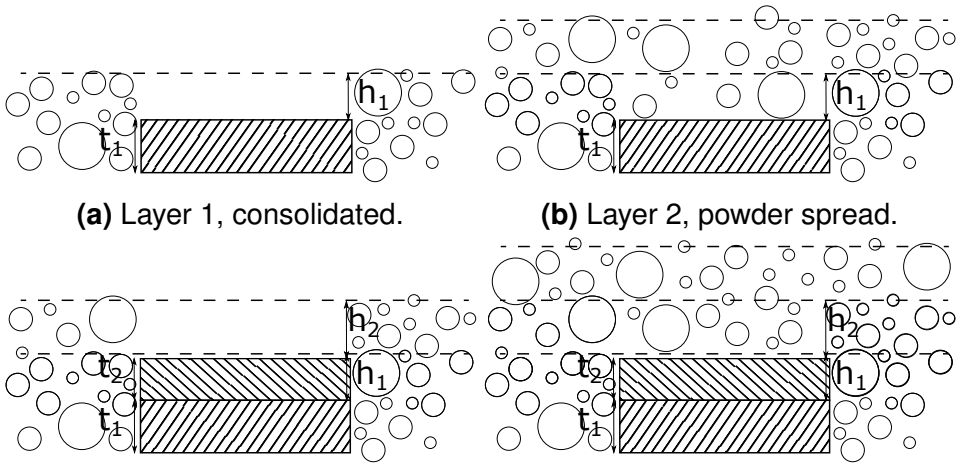

(a) Layer 1, consolidated. **(b)** Layer 2, powder spread.

(c) Layer 2, consolidated. **(d)** Layer 3, powder spread.

Figure 2.16. The progression of consolidated layers in PBF.

the previous term so Zhang et al. proposed describing the evolution of drop due to consolidation with a geometric series of the form

$$h_n = -t\alpha \times \left(\frac{1-\alpha^n}{1-\alpha}\right) \ . \tag{2.17}$$

This series quickly approaches the limit of

$$\lim_{n\to\infty} h_n = -t \times \frac{\alpha}{\beta} \ . \tag{2.18}$$

To investigate the rate of approach to the limit, the value of h_n for a given β and x, equation (2.17), can be dived by the eventual limit of h_n, equation (2.18). This simplifies to an expression that states the fraction of the maximum value of h_n, for a given layer is

$$1-\alpha^n \ . \tag{2.19}$$

Therefore, if β is 0.5 then $h_3 \approx 0.88$, $h_4 \approx 0.94$, $h_5 \approx 0.97$. If β is 0.4 then

$h_3 \approx 0.78$, $h_4 \approx 0.87$, $h_5 \approx 0.92$. In most powder bed fusion situations it is therefore expected that h_n will have reached at least 90% of its eventual limit by the fifth layer. This provides the opportunity for defect detecting and handling in-process control to evaluate the overall success of process parameters within a small number of layers of the build starting. It is expected that the consolidation model will apply to polymer PBF since the the only assumption is that all layers consolidate equally, which is expected for a successful polymer PBF build. Experimental results for polycarbonate (an amorphous polymer) found three layers were enough to reach the steady state limit for thickness, but measurements were not made of drop due to consolidation [186].

Accurate real-time measurements of layer thicknesses throughout a PBF build would enable real-time 'bonus z' compensation to improve part accuracy further than that possible with previous outline-based studies [94]. This would allow all three dimensions of a part to be monitored and deviations adjusted for in-process. This improved part accuracy is not only relevant to gross dimensions of parts, but complex interlocking features would also benefit from improved fidelity of geometry production. For example, overhangs are a well studied phenomenon in metal PBF, with simulations showing that reduced energy delivery for the initial overhang layers could significantly improve geometry fidelity [187].

The economic impact of in-process monitoring and control is not directly addressed in the literature but Baumers et al. describe a cost model that includes risk of build failure[10]. One consequence of considering risk of failure is that the optimal packing of the powder bed does not equate to full build chamber volume utilisation for the production of the maximum number of parts, because this increases the cost of a total failure. The cost model also considered individual parts being rejected after quality control inspections. Therefore, the economic benefit of in-process control

and monitoring can be estimated by calculating the relevant failure risks with and without the early interruption or intervention of process control. Also, employing a cost-optimised packing of the build area could lead to significant savings since the records of the monitoring systems would lead to very accurate failure rate estimations.

2.4.3 Conclusion

Powder bed fusion requires process control that can make decisions on the timescale of creating a layer, leading to reduced defects and therefore increasing reliability. Dynamic modification of process parameters or defect repair are two strategies enabled by such process control. The resulting improvement in reliability and reduction of defect occurrence and severity would make polymer PBF a more suitable manufacturing technique for end use parts.

Chapter 3

Thesis Motivation

3.1 Gap in the knowledge

It is clear that in-process measurements for PBF face several challenges to overcome before widespread adoption occurs in industry. These challenges include achieving optical access to the powder bed, implementing robust real-time analysis to enable process control and accurately calibrating measurements [25, 188].

Areal monitoring of the PBF powder bed has been demonstrated with dark field imaging [103], infrared imaging [189, 190], coaxial interferometry [108] and other depth sensing methods [56]. Of the depth sensing methods, structured light techniques require no scanning of the powder bed to obtain quantitative data, improving temporal coherence of data and reducing the complexity of system integration. Whilst fringe projection has been demonstrated for both metal and polymer PBF, the presented data analysis has been of limited use for process control. For example, Li et al. focused on part contour deviations from nominal and showed little examination of classifying the success of process parameters used [94]. Zhang et al. [191] rigorously demonstrated the linear nature of in-process fringe projection

measurements for PBF. However, process control requires process monitoring data analysis that can determine the real-time process state and this thesis demonstrates a monitoring system that can provide this.

This thesis will demonstrate that clear, actionable signals for process control can be derived from in-process fringe projection measurements. It will also demonstrate the applicability and utility of fringe projection for in-process powder bed monitoring in multiple powder bed fusion processes. There will be a particular emphasis on the process signatures measured and their analysis for process control.

3.2 Research aim

The overall aim for the thesis is to further the understanding of failure modes and process control strategies through process monitoring of polymer powder bed fusion with fringe projection monitoring.

Objectives

- Investigate both the laser sintering and high speed sintering processes with fringe projection measurement systems;
- Understand the methods of measurement of flaws during the powder bed fusion process by inducing flaws whilst performing process monitoring;
- Demonstrate the utility of process signatures derived from point cloud measurements of the powder bed surface.
- In-process measurements will not interrupt the processes monitored.

- In-process signatures will be resolved with enough detail to identify process failures before they happen.

In summary, this thesis will demonstrate that clear, actionable signals for process control can be derived from in-process fringe projection measurements of a polymer PBF powder bed surface. It will also demonstrate the applicability and utility of fringe projection for in-process powder bed monitoring in different powder bed fusion processes. There will be a particular emphasis on the process signatures measured and their analysis for process control.

3.3 Thesis structure

The remainder of this thesis is structured as follows:

- In-process fringe projection measurements of LS, concerning the use of a commercial fringe projection system to measure the powder bed of a commercial LS machine;
- In-process fringe projection measurements of high speed sintering. Process signatures are derived from measurements taken with a custom designed fringe projection system;
- Discussion of the results from both polymer powder bed fusion processes, comparing and contrasting the processes and measurement systems;
- Conclusion, summarising the main insights of the work and including specific suggestions for further research questions.

Chapter 4

In-process monitoring of laser sintering with fringe projection

As stated in the literature review, Chapter 2, the implementation of robust in-process control enabled by in-process monitoring is needed to improve part quality and part reliability as well as enabling certification of critical components, such as medical implants [192]. In-process monitoring enables real-time process feedback which can be acted upon, before the build finishes. This action can either be cancelling a failing build, repairing a detected defect or modifying parameters to reduce the chance of further defects occurring.

Whilst fringe projection has been widely demonstrated as a suitable post-process measurement technique for polymer PBF parts, there is only one report of it being used in-process [94]. The data collected allowed for an investigation of the quality of data of the powder bed surface measurements, see section 4.2.2.

In order to investigate the data quality that can be achieved with in-process fringe projection measurements of the polymer PBF powder bed a commercial fringe projection system was used to measure an industrial system's polymer powder bed in situ.

This chapter is based on two published papers by the author, 'In-process measurement and monitoring of a polymer laser sintering powder bed with fringe projection' [193] is the basis for the experimental results. The curvature based analysis uses the analysis method presented in 'Curvature-based segmentation of powder bed point clouds for in-process monitoring' [194].

4.1 Experiments

To interpret in-process point cloud measurements, the relationship between process conditions and process outcomes and therefore the process map location being measured needed to be established as precisely as possible before measurement. This allowed for comparison with literature in order to confirm the processing regime investigated.

4.1.1 Process mapping

Part geometry used

The part geometry chosen for the builds was a tensile test specimen following the ASTM D638-14 standard [72], see Figure 4.1. This allowed for tensile tests to be carried out on a large number of parts produced at the high temperature conditions. Because of the high sampling rate of the process map, only half of the produced tensile test specimens were required for tensile testing. Although the nominal part followed the ASTM D638-14 standard, some as-built parts fell outside specifications due to thinner gauge widths at lower energy densities. Three tensile test specimens were built in each layer of parts orientated flat in the powder bed, shown in Figure 4.2.

Figure 4.1. A computer rendering of the ASTM D638-14 Type I tensile test specimen geometry used. The gauge width is 13 mm, overall length is 165 mm and the maximum width is 19 mm. The thickness of the nominal geometry was 3 mm.

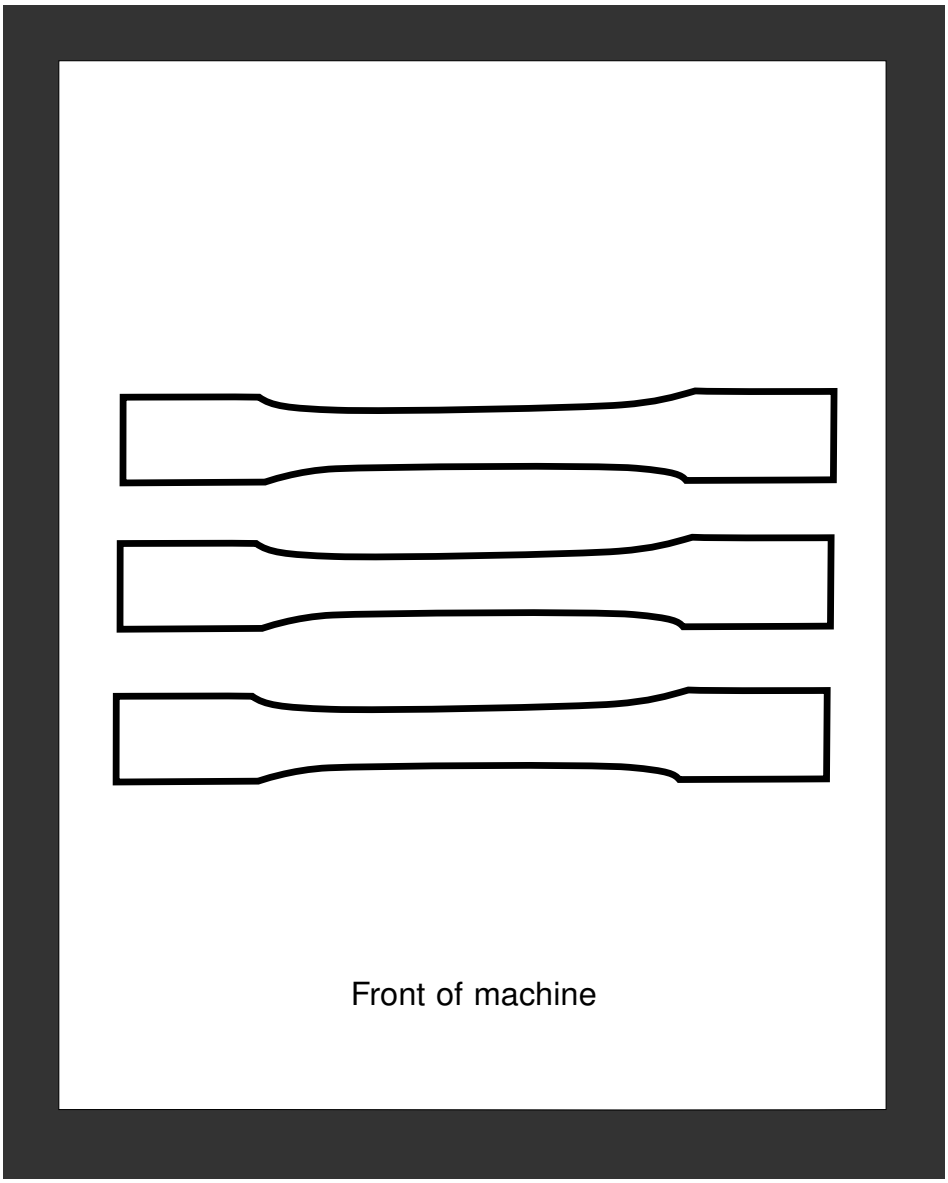

Figure 4.2. Aerial view of the tensile test specimen locations in the powder bed. This layout was used for all process mapping builds. In contrast, most of the builds observed by fringe projection had four evenly spaced tensile test specimens, with the 17 W and 4 W builds observed with fringe projection having only one tensile test specimen located towards the front of the machine.

Machine used

All builds were carried out in an EOS P100 LS system, see Figure 4.3, using 50% recycled polyamide 12 from EOS, PA2200, with an average particle size of 56 µm and specified built tensile strength of 48 MPa [195]. The EOS P100 gravity feeds the polymer powder from the top of the machine, dosing the powder into the main powder well which is on the left hand side of the machine. The powder spreading system uses a blade travelling in an arc, which is centred at the rear of the machine, to spread each new layer of powder. The powder spreading also distributes powder to the secondary powder well on the right of the machine. Rotating dividers in the powder wells dose the powder spreading blade with a consistent amount of powder for each new layer.

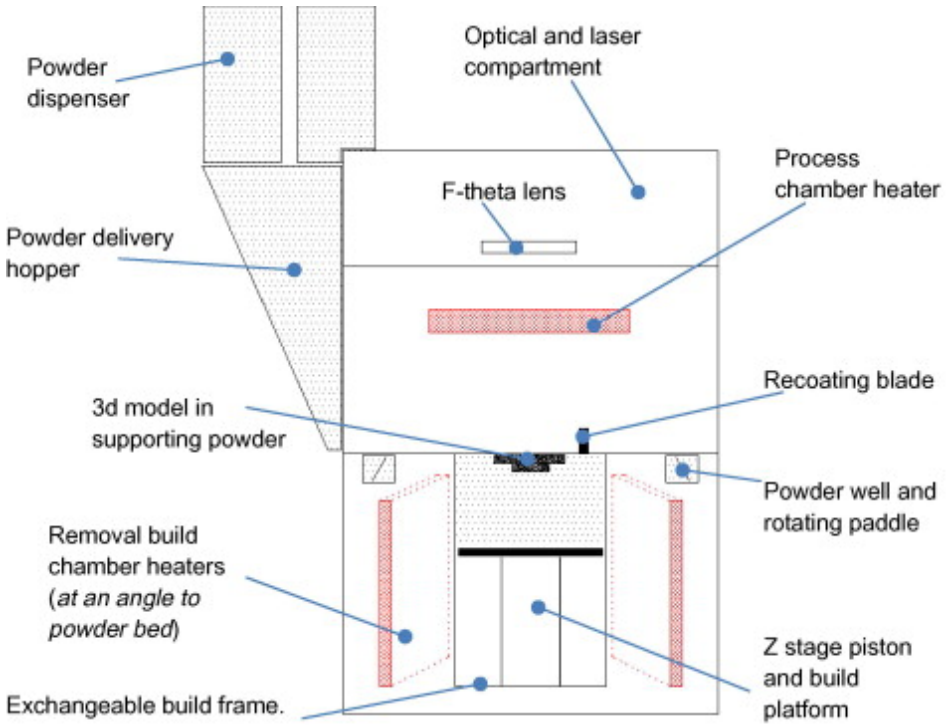

Figure 4.3. Schematic of an EOS P100 Formiga system. Reproduced with permission from Goodridge et al. [16].

Variables selected

There are a large number of process parameters in PBF, that can impact the successful production of parts [42, 196], but to reduce complexity, only the main parameters that strongly influence the delivered energy density to the powder bed are considered here. These parameters are laser power, scan speed, hatch spacing and layer thickness. For the process mapping in this work, the layer thickness was set to the commonly used value of 100 µm and the hatch spacing was set to 250 µm. This hatch spacing was approximately half the diameter of the laser spot, ensuring each hatch line got sufficient remelting from previous and subsequent hatch passes. This relationship between hatch spacing and laser spot diameter was recommended by the equipment manufacturer for the powder used. The direction of hatching alternated each layer between x-axis aligned hatching and y-axis aligned hatching, a common technique to reduce the build up of residual stresses in a part. The option for skywriting was also enabled. Skywriting increases the accuracy of the laser path when hatching by extending the laser path outside the part so the curved turning path of the laser spot is not incorporated into the finished part. The laser is turned off whilst the laser sport is outside the hatching region. The method chosen for searching the rest of the process parameter space (laser power, scan speed) was an iterative search methodology with non-uniform variable intervals, identifying the boundaries of the successful build quality envelope and the failure regions with reduced number of builds that would fail to print. An emphasis was made on finding the failure boundaries on the process map, to assist in later selection of parameter combinations.

Because these measurements were aimed at studying the LS process in standard operating conditions, and to reduce the number of experiments required, some other common variables were excluded from consideration. These were multiple laser scans and part position in the build chamber.

The process mapping did not consider the possibilities of using multiple laser scan passes per layer. This processing technique delivers the laser heating in several passes, thus reducing the stresses in the coalesced regions and extending the consolidation process [59]. It is commonly used with difficult to process polymers, and therefore was not considered necessary for polyamide 12.

Part position in the build chamber was also not monitored or varied. It can be important because the rate of cooling experienced by a polymer part produced with laser sintering influences the crystallisation process, which in turn, influences the mechanical properties of the part [197]. When large numbers of parts are placed in the same build chamber the local thermal environment can vary due to the residual heat of processing that all parts conduct and radiate as they cool down to the temperature of the surrounding powder. Therefore, it should be noted that because parts were built at different positions in the build volume, consequently with different amounts of residual heat from neighbouring parts heating the region, it is possible that the cooling rates of parts varied throughout the build volume [198].

Some builds, chosen due to their position in the process map, were measured in-process with a commercial fringe projection system (NUB3D SIDIO XR). Two of these builds, the 17 W and 27 W builds, were measured with a Nikon MCT225 XCT system, and a voxel size of approximately 12 µm, to investigate porosity and other defects that occurred during the builds.

4.1.2 Fringe projection measurements

In-process fringe projection measurements of the laser sintering powder bed surface were made with a NUB3D SIDIO XR. The nominal measurement pitch was 75 µm in all three orthogonal directions, with a scanning

volume of 200 mm $\times$ 150 mm $\times$ 90 mm. After calibration, a 1σ volumetric accuracy of 15 µm and a 1σ precision of 7 µm, was achievable as stated in the specifications.

The powder bed was viewed through the operator observation window of the machine. On the P100, this consists of an outer curved acrylic window and a thermally insulated flat glass window. For the in-process measurements of the powder bed surface, the viewing angle was roughly 55° from horizontal. The builds consisted of single tensile test specimens, with best measurement results when the test specimens were closer to the front of the build chamber, due to reduced data density, see Figure 4.4. The measurements were manually acquired when the sintering of the closest tensile test piece to the window had finished. When the laser scan path

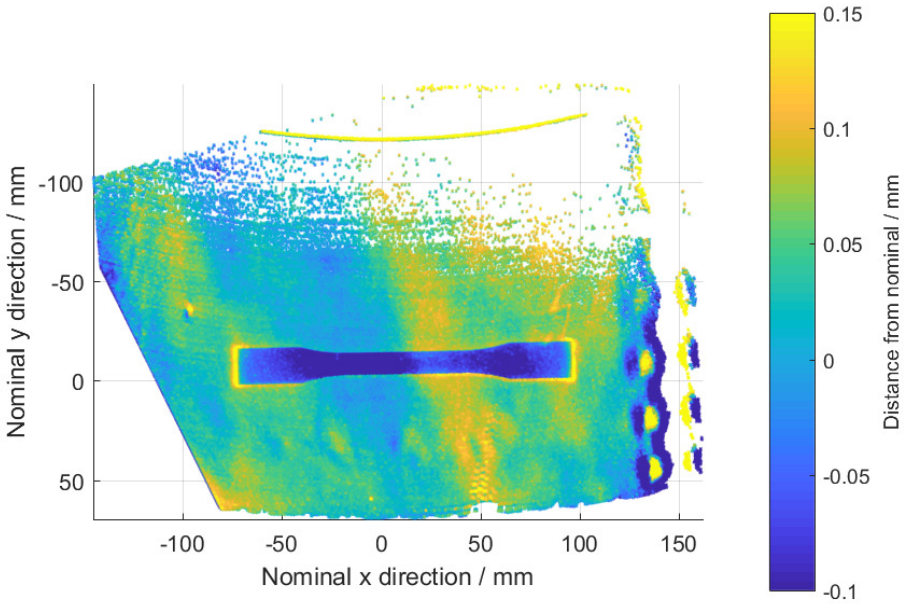

Figure 4.4. Representative point cloud from layer 15 of the 17 W build. The circular features on the right hand side are artefacts created by decorative patterns on the outer window.

was not visible, due to insufficient sintering, operator judgement rather than visual observation was employed to ensure the measurement was started at the correct point in the overall laser scan path progression. When the measurements were made at incorrect times, this was noted and quantified.

For example, some late triggering of the scans lead to the powder recoater blade entering the measured volume or the powder bed being lowered for the next layer before the scan was completed. The scans consisted of a series of projected binary fringes followed by a series of projected phase shifted sinusoidal patterns. Each complete scan was repeated with three different camera exposure times, to improve dynamic range of measured points. These camera exposures were 300 ms, 400 ms and 500 ms.

Similar to the temporal phase unwrapping techniques presented in Chapter 2 the hybrid binary and sinusoidal fringe approach allows for absolute phase to be calculated from sinusoidal fringe projection, by using binary fringe patterns to encode $k(x, y)$, see equation 3 in Chapter 2. The commercial control software created a wrapped phase map from the fringe images. The creation of the unwrapped phase map was also performed by the control software.

The control software could then convert the unwrapped phase map could into a point cloud with real-world co-ordinates because of calibration prior to the measurements [199, 200]. This calibration consisted of imaging multiple poses of a target with a grid of circles with calibrated distances between circle centres. The target was moved along the optical axis of the instrument at known intervals using a motorised lead screw. This created a set of poses of the calibration artefact throughout the measurement volume of the system. The control software could then optimise the calibration parameters to minimise the residual errors on the distances between the measured and true locations of the circular targets. The true location of the circular targets can be found by best fitting all the points with the known calibrated grid measurements.

4.2 Results

4.2.1 Process map

Parts were produced at various nominal powder bed surface temperatures, ranging from 150 ℃ to 174 ℃. Many builds at 174 ℃ completed successfully, although some parts were very fragile, showing the wide range of process parameters with which parts can be built with polyamide 12. If polyamide 12 had a narrower processing window, failure modes other than thermal degradation would be seen for the 174 ℃ builds. Figure 4.5 shows the variation of process outcomes with respect to powder bed surface temperature and energy density. As can be seen in Figure 4.5, the lower the temperature of the build, the earlier the failure by blade interaction tended to occur.

In order to further investigate failure modes, the chamber temperature was varied to as low as 150 ℃ and at the lowest chamber temperatures no builds could be completed. Failures were characterised as one sample being dragged across the powder bed by the recoater blade or no sintering being visible through the observation window. Figure 4.5 also allows spatial grouping and delineation of process modes and the parameters that are required to produce them. For example, in-process monitoring of builds on the left hand side of Figure 4.5 would be expected to have significant curl. In-process measurements a the temperature of 160 °C would be expected have minimum curvature at approximately $2.5\,10^{-2}$ J mm^{-2}, where the process maps indicates. At the temperature of 165 °C it can be seen that a 4 W build ($0.0064\,10^{-2}$ J mm^{-2}) will have issues with curling and potentially part-blade interactions. In comparison, a 17 W build ($0.0272\,10^{-2}$ J mm^{-2}) will have close to ideal build performance (for the given temperature). Finally, a 27 W build ($0.0432\,10^{-2}$ J mm^{-2}) will probably not have and curling issues, but any powder bed temperature irregularities could cause a catastrophic failure

since the process map for a temperature of 160 °C shows immediate curl failures at this energy density. This energy density at 174 °C is associated with reduced part strength, so it is possible in-process monitoring could detected this issue even in normal temperature builds.

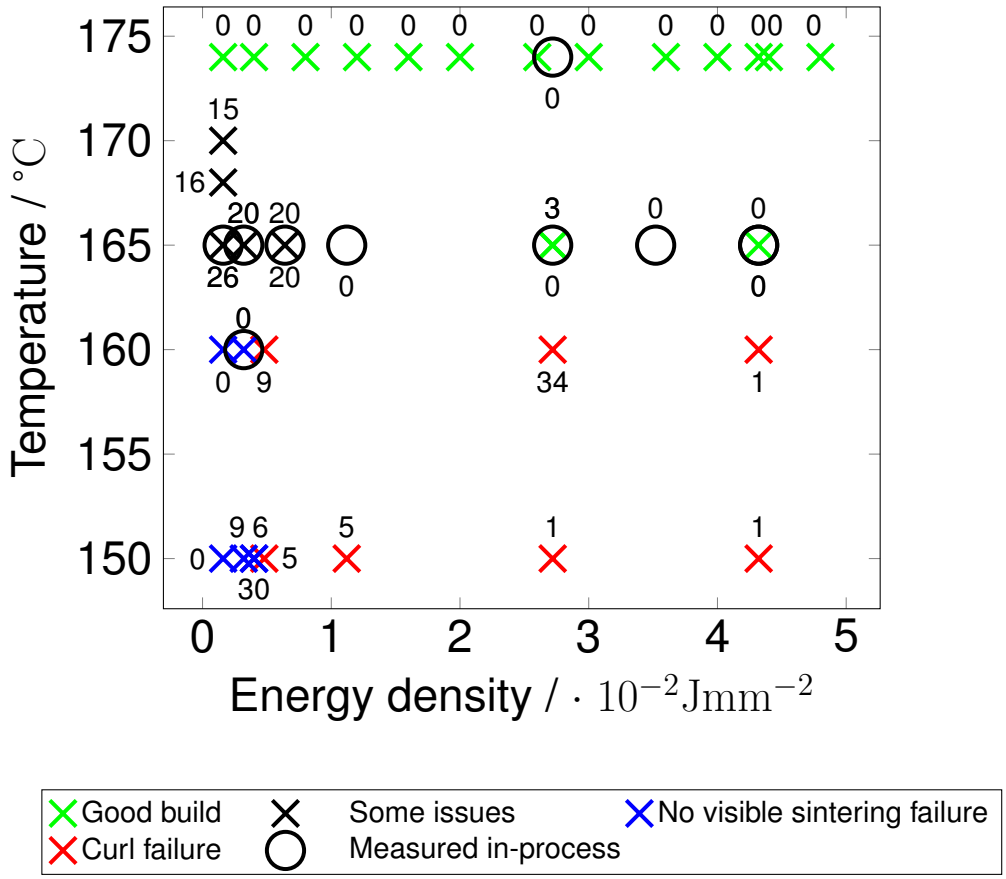

Figure 4.5. A process map detailing how the failure modes change with both energy density and powder bed temperature. The layers on which failures or blade interactions occurred are denoted by the numerical labels on points. Greater detail of two of the builds measured in-process are detailed in section 4.2.2.

,

Figure 4.6 shows the relationship between applied energy density and ultimate tensile strength at the powder bed temperature of 174 ℃. The results can be separated into three regions. The first region is to the left of the dashed line and shows the rapid onset of sintering. The second region spans from the right of the dashed line to about 0.035 J mm^{-2} and contains the parameter combinations associated with successful builds. The final region starts from about 0.035 J mm^{-2} and continues into increasing energy

density. Parts produced that fall into this final region show signs of polymer degradation, through their reduced mechanical properties.

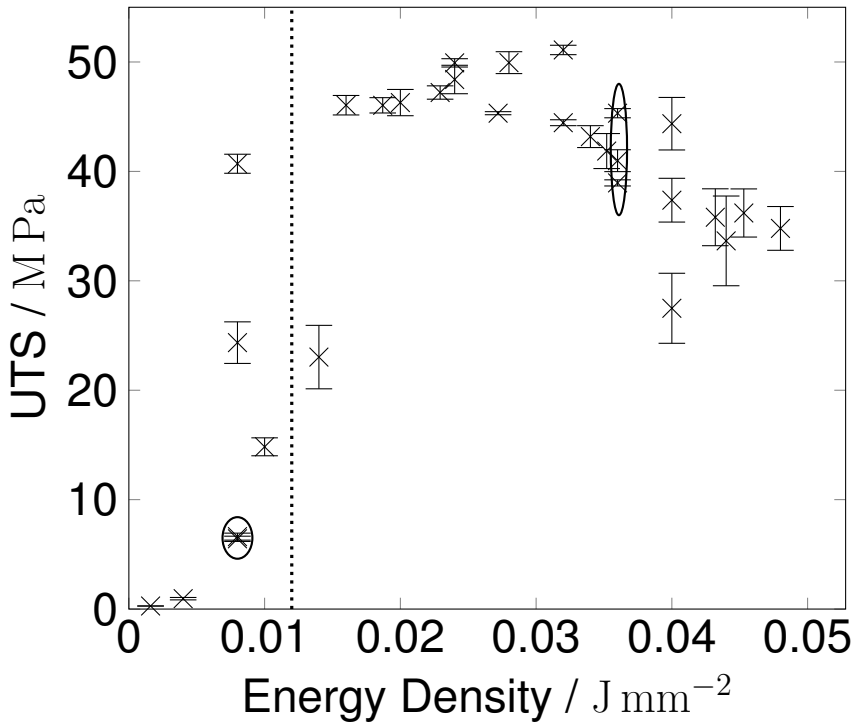

Figure 4.6. A plot of ultimate tensile strength against areal energy density at 174 °C. The increase in strength for partially recycled powder happens around the previously reported energy density of 0.012 J mm^{-2} for polyamide 12 with a layer thickness of 100 µm [69], see dashed line. The black ovals highlight two places on this graph where results have been repeated for the same parameters. These results appear to agree with previous literature [28, 69, 70].

4.2.2 In-process monitoring

Two builds in particular form the majority of the results presented here. Their building parameters were a laser scan speed of 2500 mm s^{-1}, a hatch spacing of 250 µm, a layer height of 100 µm a powder bed surface temperature of 165 °C and laser powers of 4 W and 17 W respectively. The point cloud data of individual layers consisted of approximately 290,000 points. As can be seen in Figure 4.4, there was a lower density of points towards the negative nominal y direction. The data collected of a flat powder bed

showed constant planar distortions, which can also be seen in Figure 4.4. The scanning arrangments did not allow for a calibrated flat to be placed on the build bed and removed again without re-positioning the measurement system. Therefore, whilst a calibrated flat could be used to subtract the distortions from the point cloud it would not be a valid processing technique once the measurement system had been re-positioned. This was accounted for by subtracting the height map of a nominally flat reference scan of the powder bed. The mean difference between nine flat powder bed layers and the flat reference scan is 0.03 µm $\pm$ 62 µm with 95% confidence intervals, and no systematic form errors. The mean difference between the powder bed scans is within the stated accuracy of the SIDIO XR, the magnitude of uncertainty within these results is small compared to the process signatures considered, hence a clear and flat powder surface is an adequate reference from which to perform measurements. The categories of structural defects relevant to process control, identified using the fringe projection system and the data analysis, are presented next.

Curl

Figure 4.7 shows a height map of the final sintered layer of a part with severe curling. Not only are the sintered areas above the powder bed surface, heaping of surrounding powder can also be seen, especially around –30 mm in the x direction. The slope of heaped powder extends at least 10 mm from the consolidated part. Figure 4.8 demonstrates that, even in a build which did not end in catastrophic blade interactions, the part's effect on the powder bed was still visible after 2.9 mm, or 29 layers, of powder bed had been spread on top of the completed part. The features are about 50 µm from nominal, close to the average particle size. It is unknown why one side has a raised feature whilst the other side has a depressed feature. This example demonstrates that curling failure is easy to detect and analyse, which is

covered in greater detail in section 4.2.2.

Powder bed surface irregularities

Figure 4.8 shows smaller powder bed surface irregularities, which were seen on every layer, as well as the larger-scale lifting of the powder bed caused by underlying sintered regions deforming. If a consolidated region deforms after powder has been spread on top of it, the powder surface above it will be lifted by that deformation. Because consolidated regions are free floating inside the powder bed it is also possible for regions of the bed to be depressed by the downwards deformation of a section of a consolidated region. Because the small-scale irregularities were arc- shaped, they were attributed to spreader blade issues. The issues likely arose from particles attached to the powder spreader blade, leaving grooves roughly one particle diameter deep. It is is common for some amount of polymer powder to get attached to the spreader blade during the build because the powder is kept close to melting temperature and some particles will be partially molten when the blade spreads new powder. Equally, it is plausible that a nick in the spreader blade would leave a raised arc-shaped irregularity because powder particles would not be completely contained by the blade during powder spreading. Both categories of defects are desirable to detect, and the fringe projection measurements are suitable for both. It is not clear why the curled ends of the part cause a raised area on the left hand side and a depressed area on the right hand side.

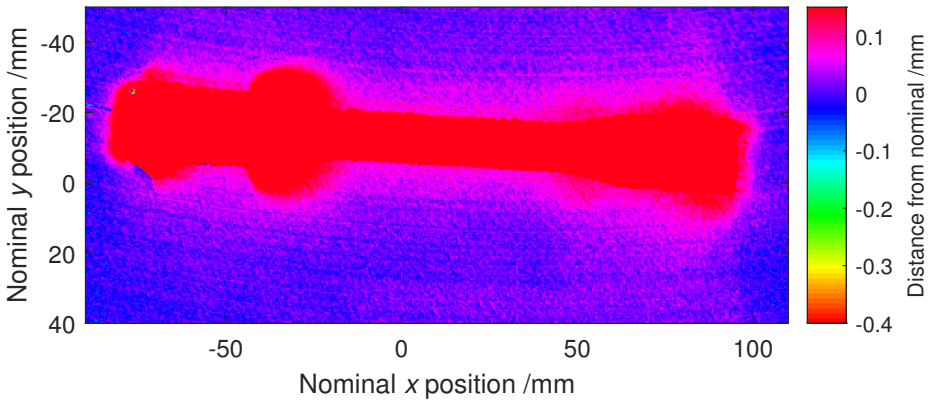

Figure 4.7. Height map of the 30th and final layer of a successful build with significant curling, processed at 165 °C, 4 W with a scan speed of 2500 mm s^{-1}. The maximum curl at both edges is over 1 mm, which includes the contribution of rocking caused by the part interacting with the blade. Fig. 5 shows this effect across the many layers of the build. The height of most of the part is measured as > 0.1 mm so it has one uniform colour.

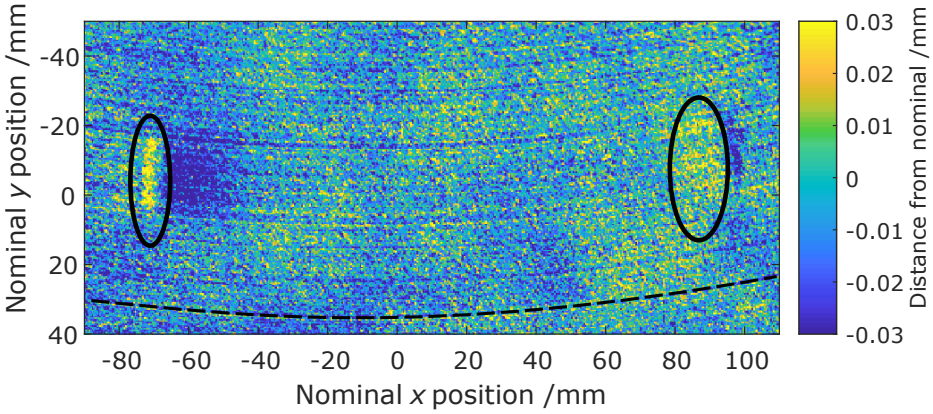

Figure 4.8. Height map showing twenty-nine layers of fresh powder after the final sintered layer seen in Figure 4.7. The continuing effect of the curled ends of the part can be seen. The ovals indicate the positions of both ends of the part. The dashed line indicates the arc that powder spreading defects follow.

Blade interactions

The rocking motion shown in Figure 4.9 is caused by the powder spreader blade catching the trailing end of the part and pushing it deeper into the powder bed. This severity of interaction between blade and part often leads to a part being dragged out of the powder bed and a failed build, but in this instance, the build completed. The onset of the blade interactions appears to occur when the maximum height of the part is approximately 500 µm above nominal powder bed height.

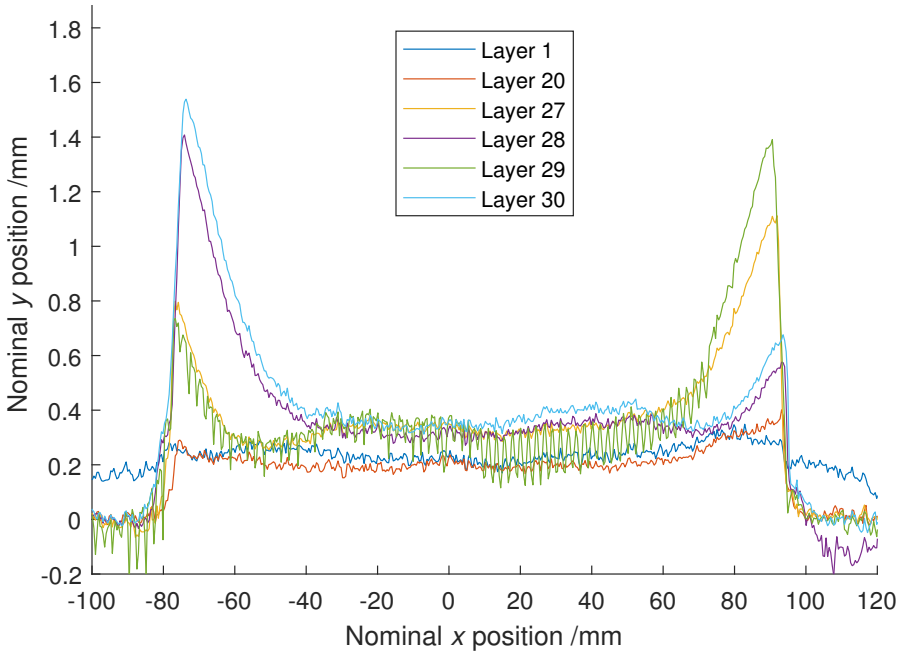

Figure 4.9. A profile along the centre of the tensile test specimen, as shown above, processed at 165 ℃, 4 W and a scan speed of 2500 mm s^{-1}. High spatial frequency artefacts in the data for some layers are due to the bed being lowered before all the fringe projection patterns had been captured. Towards the end of the build, alternate layers have opposite ends raised.

Level drop due to consolidation

The reduction in height of a layer due to consolidation, through melting of the polymer powder bed is a direct measure of successful densification in laser sintering of a polymer [186], visible in Figure 4.10. The trend of height

drop due to consolidation is discussed further in section 4.2.2. Another example of part blade interactions is also demonstrated in the sintered area of layer 16. The inset shows the broken end of the specimen which had been caught by the powder recoating blade. The remaining defects in the sintered region reduces in size in subsequent layers and is hard to discern by layer 22.

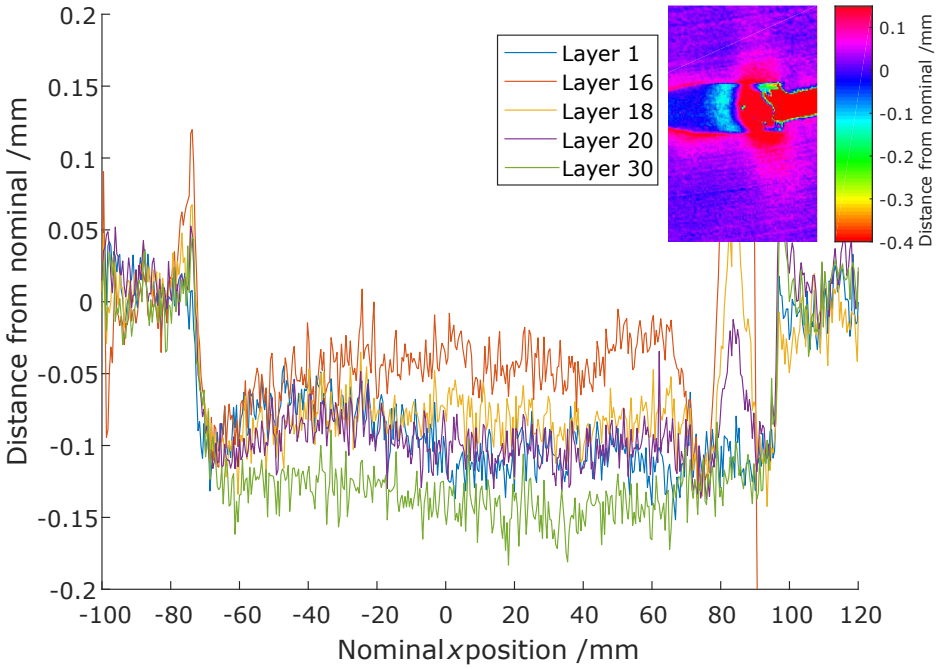

Figure 4.10. Tensile test specimen at 165 °C, processed at 17 W with a scan speed of 2500 mm s^{-1}. A 0.1 mm to 0.15 mm drop due to sintering is observed. Possible causes of the high edges are non-optimised settings for contours, an optical effect of the side of the drop or localised warping at the edge of the part [58, 201]. The profile was taken from the same region as shown in Figure 4.9. The inset shows the powder bed after the sintering of layer 16, the part-blade interaction happened when the fresh powder was spread for the sintering of layer 16.

Process signatures

Reducing the point cloud data of the powder bed surfaces to numerical quantities that are representative of performance allows for simple process control decisions. Two such measures are presented here.

Figure 4.11 shows that height drop due to consolidation, an indicator of the success of sintering, is clearly seen in the 17 W data. The drop due to consolidation on the first layer is significant, close to the layer height of 0.1 mm, and the general trend over the next 10 layers is towards increasing drop due to consolidation. The increasing height drop due to consolidation as the build progresses is expected but does not fit the geometric series proposed by Zhang et al. [106], see Figure 4.12. The value of β, see equation 1 in Chapter 2, for the 17 W build is calculated to be 0.468 with a 95% confidence interval of 0.466 – 0.471.

The corresponding graph for the 4 W build, Figure 4.11a, shows no discernible trends due to excessive curl and limited consolidation. As the maximum height drop is dependent on both the powder packing efficiency and the degree of consolidation, it is possible to estimate the degree of consolidation in-process. Figure 4.11b also shows that random defects during the process, see Figure 4.10, can be detected in the drop due to consolidation process signature.

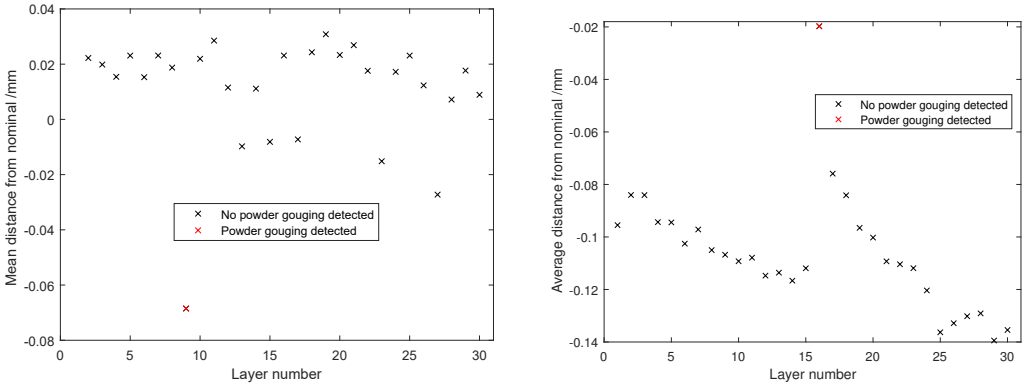

(a) 4 W build **(b)** 17 W build

Figure 4.11. Mean distance from nominal of consolidated powder. Powder gouging was detected when > 0.1% of the powder bed was measured at > 300 µm below nominal.

In contrast to height drop due to consolidation, the maximum height of the consolidated area, see Figure 4.13, indicated whether sintering is proceeding without curling. Figure 4.13 (a) shows the effect of an isolated

error on the maximum height reached above the powder bed for the 4 W build. Both before and after layer 16, the maximum distance from the nominal powder bed surface is about 150 µm. The magnitude of the change makes this derived process signature suitable for in-process control decisions as it can be reliably be detected in-process, see the inset of Figure 4.10 for a height map of the part blade interaction which led to part of the consolidated region being dragged along with the recoating blade. Figure 4.13 (b) shows the instability of the 4 W parameter choice as the maximum height from the powder bed increases up to the final layer (30) and then decreases as new powder covers the warped part. The inflection point around layer 20 is thought to be caused by blade interactions, see Section 4.3.1 for a suggested mechanism, and is another clear indication of process issues beyond the increasing amount of curling seen before layer 20.

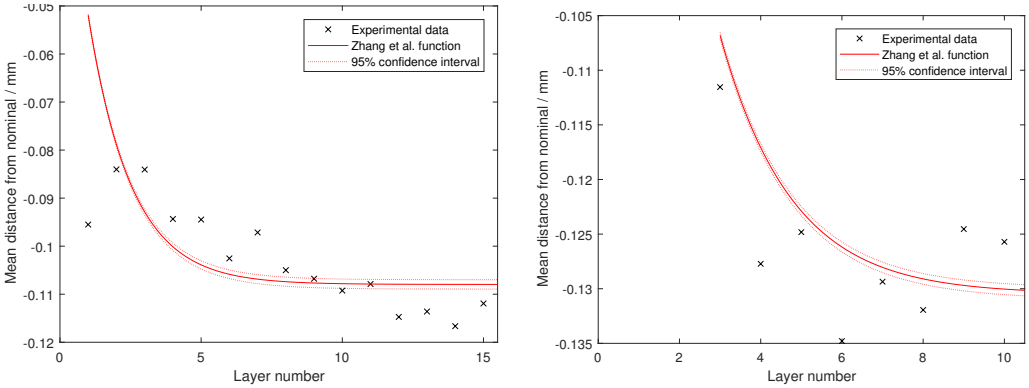

(a) 17 W build. **(b)** 27 W build.

Figure 4.12. The data from the 17 W build has the function suggested by Zhang et al. [106] fitted to the first 15 layers of the build. It clearly does not fit. The data from the 27 W build appears to fit better, but after layer 10 the data has a trend towards less drop due to consolidation so it is unclear how representative the fit is.

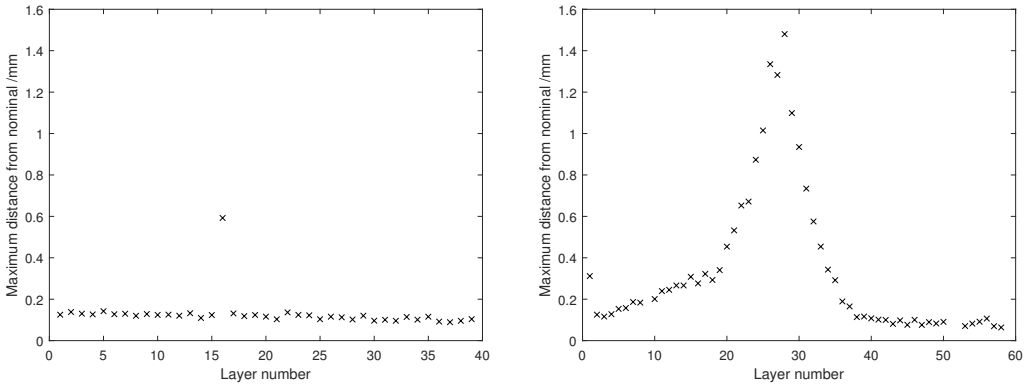

(a) **(b)**

Figure 4.13. The evolution of maximum height of the consolidated area for both builds. The influence of erroneously measured points was mitigated by removing the top 0.01% of data which has not changed the overall trend of results. a) 17 W build with the defect in layer 16 shown by the outlying point b) 4 W build with a clear deviation from the steady state results shown in a).

4.2.3 Curvature based analysis

Curvature analysis is presented here to demonstrate its ability to highlight defects found in the powder bed of a polymer PBF process, and segment the 3D data into powder bed and consolidated polymer regions. Three separate maps of gradient curvature, mean curvature and prominence can be seen in Figure 4.14. These are the three metrics that will be used in this section to analyse the point clouds of the in-process powder bed surface.

Segmentation

Segmentation of a point cloud consists of dividing the data into semantically labelled categories. Using segmentation, the point clouds of a polymer PBF powder bed can be labelled as either powder bed or consolidated polymer. The segmentation allows for the powder bed and regions that will form the part to be analysed separately. A more complex segmentation procedure could label consolidated regions depending on the model they are a part of. The curvature based segmentation demonstrated here uses common image segmentation techniques such as binarisation, erosion and dilation to create a logical mask and then refine it to only include the consolidated region of the powder bed. To create the mask, the binarised Gaussian and mean curvature maps as well as the binarised prominence map were combined to select the consolidated region of the powder bed. The binariseation thresholds were set using the common Otsu technique [202].

Powder bed analysis

The curvature maps of the powder bed show several features that are present in every layer's scan. These features could be caused by particles

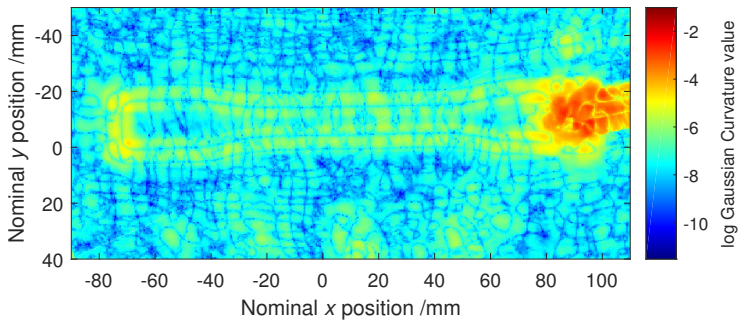

(a) Gaussian curvature

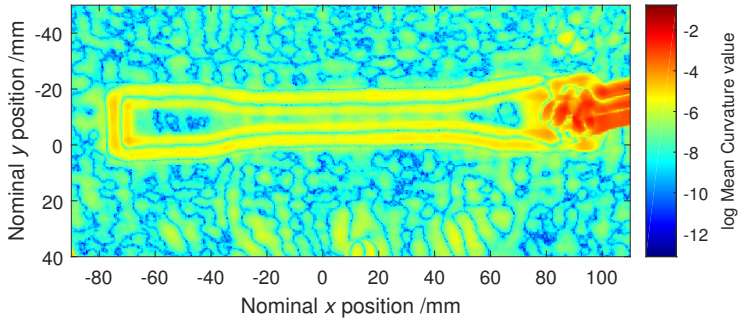

(b) Mean curvature

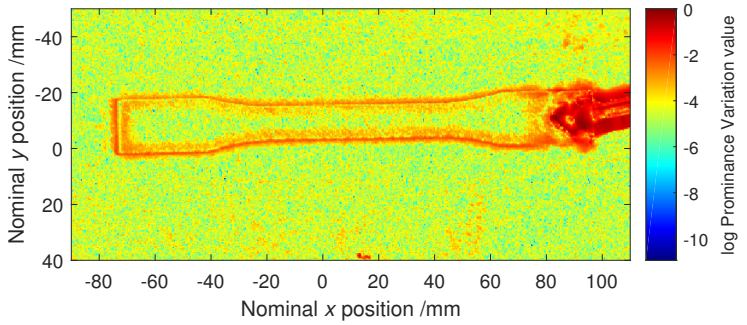

(c) Prominence

Figure 4.14. Curvature and prominence maps of layer 16 of the build with a 165 °C powder bed surface, 17 W laser power, laser scan speed of 2500 mm s^{-1} and a hatch spacing of 250 µm. All point cloud measures calculated with a kernel corresponding to a size of 5 mm.

stuck to the P100 viewing window, but irrespective of their source since they appear in every layer scan it can be assumed that are not a feature of the powder bed surface which gets refreshed every layer.

Consolidated region analysis

The produced part segmentation mask extends a small distance past the consolidated region and into the heaped powder regions. This can be seen in the segmented height map shown in Figure 4.15. Because of the inclusion of the powder heaps around the edge of the parts, the change in segmented outline between layers indicates the change in relative sizes of the powder heaps around the consolidated region. To more clearly see the heaping that occurs, the median of the even and odd layers was calculated and then plotted together. Figure 4.16 shows the left hand edge of the consolidated region. Figure 4.17 shows that the heaping around the edges of parts occurs before the part is fully consolidated, but the measurement was likely taken after the border scan had been completed, therefore, it is possible that the powder heaping is a result of the extreme edge of the border scan curling up and interacting with the powder being spread. Potential mechanisms are covered in Section 4.3.1.

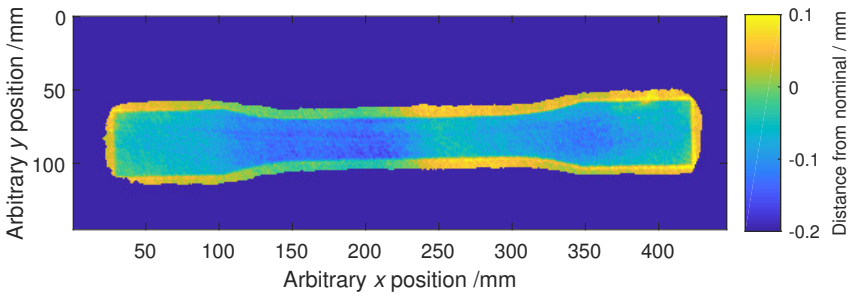

Figure 4.15. The segmented heightmap of layer 1 of the 17 W build.

Four identical parts, equally spaced in the powder bed were built with a bed temperature of 165 ℃, a laser power of 27 W, a scan speed of

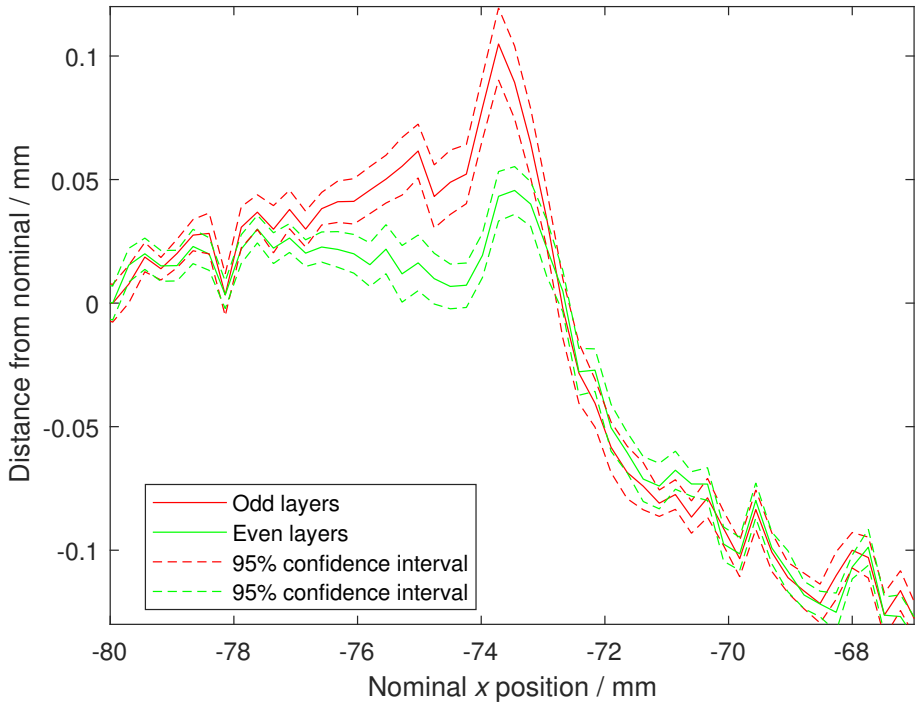

Figure 4.16. The median height map for odd and even layers in the 17 W build. Odd layers were consolidated after powder had been deposited from left to right, with even layers have powder deposited in the opposite direction. 95 % confidence intervals calculated from the error on the mean.

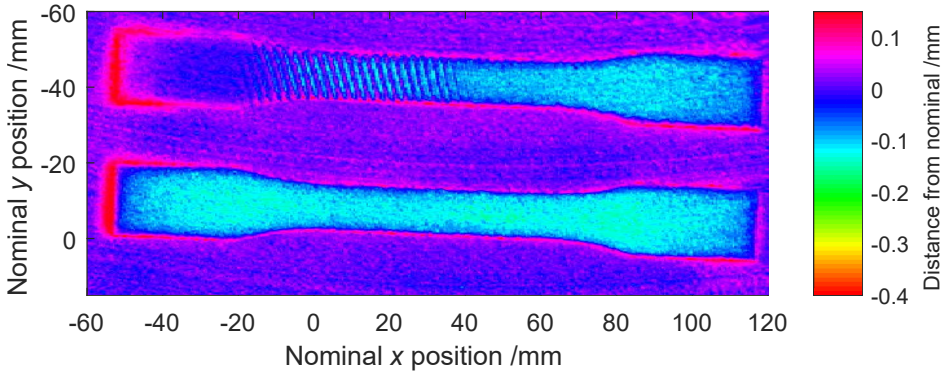

Figure 4.17. Height map of a partially consolidated tensile test specimen, powder heaping can be seen around the edges. Build parameters were a bed temperature of 165 °C, a laser power of 27 W, a scan speed of 2500 mm s^{-1} and a hatch spacing of 250 µm.

2500 mm s^{-1} and a hatch spacing of 250 µm. The part second closest to the front, the positive y direction in the figure is the front, developed the defect on the boundary of the part, which persisted and could be seen in the final part. XCT results suggest the defect is the result of a high point persisting through many layers and disrupting the normal sintering process, see Figure 4.18. The defect can also be seen in the curvature maps see Figure 4.19.

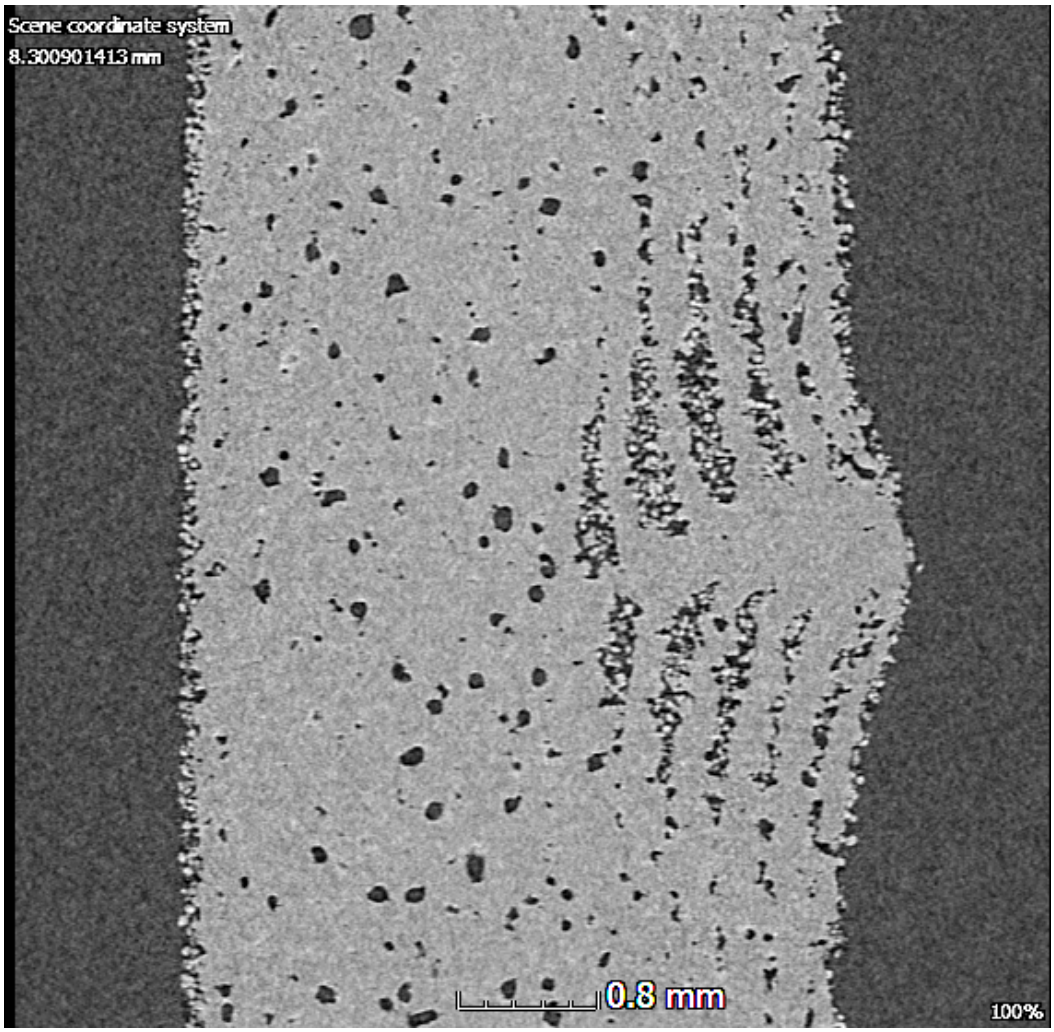

Figure 4.18. XCT slice of a tensile test specimen, produced with a bed temperature of 165 °C, a laser power of 27 W, a scan speed of 2500 mm s^{-1} and a hatch spacing of 250 µm. Build direction is from left to right

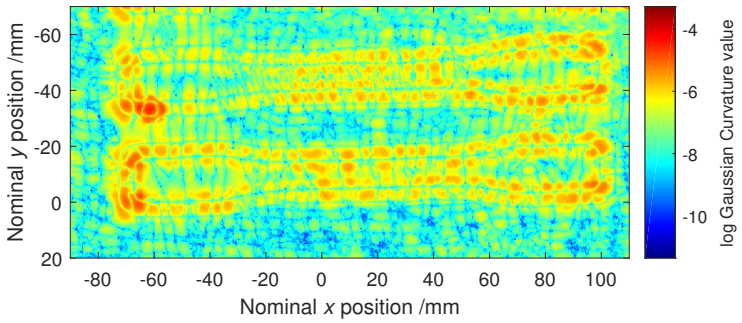

(a) Gaussian curvature

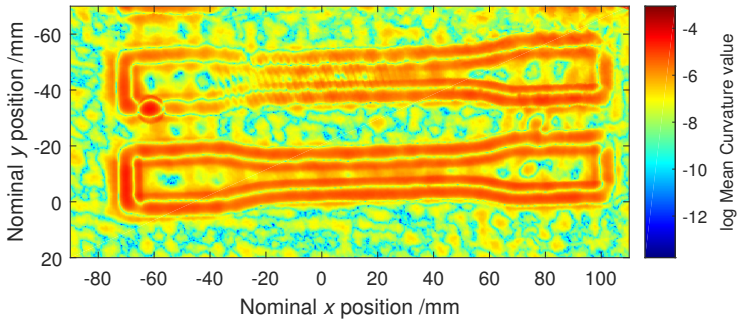

(b) Mean curvature

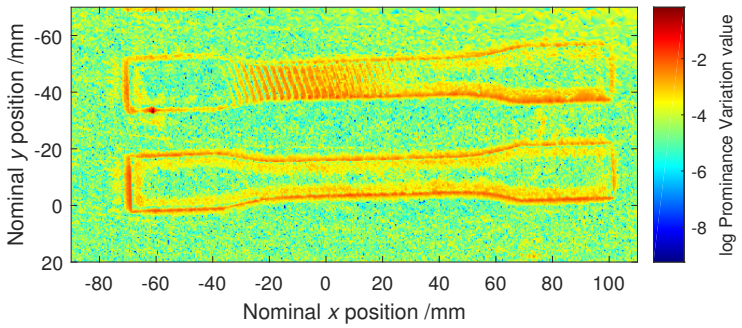

(c) Prominence

Figure 4.19. Curvature and prominence maps of layer 19 of the 27 W build. The defect is visible in all three maps, from layer 16 onwards at an approximate location of (-50, -40).

4.3 Discussion

The data analysed had pertinent process information at multiple scales and magnitudes. Powder-scale localised issues with powder spreading, section 4.2.2, were small scale and small in magnitude. Curling, section 4.2.2, was caused by issues in process parameter selection and was large scale and large magnitude. The measured drop due to consolidation, Figure 4.10, was large scale but small magnitude. Finally, the defect in the 27 W part, Figures 4.18 and 4.19, was small scale but large in magnitude.

The in-process surfaces have features at multiple scales which require multiple analysis techniques to extract relevant information from the varied features [203]. The roughly 250 µm spacing of measured points on the powder bed mean particle-level effects are unlikely to be visible in the data. However, even with the spatial resolution limitation, the process signatures and powder spreading information show that important information, such as impending part failure and poor powder spreading can be obtained. As can be seen in Figure 4.5, the transition from no visible consolidation to a build failure due to curling occurs at far lower energy densities than the builds with the most successful layers. Therefore, having just enough energy to consolidate the layer is not the optimal processing point at the specified temperature, due to severe curling. The general trend discovered was that as the temperature was increased the parts built for more layers before an error occurred. The inconsistency of results found may be due to variability in the process.

Under high-temperature conditions, it was noted that all builds had at least some degree of sintering. However, the parts created with the lowest energy density were considerably weaker than other test specimens, causing one of the three samples to break as it was removed from the build chamber. The only failure mode observed in the high-temperature processing was

polymer degradation, which can cause polymer particulates to obscure the laser glass and cause a degradation of mechanical properties.

At the lowest temperatures, successful sintering was not achieved because, when enough energy was delivered to consolidate the powder, curling caused build failure. A potential cause of this failure mode is excessive thermal differentials and rapid cooling due to a cold powder bed. In the low-temperature conditions, the parameter sets that showed no visible indication of sintering during the process also led to no sintering. Curling occurred in some builds where no sintering was visible, demonstrating that the naked eye is not always sufficient to identify whether partial consolidation has occurred in areas scanned by the laser. These results show the need for high-quality process monitoring for automated classification of the process outcomes.

It should be noted that smaller particles are preferentially heated when the laser imparts energy [204], due to the volume of polymer requiring heating being smaller. This preferential heating causes higher peak temperatures and greater chances of polymer degradation. Therefore, particle size distribution needs consideration when process monitoring and control are performed. Also, since all values for laser power and scan speed are nominal, it is conceivable that the recorded values of both deviate significantly from the actual values.

However, the mechanical testing of the high temperature process mapping shows the onset of sintering occurring at an energy density previously reported in literature, $0.012\,\mathrm{J\ mm^{-2}}$ [28, 69, 70]. Compared to previous literature, the onset of sintering visible at the dashed line in Figure 4.6 is better defined as are the issues with energy density, discussed in Chapter 2. The two sets of repeated measurements, circled on Figure 4.6, demonstrate the variability of builds since each result is the average of three tensile tests of parts from the same layer of the same build.

4.3.1 Process insights

There were no occurrences of catastrophic curling at the highest temperature builds because excessive polymer degradation (i.e. producing thick white smoke) occurs at a lower energy density than the point where induced residual stresses cause failure of the build. Even when parts were successfully built at lower temperatures, blade interactions occurred. For the build shown in Figure 4.9, the highest point of the consolidated area alternates between the left and right hand sides towards the end of the build process, when the magnitude of the curl is greatest. This pattern of data can be interpreted as the part being rocked by the blade as it spreads a new layer of powder, tipping up the end of the part over which the blade passed first. This means that when the blade returns to spread the next layer it passes over the curled end of the part previously pushed into the powder bed and then proceeds to continue spreading powder until it makes contact with the elevated side of the part. This contact pushes the elevated side of the part down. As the blade continues to spread powder the continued contact with the curled part has the effect of pivoting the other side of the part into an elevated position, because there are no support structures holding it down. This cycle repeats and can be most clearly seen in layers 27 - 30 in Figure 4.9. The inflection point in Figure 4.13b can be interpreted as a steady increase in curl as the build progress, followed by the inflection point where a different process occurs. The rocking of the part discussed in Section 4.2.2 reduces the amount of powder above the raised end when laser heating occurs. This increase the heating effect of the laser and promotes increased warping at the extreme ends of the part. The more the part rocks, the more likely it is to warp which will make the part rock more. The overall shape of the lengthwise cross sections agrees with previous literature that describes the large radius of the main curve of the part, along with increased curling at the extreme edges of a part [58,

201]. Three phenomena have been linked to curling: thermal differentials causing differential stresses; densification and shrinkage upon cooling [25, 58]. It has also been shown that the cooling rate of polymer laser sintered parts has a measurable impact on mechanical properties [205]. In contrast to the curling, which gets worse with each new layer, Figure 4.13 a) shows evidence of self-repair of a potentially catastrophic defect. This self-repair shows how the evolution of a defect needs to be understood before process control remedies can be considered. It also demonstrates how large defects could be hidden inside AM parts with little to no external indication of issues. The detection of both these failure modes is important because quick detection of a potential build failure could save significant time and cost when producing small numbers of AM parts.

Whilst not a failure mode, the heaping of powder at the edges of the produced part shows an interaction between the consolidated region and the powder spreader blade, see Figure 4.16. The exact creation mechanism is unclear but it appears that the powder forms a ramp up to warped edges of the consolidated region during powder spreading. When powder is spread over the opposite edge of the part, the reduced size of ramp suggests a powder deposition shadow. It is unclear why the ramp of powder should increase the maximum height after consolidation. Compliance of the powder bed to the part being pushed down by the powder could cause an increase in height, but the scale of powder ramp and the retained high point after consolidation seem difficult to produce with just the release of pressure after powder has been spread. Extra curling due to the border scan could produce the maximum height after consolidation, but this mechanism seems unlikely to produce the large ramp. Whilst rocking of the part due to blade interactions could produce asymmetric heights and leave powder ramps after spreading, the effect was seen in non-curled builds, and in builds with clear curl the ramp was taller than the depression of the opposite side of the

part. A combination of these described effects could potentially be the cause of the height maps seen in Figure 4.16, but further research is needed to identify the mechanism responsible.

It is interesting to note that the maximum height from nominal after layer 30 decreases faster than the lowering of the part due to new layers of powder being spread, see Figure 4.13 b). This could be the result of the thermal stresses of the part reducing as the rate of heat loss from the top surface is reduced due to the insulating layers of powder spread on top. However, without thermo-mechanical simulations of the phenomenon or powder bed penetrating measurements, it is difficult to give a definitive interpretation of the varied reduction rates of the height above the nominal.

The defect seen in the 27 W build shown in Figure 4.19 has several unusual features visible in the XCT scans of the region, see Figure 4.18. The large voids of un-sintered powder, separated by consolidated regions seem to be related to the central spike like defect that is visible from layer 19 until the final layer, 30. There are high levels of porosity in the part, but that is to be expected since the part was produced with high energy density. Without pre and post consolidation powder bed scans, it is difficult to determine the root cause of the defect. However, the origin of the defect does not appear to be a foreign contaminant such as a hair.

Of the many potential failure modes in laser sintering [25, 26], the ones directly observed in these experiments were polymer degradation, lack of sintering, catastrophic curling and excess thickness/width. These results suggest numerous avenues for future work. Repeating similar experiments on differing machines with different measurement strategies would investigate the universality and detectability of the process signatures discussed here. How surface topography evolves when defects occur is another important question. If process monitoring detects a defect in the powder bed surface, only detailed knowledge of the expected evolution of such a surface

can determine whether process control needs to intervene. This detailed knowledge can be obtained through three-dimensional measurements of the powder bed surface during the process. More detailed analysis of the built parts would help to create a clearer picture of the mechanisms by which process signatures impact final part properties. For example, the drop due to consolidation could act as an indication of consolidation success. Improved frameworks for the analysis of the in-process surface measurements are also required. One example is determining the best solutions for efficient CAD comparison and process success categorisations: without these frameworks process control cannot be reliably implemented.

4.3.2 Segmentation of point cloud data

The localised nature of the curvature calculation ignores the large scale variation present due to the undulations in the scans. Therefore, the curvature based analysis did not need a reference powder bed scan subtraction for processing of data showing the increased robustness of the method when compared to height based thresholding. However, the curvature based segmentation did struggle with the heaped powder next to parts, and the impact on segmentation of using a kernel to increase the speed of processing curvature was not investigated. Given the success of using a priori part slice information to identify consolidation regions in literature [94, 206], it could be that curvature based segmentation is best used for detecting defects in powder spreading. Curvature analysis could still be applied inside the CAD segmented region to check if any anomalous regions are inside the consolidated region.

4.3.3 Process signatures

When Zhang et al. [106]'s powder consolidation drop function, was fitted to the data from all layers apart from layers 16-24, because of the defect on layer 16, the result is as shown in Figure 4.11. The convergence rate of the experimental data is much slower than that of the model, see Equation (2.19), and the brief experimental results for polycarbonate layer thickness presented by Berzins et al. [186] [186]. It is possible that the semi crystalline polyamide melt behaves differently enough to the metal and amorphous polymer melt pools so that the simple geometric series is no longer valid. Another potential reason for the lack of fit is that the sub-optimal powder bed temperature of 165 ℃ used for the build meant that minor warping interfered with the measured drop due to consolidation. However, no significant warping was seen in the data. The approximately 10 s fringe projection scan time could contribute to a poor fit to the suggested trend. However, it would be expected that such a systematic measurement error would uniformly reduce the measured drop due to consolidation, and not change the fitting quality of the data. Finally, the differences between layer heights are smaller than the accuracy of the system, but the heights are calculated from the average of approximately 40,000 points so stochastic measurement error is unlikely to be the cause. If the experimental data's poor fit with equation 4 in Chapter 2 is due to the process map location of the build, it suggests that drop due to consolidation can indicate successful sintering within approximately five consolidated layers.

The maximum height above the powder bed appears to be a very stable process signature that only deviates from normal values when a defect has occurred. The differentiation between a random defect causing a blade interaction and systematic process parameter issues leading to curling appears simple enough for basic statistical process control methods to successfully classify, such as control charts. This process signature appears to be best

suited for immediate application into a commercial system because of the lack of analysis required to infer process state from the process signature.

4.4 Directions for further research

Despite the 250 µm spacing of measurement points on the powder bed, several process signatures and multiple process insights were gained from the measurements. It is unknown whether particle-level resolution would increase the number or quality of process signatures and insights that can be derived from in-process fringe projection data. A higher temporal resolution could capture the gradual drop due to consolidation of the heated areas. Estimates in the literature for the densification timescale of virgin polyamide 12 vary from <0.5 s [41] to 18 s [30] so in-process measurements would bring clarity as to the magnitude of this important timescale. It is unclear whether the more accurately derived Frenkel-Eshelby model was used by Haworth et al. The Frenkel-Eshelby model was used by Peyre et al. although it was erroneously referred to as the Frenkel model.

An extra scan after powder spreading but before consolidation could be beneficial for the study of some process signatures, such as maximum height above the powder bed and the difference in powder bed surface between alternating layers. This would allow for a clear distinction of which steps of the processing procedure were associated which which process signatures.

The maximum utility of in-process monitoring is when the measured process state is analysed and informs the in-process control before the next layer is deposited and consolidated. The presented measurements required delaying the sintering process and all analysis was post-process, therefore more work is needed to explore what hardware and software combinations are required to obtain real-time analysis of the in-process monitoring

data. Techniques such as graphics processor unit (GPU) acceleration of high speed fringe projection data acquisition [207] could be applied to this problem.

Jamal and Dalgarno presented computational results suggesting almost all curling occurred when the final layer was cooled down and covered in colder powder [201]. This is contrary to the trend seen in Figure 4.13 where curl gradually increases throughout the build. It is possible that their predictions are correct for minor curl, but a more detailed in-process monitoring study would be required to determine the validity of their predictions across the process map.

4.5 Conclusion

In summary, the experimental work shows that fringe projection can be used for in-process monitoring of polymer PBF to prevent structural defects forming during the build. Fringe projection can quickly detect structural defects which are potentially catastrophic to the build such as curling and irregular level drops and is, therefore, suitable for dynamic process control. The information gained during the process could be used to perform in-situ modifications of process parameters as well as to repair detected defects [183].

Curling is always undesirable and can be used as a signal that intervention is required from process control. It was, in fact, one of the strongest in-process signatures measured. However, the link between curling and final part properties cannot be easily drawn since polymer degradation occurs before curling at optimal temperatures.

The presented measurements also place bounds on the sensitivity of both direct and indirect depth measurements required for in-process monitoring

of the laser sintering powder bed. The process signatures discussed are likely to be universal across all PBF techniques, though the measurement methods required might vary across specific processes.

Fringe projection has been demonstrated in detecting both quality of consolidation and magnitude of curl through analysis of the powder bed surface topography, suggesting this technique could be incorporated into a process monitoring system for laser sintering. The commercial measurement system gave acceptable data quality for a significant area of the build, but a fully integrated system could improve both on speed of acquisition and powder bed resolution.

Chapter 5

In-process monitoring of high speed sintering with fringe projection

5.1 Introduction

To complement the data obtained from the laser PBF process, it was decided that a different polymer PBF process should be investigated with a custom designed system to see the universality of the features of the in-process monitoring point clouds. HSS was chosen because the method of polymer consolidation is significantly different from laser PBF, but it is also a commercially relevant technology with multiple machine vendors developing variants of HSS. A legacy prototype machine was available for development work, so was chosen for observation. The previous commercial fringe projection monitoring system could not be used to monitor the HSS process because of the high contrast of the surfaces and the required speed of observation, this meant that a further system was devised. A representation of the chosen HSS system, and the final monitoring solution

can be seen in Figure 5.1. An overview of the design of the system will be presented before a description of the experimental methodology and results.

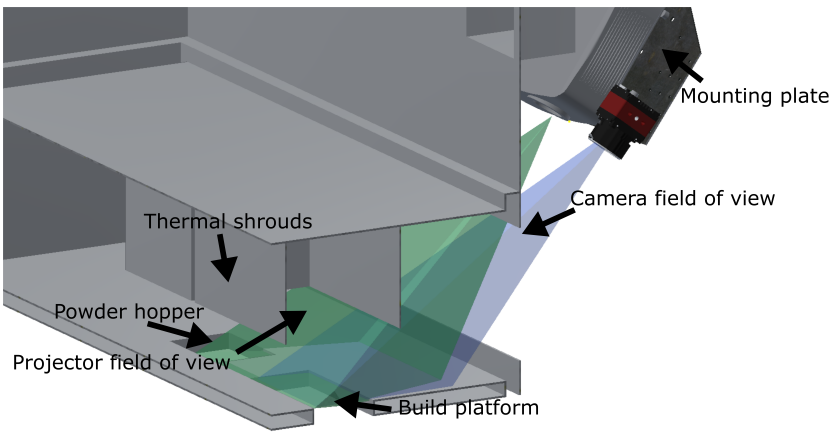

Figure 5.1. Computer rendering of the fringe projection system showing the optical constraints of the system.

5.1.1 System design

Because the HSS machine could not be monitored by the same commercial system as used for LS, a custom system needed to be designed. This required the consideration of many factors from the synchronisation with the HSS process to the optical challenges of viewing the build volume from the side.

Design constraints

The main design constraints of the fringe projection monitoring system were being able to measure the whole powder bed without interrupting the printing process, and doing so at a resolution that provided sufficient detail for analysis. A particle-scale spacing of measurement points on the powder bed was targeted, which is roughly 50 µm for most commonly used commercial grades of polymer for laser PBF. The speed of the measurement process relative to the measurement window in the HSS process is critical, as quantified by Hirsch et al. [43]. It was decided that no reduction in the

speed of part production could be justified, Therefore, the powder spreading and consolidating processes were timed and there was found to be between one and five seconds to capture the data. The HSS process produces very dark consolidated regions that have a high contrast to the surrounding powder bed. This was an important design consideration because dark surfaces reflect less light and reflected light is crucial for the measurement technique. If not enough light reaches the camera sensor, then the phase determination and all other steps that follow will have poor quality data.

There were several machine specific design considerations, mainly consequences of the machine being a legacy prototype machine. These included the fact that the HSS machine vibrated significantly at the end of each carriage stroke due to sudden carriage deceleration, and the deceleration could not be modified in the firmware. Therefore the measurements would need to be taken before the sudden deceleration, or the whole measurement system needed to be attached very rigidly. Also, the first build after a period of inactivity would fail due to curling, due to poor powder bed warm up characteristics. The heat imparted into the powder bed by the sintering lamp was often enough to allow the next attempted build to succeed due to residual heat. An occasional software bug could lead to a failed build at any point in a build, so the builds were designed with redundancy and parts aligned within the x – y plane. Another occasional error would result in a failure to consolidate a layer, presumed to be a control system error leading to the infrared lamp not turning on during the sintering pass. This type of process failure did not mean a build had to be restarted, so it was treated as an opportunity to investigate the process failure. Whilst the measurement process occurred outside the build chamber, the build removal process liberated significant quantities of powder into the machine's room, which then settled on most surfaces. Because the projector's light source was a bulb which got hot enough to need high airflow cooling, there was

a significant risk of polymer powder being passed over the hot bulb and eventually obscuring light emission. To prevent this thermoplastic powder from being melted onto the projector's bulb, a filtered airflow system was fabricated using LS for the complex shapes required to fit closely to the projector's body.

Scheimpflug principle

It was impossible to monitor from the region directly above the powder bed because there was no optical access. Therefore, projection onto and monitoring of the powder bed had to be done from the side of the machine. It was determined that the geometric constraints of the imaging system meant both the projector and camera had to view the powder bed from outside the build chamber, thus avoiding the challenges of integrating a projector and a camera into a heated build chamber. The angle needed to clearly view the powder bed, approximately 45°, was large enough that the Scheimpflug principle was needed to focus on the whole of the powder bed. With a conventional lens, the optical axis of the lens is aligned with the optical axis of the sensor, leading to the focal plane being perpendicular to the optical axis of the sensor. When viewing a plane at an angle, this leads to the depth of field volume only partially intersecting with the object plane. If the optical axis of the lens is rotated with respect to the imaging sensor's optical axis, the region of focus can be angled and translated with respect to the imaging sensor's optical axis, see Figure 5.2. It is, therefore, possible to image an angled plane and see the whole surface in focus, providing the camera positioning is accurate enough for the wedge of focus of the system. This makes it possible to collect in-focus fringe projection data across the powder bed.

The chamber window of the HSS system provided a clear view of the powder bed, but also functioned as access to the build chamber for the

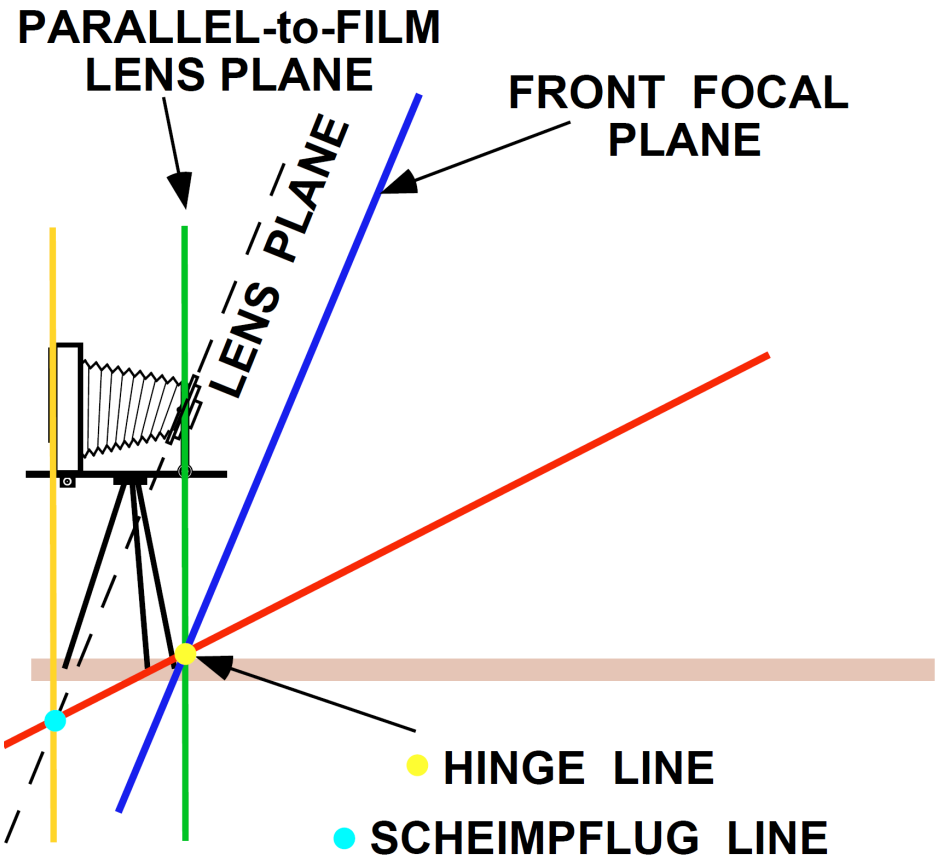

Figure 5.2. A simplified diagram of the Scheimpflug principle. Reproduced with permission from [208].

removal of completed builds. Therefore, the monitoring equipment could not interfere significantly with the operation of the door. This required either a dynamic sensor mounting solution that moved into place once the door was closed, or a static sensor solution that did not prevent the door opening to a roughly horizontal position. Whilst the latter solution did represent a reduction of work space for operators, it was decided it was an acceptable inconvenience. If this concession had not been made, only a dynamic sensor mounting would have been possible for viewing the powder bed. This was discounted because mounting the monitoring system to the door could have twisted the steel frame surround and shattered the glass with the approximately 10 kg of equipment, see Figure 5.1. The available optics for the system resulted in the camera's field of view covering a region slightly larger than the HSS build region whilst the projector's field of view extended further in all directions. This can also be seen in Figure 5.1.

Choice of camera

There are both industrial and consumer cameras that would be suitable for the fringe projection system. Consumer cameras are generally cheaper than industrial cameras with similar specifications, but lack the ability to load captured images into the computer's memory, saving to the hard drives instead. This would have increased the time to process images to an unacceptable level and an industrial camera was chosen. The next design choice was the camera sensor specifications.

When designing the optical metrology system, the camera sensor was an integral part of the design calculations as an increased number of pixels has the potential to increase the resolution of the fringe projection system. However, for the same overall size of imaging sensor, more pixels on a sensor will mean the individual pixels are smaller. Smaller pixels reduce the incident

light flux, which reduces the performance of a fringe projection system due to a reduced signal to noise ratio. Smaller pixels also mean a smaller depth of field because the acceptable blurring, or circle of confusion, is reduced in size for smaller pixels. Finally, having more pixels does also increase processing time for all operations after image capture. Despite the potential issues with a higher resolution sensor, it was decided to maximise pixel count to aim for particle level resolution on the powder bed. The speed of image acquisition aimed for was four frames per second, allowing for temporal unwrapping techniques to be used in the measurement time available. The area of imaging sensors mainly come in standard sizes, ranging from those found in devices such as smart phones and tablets (representative diagonal measurements would be 3 mm to 6 mm), up to those found in dedicated professional digital cameras (representative diagonal measurements would be 15 mm to 27 mm). Full-frame imaging sensors, so called because of the image sensor's dimensional similarity to film stock, are the largest commonly available sensor size. They were chosen as the target specification because the larger pixel area allowed for a better signal to noise ratio.

Method of fringe pattern production

It is possible to perform fringe projection with an interference grating and precision actuation but the flexibility of digital fringe projection leads to it being chosen over analogue fringe creation because it allows for greater freedom in pattern encoding strategies. Digital fringe projection can suffer from errors due to pixel quantisation [171], but the ability to project arbitrary digital patterns was seen as more important to the fringe projection process.

There are several common ways for consumer digital projectors to project an image. Digital light processing (DLP) uses a digital micromirror device (DMD) to project greyscale images. Colour is achieved with either a colour

wheel or using three separated coloured light sources with separate DMDs whose light paths are integrated together before being projected. A colour wheel has segments with different coloured filters that are spun through the optical path of the projector to impart their colour on the white light passing through. A minimum of three segments (red, green, blue) are required but it is common for other colours to be present to improve the appearance of the projected image.

The mirror based, DLP, projection method has two main advantages over other consumer projection techniques. The fill factor is very high in DLP [162], which is the percentage of every pixel site that actually reflects light for the image. Also, because the reflectivity of the mirrors is high the contrast between an on pixel and an off pixel is high compared to competing techniques [209]. This increases the signal to noise ratio of the images captured which improves the quality of the calculated phase.

The light source is an important component of the projection system. The most common light sources are high pressure mercury vapour lamps, or the related metal halide lamps. They have a spectral range that includes some ultraviolet and little infrared. An alternative bulb chemistry is xenon, whose spectral range has very little UV and a significant proportion of near infrared radiation. The amount of thermal energy delivered to the powder bed is an important consideration. Therefore, DLP is a suitable technique for structured light projection, as long as the imaging exposures are longer than several rotations of the colour wheel or they are synchronised with the colour wheel.

Organisation of the measurement system

It was decided to separate the co-ordination of fringe projection and triggering from the capture of and processing of images. This reduces the

possibilities of variable processing times impacting the correctly timed capture of fringe projection images, because each set of images was buffered in the camera before being processed by the computer program. The buffering meant that even if the Matlab script requested the images after the next layer's monitoring had begun, they would be successfully transferred. A Raspberry Pi 3B+ was chosen for the triggering of the camera because of the modest computational load of displaying the fringe patterns at the camera refresh rate 1920 $\times$ 1080 progressive scan (1080p). There was also a need for interfacing with optical sensors to ascertain the position of the HSS carriage, which the Raspberry Pi could accomplish simply.

The Raspberry Pi ran a Python script that confirmed the camera was available to capture an image, then projected each fringe image in succession, triggering the camera and waiting until the camera exposure had finished before proceeding to the next fringe pattern. Sensing where the print head was throughout the build was achieved with a pair of optical distance sensors pictured in figure 5.3. The Matlab script waited for a set of fringe patterns to be captured before saving the images to the hard drive. This was needed because the time taken to calculate the phase and unwrap it for each frequency was longer than the temporal measurement opportunity. This required the point cloud scans to be calculated after the process because the Matlab script would not be able to capture each new set of fringes. Due to the value of the unwrapped phase of each pixel being independent of all other pixels the temporal phase unwrapping technique is suitable for translation to a GPU for processing. By processing the captured images with a GPU it could help make the analysis possible in-process but this is beyond the scope of this work.

5.1.2 System specifications

A 26.2MP Allied Vision GigE camera, GT5120 monochrome global shutter industrial camera, pixel size of 4.5 µm, was used with an Optoma HD142X projector. The DLP projector was a consumer model that cost approximately £500. The camera had a maximum frame rate of 4.59 with a default 8 bit monochrome colour depth. Colour depth refers to the number of intensity levels possible in an image, with 8 bits giving 256 levels and 10 bits giving 1024 levels. Using the 10 bit recording option halved the camera's maximum rate of capture. The lens used on the camera was a Lensbaby Edge 80 (80 mm focal length) tilt lens, to enable the whole of the powder bed to be in focus, as discussed in Section 5.1.1. The lens aperture was set to f/16, the camera was tilted to about 50° from horizontal, with a 12° pan to the right. The lens was tilted vertically to approximately 15°. This meant the hinge point of the wedge of focus was roughly 420 mm below the camera, which coincided with the plane of the powder bed surface. This gave a theoretical angular depth of field of about 3°. A focus pattern was printed by the HSS system onto the powder bed for verifying camera focus. A projected pattern could not be used because the projected image was not in focus across the field of view of the camera. The droplet spacing on the powder bed of the printed pattern was 70 µm, roughly twice the camera pixel spacing of 30 µm on the powder bed. This did not appear to be an issue since it was not possible to resolve individual droplets in the pattern. A picture of the completed system can be seen in figure 5.4

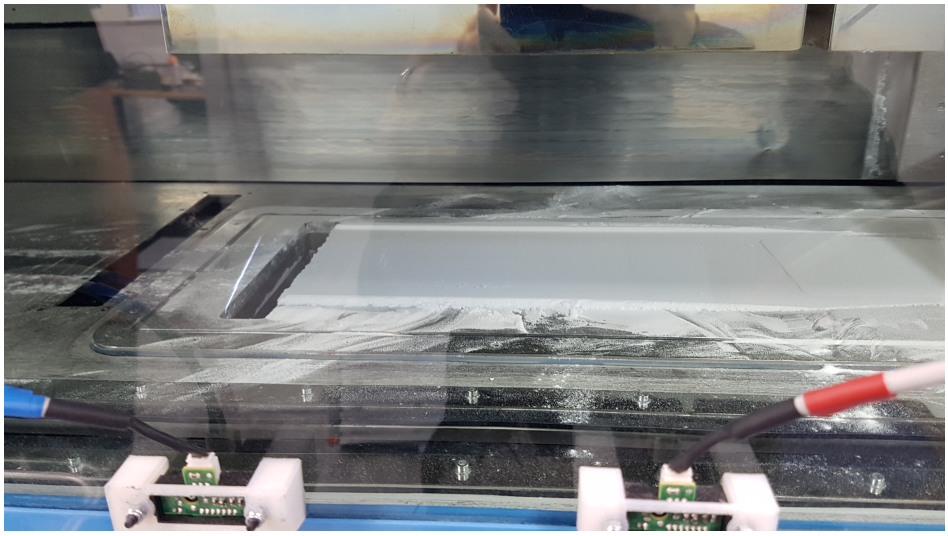

Figure 5.3. The optical distance sensors for triggering the measurement process. Sensors were placed in custom 3D printed housings and the housings were attached to the glass access door with double sided adhesive tape.

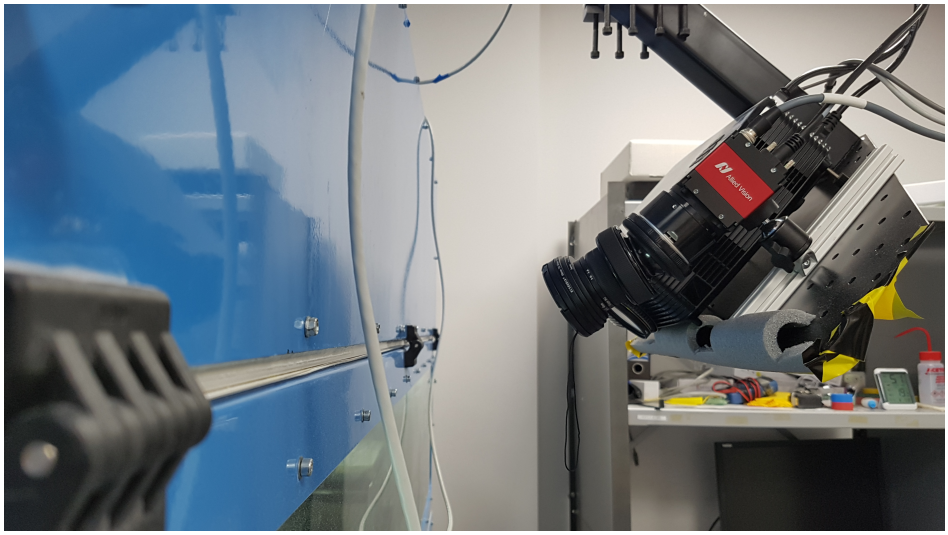

Figure 5.4. The fringe projection monitoring system attached to the HSS system. For monitoring the HSS build, the system was moved closer than pictured to reduce vibrations caused by the powder recoating mechanism. The filtered airflow system was not fitted at the time of the picture, but was installed for monitoring.

5.2 Methodology

In order to investigate if process signatures can be detected in HSS, point cloud surface measurements of the powder bed were collected during a build consisting of the same geometry produced multiple times with one HSS processing variable changed.

5.2.1 Fringe projection measurements

Point cloud surface measurements were made of the in-process powder bed twice per layer, before and after sintering. Whilst the system could also measure the powder bed surface, the contrast between the white powder and the black consolidated regions surpassed the dynamic range of the camera, therefore the consolidation performance was chosen for evaluation because of the greater insight into the sintering process. After the powder spreading stroke occurred, the mainly white powder bed could be measured by displaying the fringe patterns for a fraction of the camera exposure time, preventing overexposure of the captured images. A fringe image was displayed for at least one frame (16.7 ms), followed by black frames, emulating a shorter camera exposure time which meant that the captured images were not overexposed.

5.2.2 Acquisition parameters

Due to the low contrast of the projected fringes on the consolidated regions, the exposure time of the images had to be increased to 0.5 s, allowing for a combination of three high frequency and six low frequency fringes to be projected on every sinter stroke. The chosen temporal unwrapping approach was number theory and the high frequency fringe patterns had 59 fringes across the projector's image, whilst the low frequency fringe patterns

had 11 fringes across the projector's image. The low frequency fringes had more phase shifts to compensate for their greater phase noise, because number theory unwrapping requires both frequencies to successfully phase unwrap. The longer exposure time also allowed for a smaller aperture thus increasing the depth of field to cover most of the powder bed. In contrast the powder spreading stroke was captured with three low frequency and three high frequency phase shifts because the measurement window was shorter. The minimum time required to collect the fringe projection images meant that some powder bed movement could occur during image capture which led to possible sources of noise in the measurements.

5.2.3 Build layout

Two geometries were chosen for builds to maximise the potential process insights possible through analysis of the in-process powder bed surface measurements. All geometries were weighed after manual powder removal, with scraping of partly sintered powder particles being required.

Tensile test specimens

In order to test the mechanical consequences of the varied build parameters, tensile test specimens were built and tested. Because of the small build volume of the HSS system, reduced size tensile test specimens were arranged in pairs in twelve stacks with a density-artefact in between, see Figure 5.5. Each set of parts was separated by 20 unconsolidated layers of powder. Labels were applied in relief to all specimens to denote both position in build and layer number. The labels were applied to the clamped regions of the tensile test specimens to minimise any potential effect on the mechanical properties of the produced specimens.

Density-artefacts

To complement the mechanical testing, density-artefacts were designed to be built alongside the tensile test specimens. They were sized to fill space between the gauge lengths of the tensile specimens, whilst not interfering with their successful consolidation. Four spheres were placed in the middle of the rectangle's corners to aid with post-process dimensional measurements, since measuring a sphere's centre averages out many systematic and stochastic error sources. To reduce ambiguity due to rotational symmetry, the diameter of one of the spheres was made smaller. To simplify fixturing for measurements, the centres of the spheres were moved so that a plane was formed by the sphere surfaces when placed on a flat surface. The density-artefacts were measured with a Nikon MCT225 computed tomography system, with a voxel size of approximately 20 µm. However, issues with data processing meant the volumes of the samples could not be calculated.

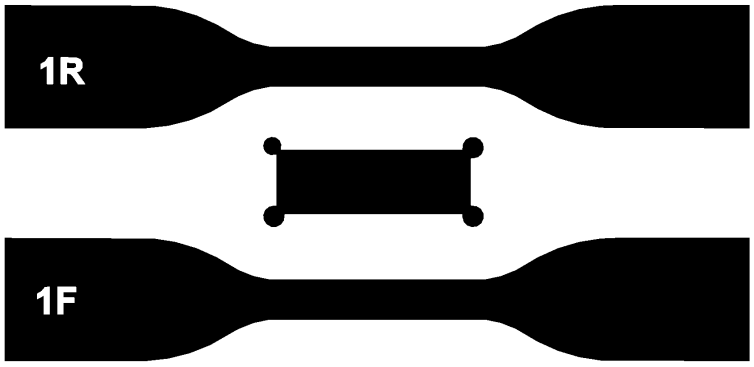

Figure 5.5. Bitmap used for ink deposition for one of the layers of the first set of geometries built. Labelling was used to notate orientation, position (F for front, R for rear of build chamber) and repeat number. The density-artefact did not require labelling because of the lack of rotational symmetry of the part.

5.2.4 Processing parameters

The polymer used in the builds was a semi-crystalline thermoplastic elastomer (TPE) with an average particle size of about 70 µm. Previous successful processing of the polymer had achieved ultimate tensile strengths of approximately 8 MPa and elongation at break of over 100 % and up to 200 %. A droplet volume coverage of 6000 pL mm^{-2} was considered the optimal processing parameter for the material due to previous process experience. To investigate the relationship between this variable and consolidation, the droplet volume coverage was varied between 2500 pL mm^{-2} and 8000 pL mm^{-2}. For the blank layers separating the stacks, the sinter stroke lamp output was set at 50 %. This kept the powder warm before the next layer of powder was spread on top. The processing parameters for each successive layer of parts in the build can be seen in Table 5.1. The build was arranged into two sections, with nominally optimal processing parameters used for control builds at the beginning, in the middle and at the end of the overall build. Each section had the same parameter sets, but the order was randomly assigned. This approached reduced the impact of confounding effects from the overall position in the series of builds, or the parameter sets of the neighbouring build. It was expected that poor system thermal mass would lead to a weakly consolidated first stack. This was accounted for by building two repeats of the control parameters at the beginning of the build.

Every HSS layer had a powder spreading stroke followed by a print and sinter stroke. If the layer was blank with no regions to consolidate, the infrared heating lamp still turned on to heat the powder bed surface up to temperature, ready for the next layer of powder to be spread. The selected TPE powder required the blank layers between parts to have a 50 % sintering lamp intensity to prevent the powder sticking to the roller. The cohesive nature of the powder meant that the roller occasionally dropped small heaps of fresh powder onto the consolidating regions, which could

Stack number	Droplet Volume / pL mm^{-2}
1	6,000
2	6,000
3	2,500
4	3,500
5	8,000
6	4,500
7	6,000
8	8,000
9	9,000
10	2,500
11	3,500
12	6,000

Table 5.1. Processing parameters for the HSS builds.

embed partially consolidated polymer particles into the bulk of the part, see Figure 5.10. The small heaps of powder were clearly visible against the darker, printed and consolidated regions which meant they could be easily detected in both visible and near IR images of the powder bed surface.

5.2.5 Thermal monitoring

Over the course of the build, temperature measurements were recorded as part of the standard build logging for the HSS machine. Temperatures were recorded for the powder bed surface and several locations around the machine, including the walls of the build chamber. An infrared camera also captured an image from above the powder bed after every powder spreading or sintering pass. This provided a record of the state of the powder bed for every layer, but was not calibrated so could not give thermal distribution across the powder bed surface.

5.2.6 Tensile test measurements

All tensile tests were carried out with a Tinius Olsen 5ST, with a 5 kN load cell and an extension rate of 50 mm per minute, using the bundled laser extensometer. The extensometer required reflective stickers to be applied to the tested parts to track true strain. Mechanical testing of parts occurred five days after being produced due to the availability of the tensile testing equipment.

5.2.7 Data management

An important consideration when manipulating the produced data was the amount of data produced per build. A typical full build with 666 layers was found to create about 500 GB of image data alone. It is clear that long term use of such a system would require efficient data storage techniques with only the most relevant in-process data stored long-term. The raw images would likely be discarded once processed, although an average illumination image for each stroke could be kept for visual inspection after the build. If the phase unwrapping was shown to be robust over a wide range of builds, the wrapped and unwrapped phase maps could also be discarded, leaving just the point clouds for each stroke. This would reduce the stored raw data to 390 GB per build, which could still be an issue with frequent builds or multiple PBF systems with in-process monitoring. Therefore, long term use of the in-process monitoring system would require careful planning for the infrastructure needed for the storage, backup and distribution of the collected data.

5.2.8 System calibration

A rigorous setup procedure was followed to ensure the camera and projector were in the optimum positions and correctly focused before calibration occurred. First, the projected region was centred and levelled, with the focus adjusted to be across the centre of the build area. If the projector was perpendicular to the powder bed, it could be used to project a focusing pattern to confirm the camera focus. However, since the projector was not in focus across the whole powder bed due to the angled projection as explained in Section 5.1.1, a pattern had to be printed onto the powder bed to aid focusing.

Calibration was performed using a method similar to that outlined in Zhang [162]. A chequerboard reference target was imaged in multiple orientations to allow for the intrinsic and extrinsic parameters of both camera and projector to be determined. The extrinsic parameters describe the pose and position of the imaging system, whilst the intrinsic parameters describe the characteristics of the imaging systems. The intrinsic parameters described a pinhole model of both camera and projector, as well as image distortion models for both. The image distortion models used were [210]. The chequerboard used was a precision manufactured ceramic plate with square sizes of 20 mm. One minor modification of standard chequerboard calibration procedure was to use the centres of the white squares for phase map data, not corners. This was because the dark regions of the chequerboard had unacceptably high levels of noise. Therefore, when the stereo camera calibration was performed, the calibration points were the centres of the white squares instead of the normal intersection points. To ensure a robust calibration, the target was imaged in a wide range of positions. The wide range of calibration target positions led to large number of erroneous phase jumps, so linear interpolation was used to correct erroneously unwrapped calibration points. Calibration can be evaluated by reprojecting

the best-fitted location of the calibration chequerboard poses back into the camera and projector's pixel-space. The difference between the measured chequerboard centre location and the reprojected centre is a measure of both the accuracy of the measuremnt system and the sucess of calibration. Calibration results had pixel reprojection errors that corresponded to point measurement uncertainty of approximately 20 µm. This is well within the requirements for powder-scale measurements.

It should be noted that this calibration approach is almost identical to that commonly used for stereo camera pairs, except the projector's co-ordinates used are the horizontal and vertical phase (which are an indirect measure of the projector's pixel co-ordinates). Once calibration was completed, unwrapped phase data could be converted into calibrated real-world co-ordinates using Equation (5.1). The derivation is covered by Zhang [162].

$$\begin{bmatrix} x \\ y \\ z \end{bmatrix} = \begin{bmatrix} h^c_{11} - u^c h^c_{31} & h^c_{12} - u^c h^c_{32} & h^c_{13} - u^c h^c_{33} \\ h^c_{21} - v^c h^c_{31} & h^c_{22} - v^c h^c_{32} & h^c_{23} - v^c h^c_{33} \\ h^p_{11} - u^p h^p_{31} & h^p_{12} - u^p h^p_{32} & h^p_{13} - u^p h^p_{33} \end{bmatrix}^{-1} \begin{bmatrix} u^c h^c_{34} - h^c_{14} \\ v^c h^c_{34} - h^c_{24} \\ u^p h^c_{34} - h^p_{14} \end{bmatrix} \tag{5.1}$$

where x,y,z are the Cartesian co-ordinate outputs of the equation, h^c_{mn} is an element of the camera parameter matrix, h^p_{mn} is an element of the projector parameter matrix, (u^c, v^c) are the camera pixel co-ordinates of the feature in question and u^p is the projector's co-ordinate that is parallel to the projected fringe patterns.

5.3 Results

In general, the fringe projection data collected was noisy with significant issues, hampering conversion into point clouds. Extensive processing was

attempted to reduce the impact of this noise and retrieve unwrapped and 'de-noised' point clouds. This was unsuccessful, but whilst the custom designed fringe projection monitoring system did not produce good quality point cloud data, the data collection process was validated and sources of future improvements identified.

5.3.1 Calibration

The calibration of the system was achieved by calibrating the camera and projector separately and then estimating their relative poses and translations. The linear interpolation post-processing of the fringe projection data, see Figures 5.6 and 5.7, increased the number of poses that could be used for projector calibration. This enabled the calibration optimisation algorithm to process more of the poses and therefore produce a more accurate result. The extrinsic estimations for both camera and projector are seen in

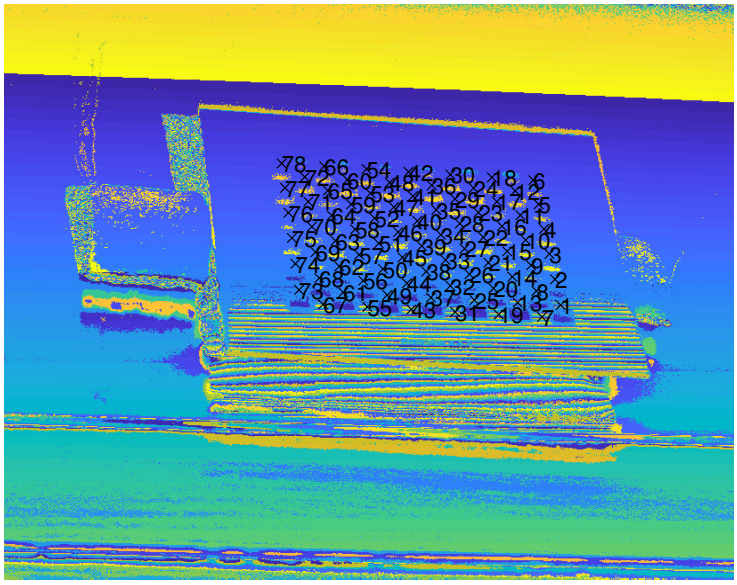

Figure 5.6. Horizontal phase for calibration pose 24. Data was collected with sinusoidal fringes and 24 phase steps. The colour corresponds to phase. The centres of the white squares on the chequerboard are numbered to aid comparison between this figure and Figure 5.7.

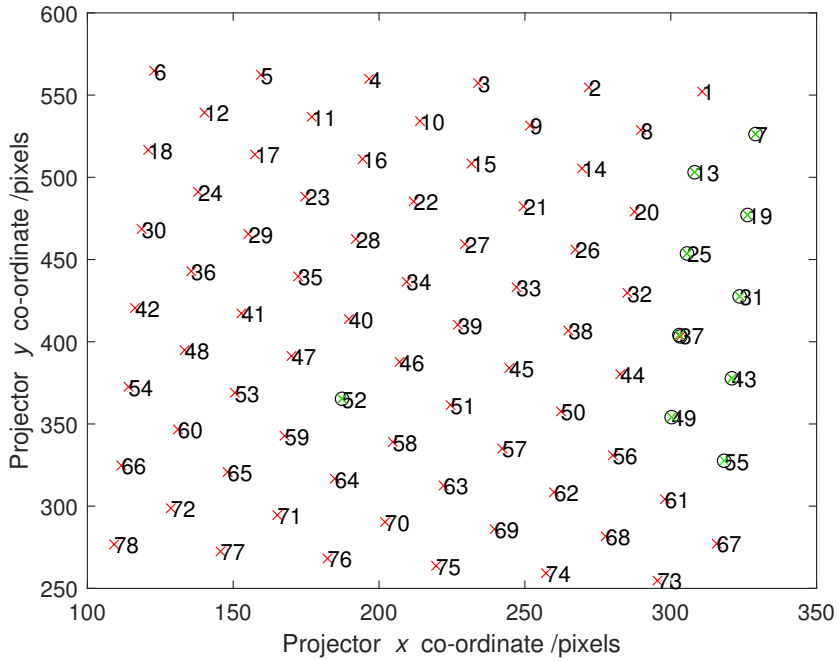

Figure 5.7. Co-ordinates for the centres of the white squares on the chequerboard, including interpolated results. The red crosses are the unaltered phase values as measured from Figure 5.6 and the corresponding vertical phase map. Green crosses in black circles are points which have been linearly interpolated to correct for erroneous phase values. Areas with both a red cross and a green cross are points where linear interpolation suggested a similar phase value so the original measurement was used.

Section 5.3.1. It is clear to see the more limited range of poses that were suitable to use for projector calibration. The reprojection errors across all poses used for both camera and projector can be seen in Section 5.3.1. The reprojection errors are higher than desirable for the projector, but they are good for the camera.

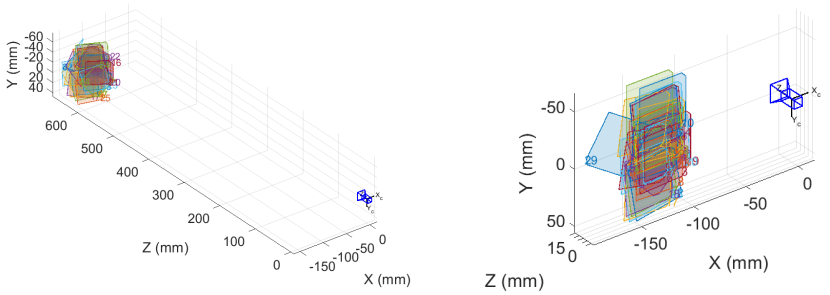

(a) Visualisation of the reference target positions relative to the camera.

(b) Visualisation of the reference target positions relative to the projector.

Figure 5.8. Estimation of extrinsics for calibration. The numbering for both figures is not equivalent because not all usable camera images could be processed successfully for projector calibration. The projector is incorrectly displayed as rotated away from the calibration board poses.

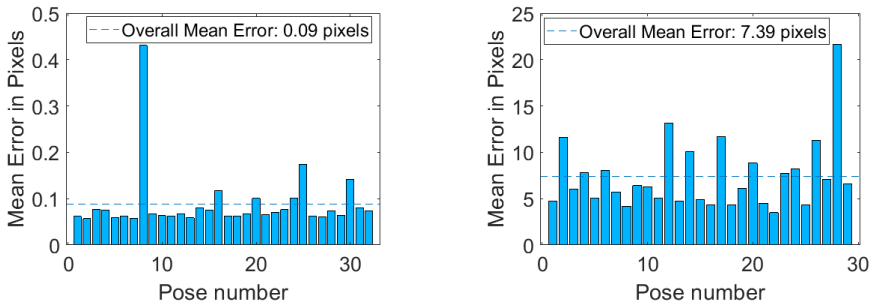

(a) Camera reprojection errors per pose after calibration.

(b) Projector reprojection errors per pose after calibration.

Figure 5.9. Root mean squared reprojection error per pose after calibration. The reprojection errors for the projector are significantly higher those for the camera. Sub-pixel reprojection errors should be achievable for most imaging and projection.

5.3.2 High speed sintering build

The thermal measurements collected during the HSS build showed unstable thermal control, with cyclical application of high levels of heating

followed by no heating applied at all. This rapidly varying thermal environment could impair mechanical properties of produced parts because of the varying thermal environment for consolidation. Figure 5.10 shows the infrared image of the powder bed after the sintering stroke on layer 39 of the build. All the infrared images show a darker region in the top left of the images, indicating that the back left of the build was the coldest part of the powder bed throughout the build. No hot spots were observed, which would be an indication of poor processing parameters.

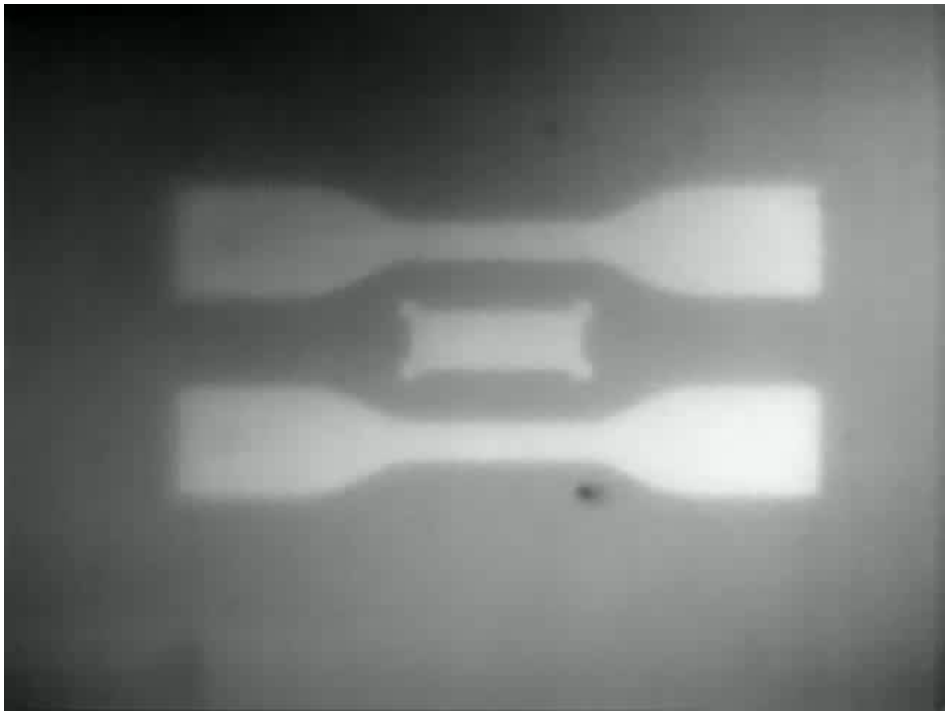

Figure 5.10. Infrared image of the powder bed after the sintering stroke on layer 39 of the build, the 18th layer of the first set of parts. The small dark region near the front is an agglomeration of cold powder that fell off the powder spreading mechanism during the sintering stroke.

5.3.3 Produced parts

All the tensile test specimens produced were destructively tested. The variation in the density-artefact calculated densities can be seen in Figure 5.11. Whilst the variation in density is small, the trend of higher densities for higher droplet volume coverage is expected because more deposited

ink should increase the consolidation of the part. The variation between repeats does not seem to follow a trend. The variation in the density-artefact calculated porosities can be seen inFigure 5.12. The first two stacks have higher porosities than any other stacks, which is expected because there is minimal residual heat in the powder bed during the first layer of parts in polymer PDF. Taking the rest of the stacks, the porosities halve as the droplet volume triples to go from the minimum droplet volume coverage to the expected optimum droplet volume coverage. As the droplet volume increases further, the porosity increases again potentially as the parts over-sinter. The relationship between drop volume coverage and mechanical properties is shown in Figures 5.13 and 5.14. The differences between the two tensile test specimen positions are also indicated. Four specimens were built with the same droplet volume coverage of 6000 pL mm^{-2}. The variation between the four pairs of 6000 pL mm^{-2} specimens built shows the large amounts of variation possible throughout a polymer PBF build. The first pair weighed less, had a lower ultimate tensile strength (UTS) and had a lower elongation at break (EaB). The second pair improved on the first pair for all these properties but did not reach the increased performance seen in the third and fourth pairs of specimens. As expected, this shows that the local thermal environment, especially radiant heat from consolidated parts cooling down, has a large impact on part mechanical performance of a part. The UTSs of the tensile test specimens, see Figure 5.13, built at the front of the build chamber are consistently less than of their counterparts built at the back of the powder bed, indicating different powder bed thermal environment for the parts. The EaB of the specimens follows a similar trend though it is less consistent. Taken all together, the graphs suggest that the optimum droplet volume coverage is between 4500 pL mm^{-2} and 6000 pL mm^{-2}.

5.3.4 XCT measurements

XCT measurement were taken of all twelve density-artefacts, but unforeseen circumstances meant that only their densities and porosities could be calculated. It should be noted that XCT measurements of porosity and density are reliant on determining the location of pores, surface and ignoring scanning artefacts. Therefore, whilst the relative densities and porosity trends are likely to be correct, their absolute values might not be. XCT measurements did reveal low concentrations of particles of a higher density distributed evenly inside parts. This is likely an additive to improve the processability of the polymer powder.

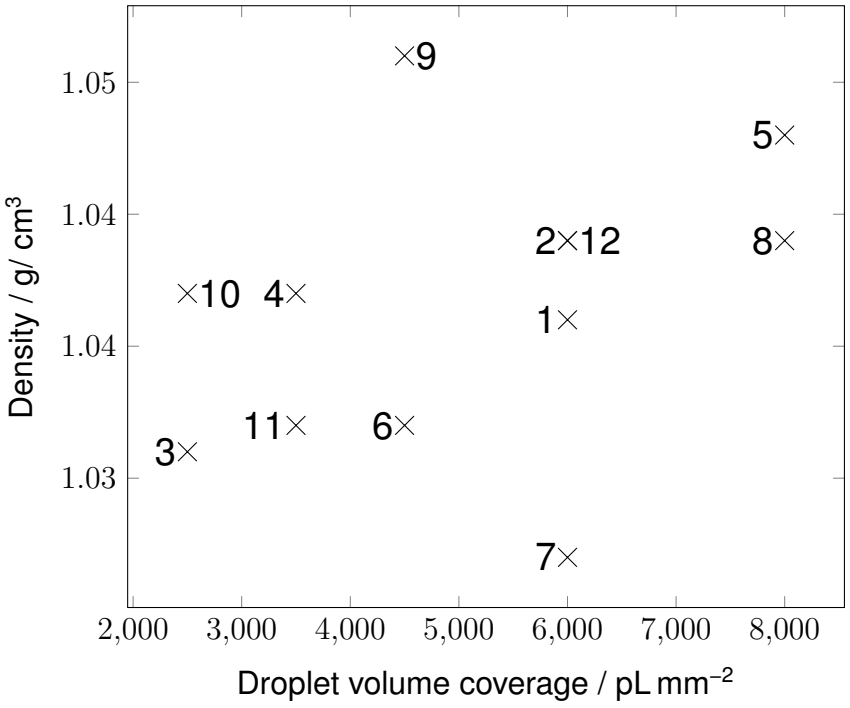

Figure 5.11. Variation of density-artefact density with respect to droplet volume coverage.

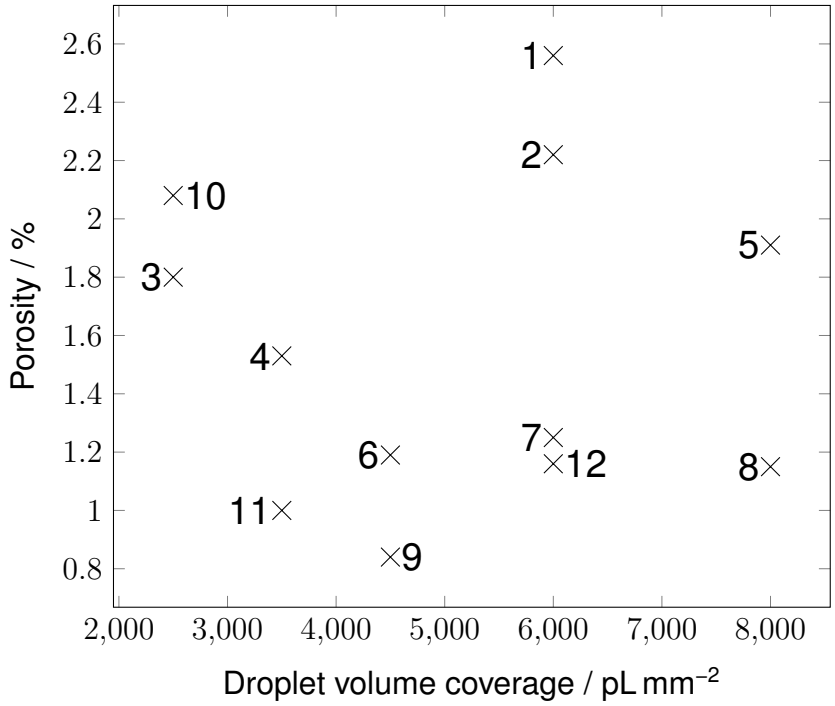

Figure 5.12. Variation of density-artefact porosity with respect to droplet volume coverage.

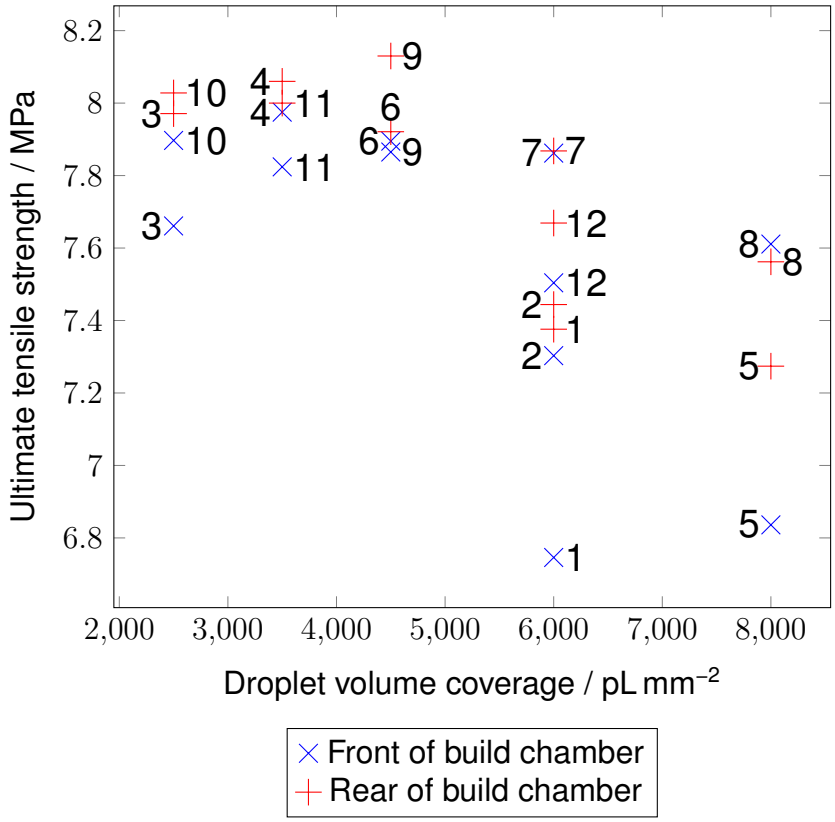

Figure 5.13. Variation of ultimate tensile strength with respect to droplet volume coverage.

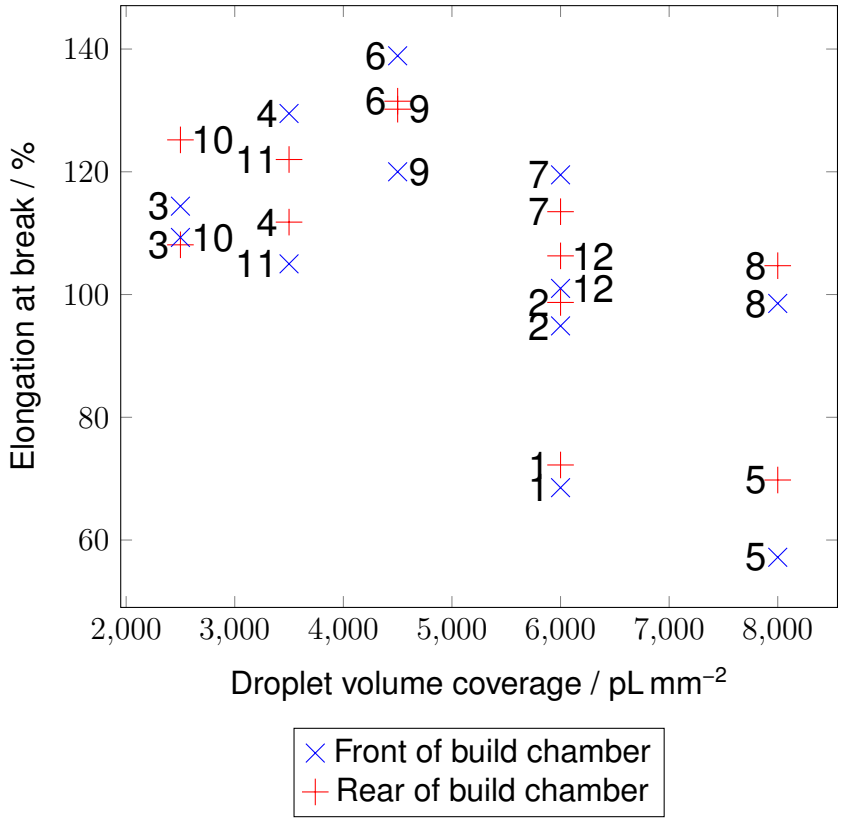

Figure 5.14. Variation of tensile test specimen elongation at break with respect to droplet volume coverage.

5.3.5 Images captured

The images were captured and then the phase was calculated from the multiple phase shift images. Selected steps in this process can be seen in Section 5.3.5. There were some fringe images that contained incorrect patterns, see Section 5.3.5, however this was infrequent and did not appear to be the cause of the phase noise issues for all layers because the phase noise appeared equally bad in images where no pattern display issues had occurred. The in-process data captured required significant post-processing to attempt phase unwrapping. There were some portions of the image that were over exposed, and the low frequency fringe images had higher apparent noise than the high frequency images as expected [163]. Fourier transforms of the powder bed images were performed, to better visualise the information in the images as well as to check for issues with gamma calibration. The sintered layer images, as well as powder bed images, were excluded from analysis because the sudden intensity changes around the sintered regions would mask spectral features related to the quality of the optical path (the projected fringes reflecting off the powder bed and onto the imaging sensor).

The projected fringes have a clear structure with maximum variation in a direction close to horizontal across the image. This is seen as a bright spot in the frequency (absolute) component of the Fourier transform, distinct from the DC peak. The first harmonic of the fringe appears at twice the distance from the DC peak in the same direction, with further harmonics continuing as shown in Figure 5.17 a) and d). Image processing techniques were used to enhance the contrast of the log-scaled absolute of the Fourier transform of the images. Thresholding and blob detection then identified the DC peak, the peak due to the fringes, and then to threshold out the central DC peak, the peak due to the fringes and the harmonics along the ‘line’. Filters for removing the harmonic peaks were constructed by convolving the binary

(a) Image captured on sinter stroke of the second layer of stack 7. The row of the image marked is used for the subsequent parts of this figure.

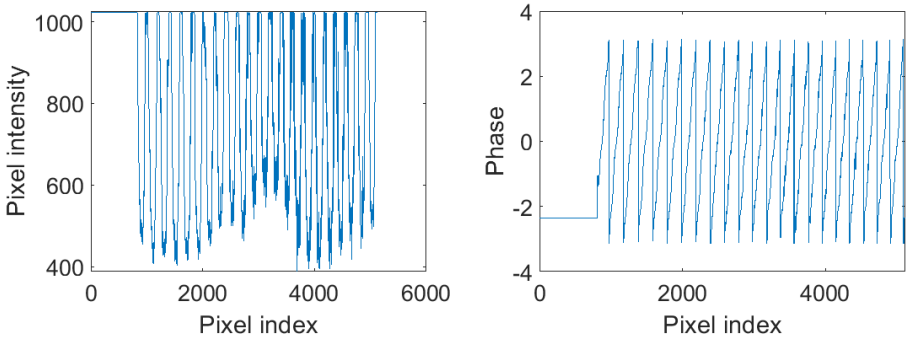

(b) Pixel intensity across the front tensile test specimen. Significant portions of the image are over exposed.

(c) Wrapped phase for the same row as above.

Figure 5.15. An overview of the image capture process

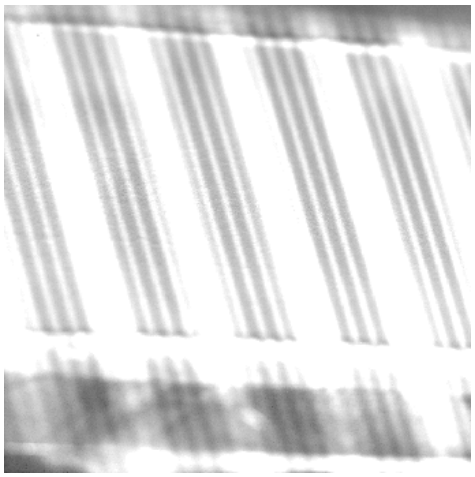

(a) First phase shift high frequency fringe image from layer 1. The high frequency fringe pattern is modulated by the low frequency fringe pattern.

(b) First phase shift high frequency fringe image from layer 22. The image is overexposed, but the layer before was correctly exposed.

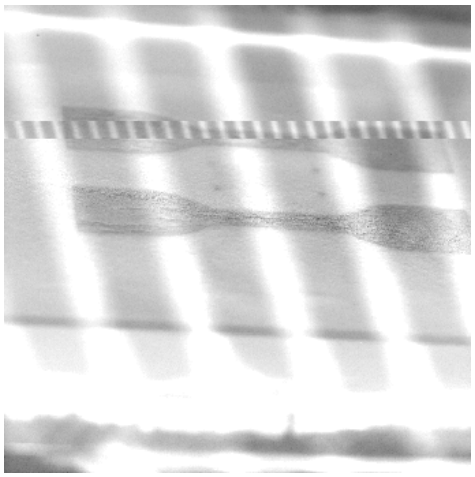

(c) First phase shift low frequency fringe image from layer 647

Figure 5.16. Fringe pattern projection errors observed on sinter strokes. Almost all observed pattern projection errors were seen on the first phase shift of a pattern.

masks with a Hann window to prevent ringing caused by sharp transitions in the filter. Therefore, the projected fringes could be given a bandpass filter for just the fringes (for improved number theory unwrapping), as well as filtering out the contribution of the harmonic peaks (which could be safely assumed to be an artefact related to the fringes because of the harmonic sequence of peaks). Powder stroke images had a more complete image of the powder bed surface with better signal to noise characteristics, see Figure 5.17.

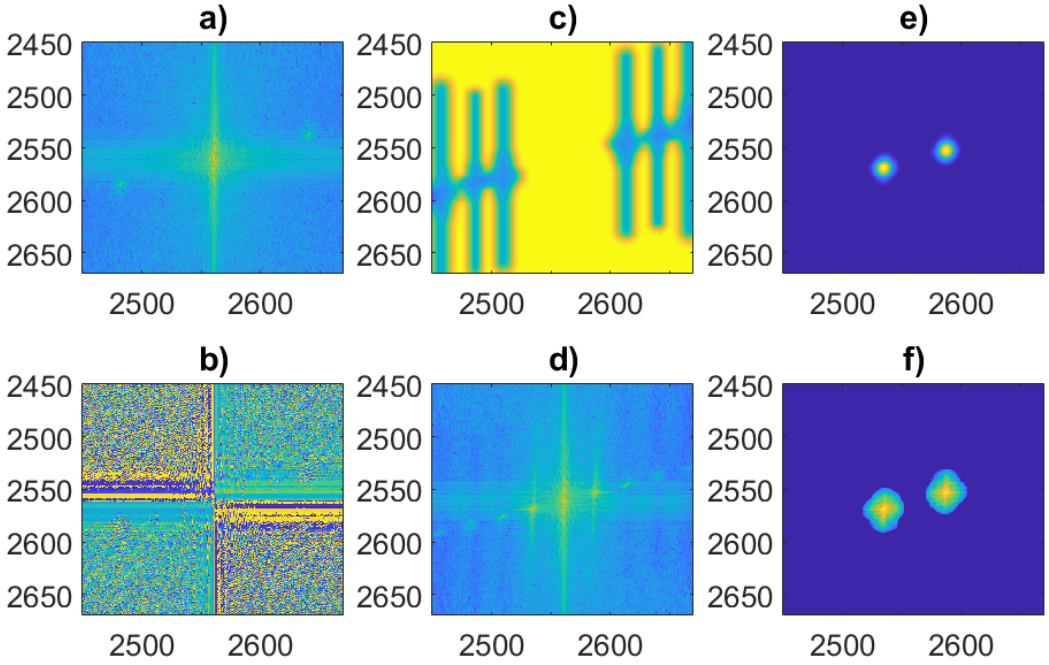

Figure 5.17. Fourier space filtering of a captured fringe image for the first powder stroke of stack 7. a) The log-scaled absolute component of the Fourier transform of the fringe image, zoomed into the central region. All images have had the DC peaks shifted to the centre of the image and share the same axes limits. All axis labels are pixel co-ordinates for the images. b) Phase component of the transform of the fringe image. c) Constructed Fourier-space filter to extract the contribution of the fringe's harmonic peaks to the image. d) The log-scaled absolute component of the Fourier transform of the Fourier-space filtered fringe image. e) Constructed Fourier-space filter to extra only the information from the fringes. f) The log-scaled absolute component of the Fourier transform of the Fourier-space fringe-only filtered fringe image. The Fourier transforms shown are for one phase shifted image, but results are representative.

5.3.6 Quality of phase data

There were multiple issues with the phase data produced by the measurement system. Even though single rows of phase data could be unwrapped successfully with the Itoh method, there was underlying phase noise that was significantly larger than any underlying phase variation due to changes in height on the powder bed, see Figure 5.18. The source of the high harmonic noise in the images is unclear and the Fourier filtering required to remove the unwanted frequencies would compromise the height measurements derived from such filtered data.

The general curve seen in the phase difference plots in Figure 5.18 was also seen in phase data of a flat chequerboard target laid down on the build chamber bed. This indicates that the distortion parameters of the projector were not well constrained during calibration. The first distortion parameter in the Brown model [210] is a quadratic term and accounts for the majority of the distortion in the image so it is likely that the first parameter was poorly optimised for.

5.3.7 Phase unwrapping results

Figure 5.19 shows the technique of number theory phase unwrapping as applied to the phase derived from filtered images. Whilst only using the 'fringe-only' filtered images removed the high frequency noise in the phase, it did not prevent issues with number theory unwrapping. Whilst the plateaus of LUT values were mostly straight, they did not have constant value and that combined with offsets from their correct values led to unwrapping errors. For comparison, the unfiltered phase equivalent can be seen in Figure 5.21. Figure 2.12 shows the idealised version of LUT values with level steps at each new novel combination of high frequency and low frequency phases. Because of the high phase noise seen in Figure 5.21, an error

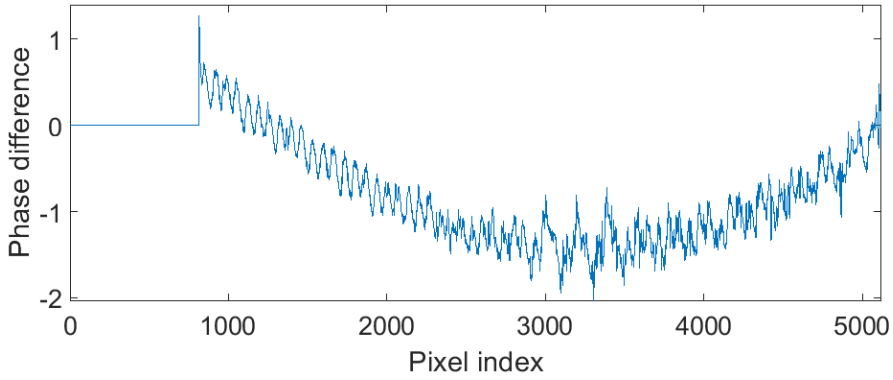

(a) Difference in phase between the Itoh unwrapped phase for the featured row and a straight line of equal inclination. Spatial period of oscillation was approximately 30 pixels, whereas a high frequency fringe period was approximately 200 pixels.

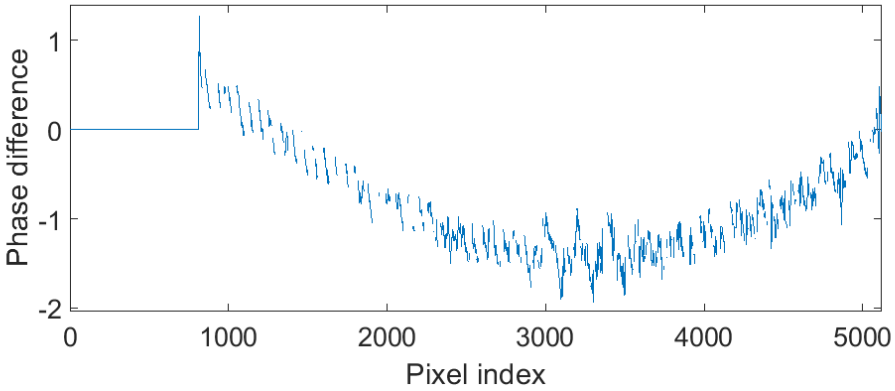

(b) Same data as Figure 5.18a, after the removal of all the pixels where at least one of the high frequency phase shifts was over saturated for the pixel.

Figure 5.18. Underlying phase noise in captured data. Data is from the same row as highlighted in Section 5.3.5.

correcting algorithm was tested, but it produced worse unwrapped phase maps. The error correction technique recognised the planar nature of the surface, and that the fringe orders are mostly monotonic in the direction of the fringes. Therefore, of the multiple LUT solutions that fit the noisy data there could be an unambiguous unique solution that minimises large jumps in fringe order between neighbouring regions. Unfortunately, even when region analysis is performed to label each unique plateau, the level of phase noise is too high. The effect of the high phase noise is to make erroneous LUT solutions appear to fit the data as equally well as the correct unwrapping answer. It is possible that further analysis could be implemented to extract some meaningful point clouds from the data. However, it would require local (spatial) unwrapping analysis and the high proportion of over exposed data would make this challenging. Also, the high levels of phase noise demonstrated in Figure 5.18a mean that removing phase noise at the demonstrated frequencies is likely to strip away information contained in the images. Therefore the data is not suitable for either long scale or short scale analysis.

Figure 5.22 shows the masked image of the number theory LUT values. The masking was calculated by finding all pixels where at least one fringe pattern intensity was within 4 intensity levels of the maximum possible unsigned 10-bit number (1024). The Fourier filtered images were checked by calculating a one dimensional Fourier transform of a row from near the middle of the image. The comparison of spectra before and after filtering can be seen in Figure 5.23, with a significant reduction in the first and largest harmonic peak seen.

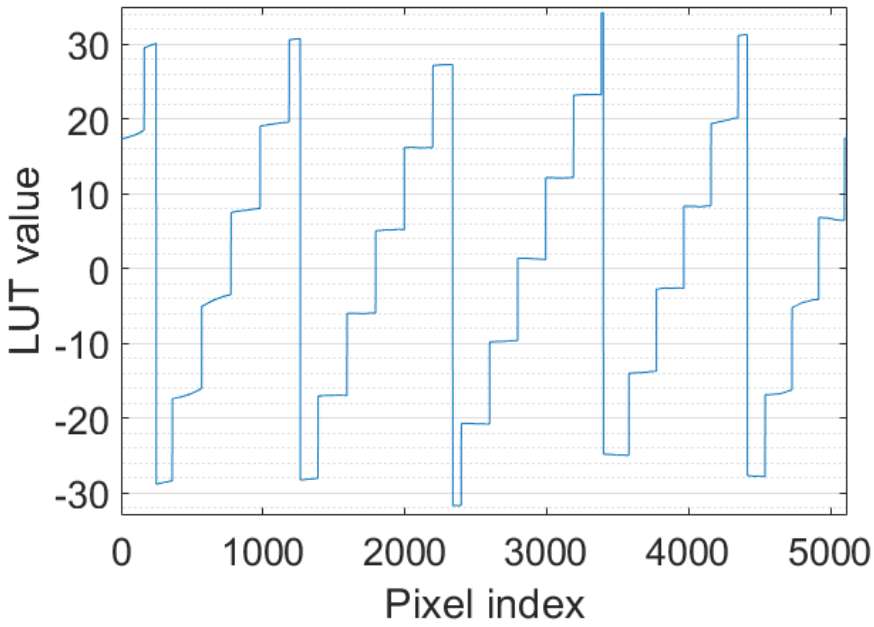

Figure 5.19. Number theory phase unwrapping with experimental data, filtered in Fourier-space. Each plateau should be of a constant value, ideally centred around the exact integer value in the LUT.

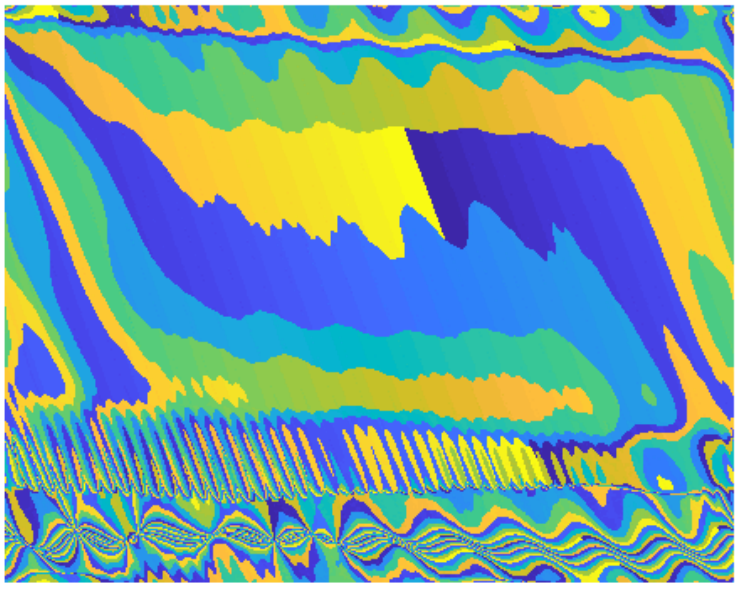

Figure 5.20. Image of number theory phase unwrapping with experimental data, filtered in Fourier-space. Whilst there are regions where number theory phase unwrapping is successful (regions of similar colour), this is not consistent across the powder bed.

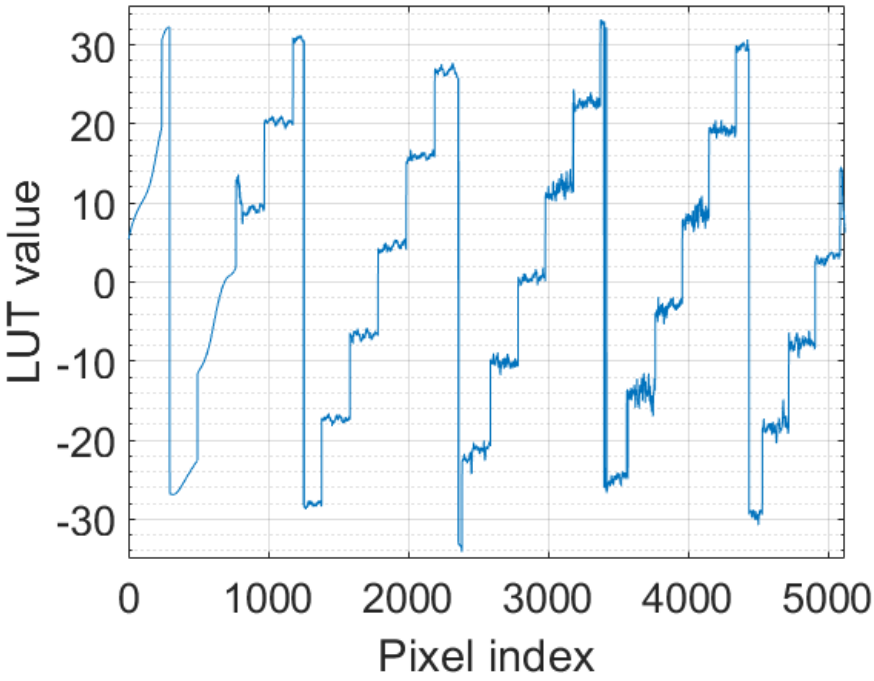

Figure 5.21. Number theory phase unwrapping with experimental data, not filtered in Fourier-space. This data is from the powder stroke of the same layer as .The phase noise.

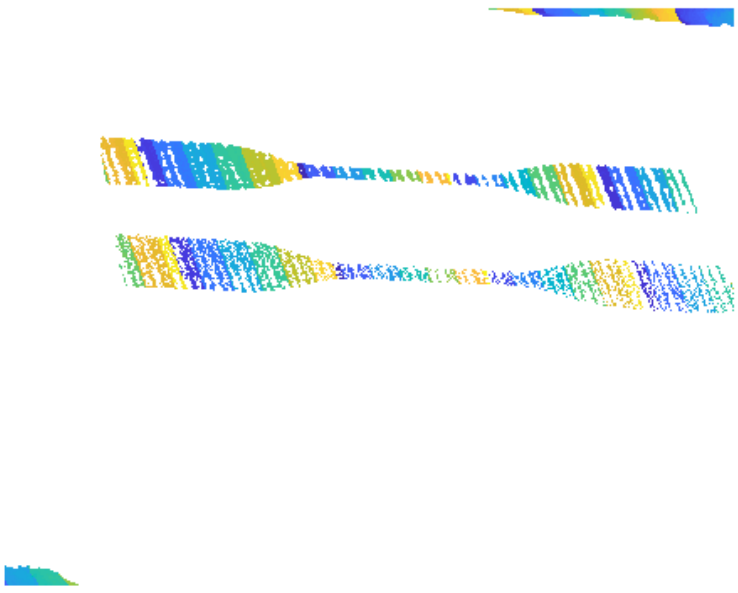

Figure 5.22. Image of number theory phase unwrapping with experimental data, not filtered in Fourier-space. The regions .

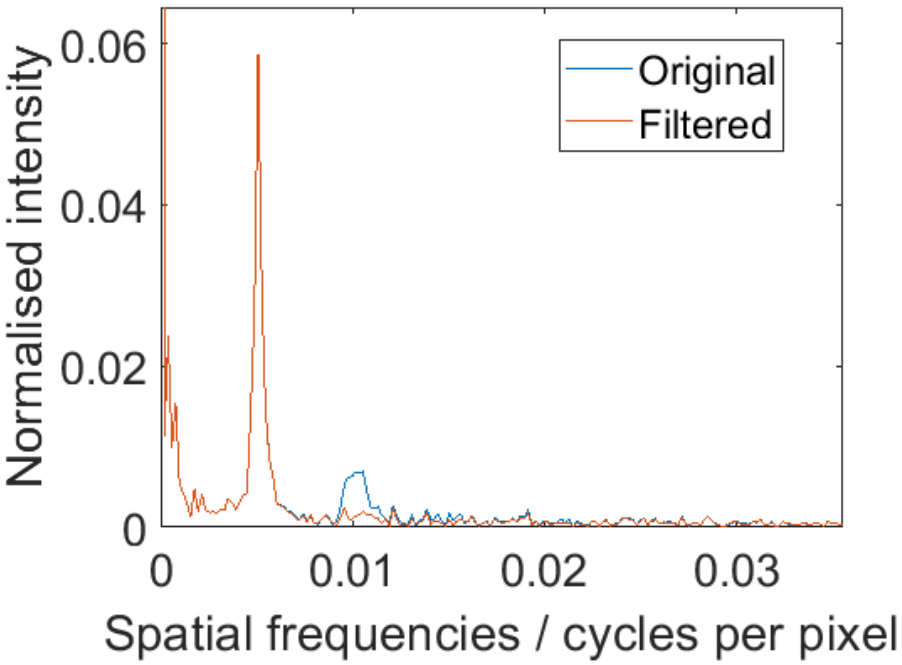

Figure 5.23. Fourier spectral comparison before and after frequency space filtering. The first harmonic peak at approximately 0.01 cycles per pixel is effectively suppressed by the frequency space filtering of the captured images. This data is from the powder spreading stroke of layer 343 of the build, which was the first layer of stack 7.

5.3.8 Point cloud measurements

When the phase maps were converted into point clouds, they had an average point spacing on the powder bed of 30 µm $\pm$ 19 µm, with $k = 1$ coverage. Point cloud measurements are not presented because the phase unwrapping was not successful, and there were several issues with phase noise obscuring the underlying data from the powder bed surface.

5.4 Discussion

Ultimately, the lack of opportunity to design the phase encoding approach around the experimental data led to poor quality data that could not be used to calculate process signatures. However, HSS has been shown to be a viable candidate for fringe projection in-process monitoring and insights into process specific challenges have been gained.

5.4.1 Calibration

The difficulty in obtaining the calibration for the system was partly due to the poor depth of focus across the build chamber. Without a change of monitoring viewpoint, it is possible that a more bespoke calibration routine is needed for the fringe projection monitoring system. The 24 phase step sinusoidal fringe projection methods used did not eliminate erroneous phase jumps in the calibration data collection. There was a remaining radially symmetric distortion in the point clouds of the powder bed suggesting poorly fitted calibration. This is likely a poorly calibrated k1 term since it is a quadratic radial distortion term. This would be improved with a larger depth of focus, less noisy chequerboard data, and, perhaps, a calibration using the powder bed build base as a precision lead screw in one direction.

The calibration was hampered by the mismatched fields of view of the camera and projector. The camera only viewed the central portion of the projector's field of view giving poor constraints for the calibration optimisation process. If the field of views of both camera and projector could be better matched it might lead to a more accurate calibration, which would support more accurate measurements. A future improvement could be to calibrate the camera separately through a greater field of view. Then the camera's calibrated parameters could be fixed before repeating calibration for the whole system solving for the projector's calibration parameters and the relative poses of the two systems.

Despite the difficulty in obtaining a calibration, the produced point cloud was correctly scaled and orientated. Another possible improvement to the calibration routine would use the powder bed to translate the calibration artefact into a wider range of positions, providing a dense sampling of calibration object poses throughout the measurement volume. However, this would significantly increase the processing and memory requirements for calculating the camera and projector intrinsic and extrinsic matrices. It is also possible that the extra measurements required to increase the calibration robustness would fall far away from the plane of focus. This would make fringe projections measurements difficult and more likely to have errors in unwrapping, reducing the effectiveness of the calibration procedure.

5.4.2 Fringe pattern errors

A significant number of layers had at least one partial pattern error due to either a projection error or over saturation. The over saturation was possibly due to the projector's light source varying in intensity during the course of the build. It was not observed during calibration or overnight tests so it is unclear why the brightness of the bulb varied so significantly during

measurements. Because the projection errors are clearly visible in images taken with a 0.5 s exposure, it suggests the image being supplied to the projector was at fault. This is because the DLP projector's native refresh rate was 120 Hz and the supplied video signal from the Raspberry Pi was 60 Hz, meaning a 0.5 s exposure was taken over tens of projector refresh cycles. Therefore any initial refresh issues would cause small illumination variations due to the long exposure of the camera.

5.4.3 Fringe projection challenges

A main limiting factor for the fringe projection measurements was the noise in the calculated, wrapped, phase maps. This was caused by having small numbers of phase shifts for the data collection and having a small aperture limiting the amount of light entering the camera. This meant the unwrapping algorithm was unable to correctly unwrap the phase maps. It is clear that a monitoring system such as the one demonstrated requires an iterative approach to selecting the best phase encoding scheme because it is very difficult to predict phase noise levels without taking real-world measurements.

Despite the tilt lens being used on the camera, only a thin strip of the front tensile test specimen was fully in focus across the powder bed. This had the effect of reducing the resolution of the measurement system away from the horizontal strip of focus. A smaller sensor size, a smaller aperture or a shorter focal length could improve the depth of focus but they would respectively increase phase noise (or reduce the number of pixels), reduce the incoming light (increasing phase noise) or reduce the usable region of the images captured. Given the numerous other issues with the collected data, this improvement would not be relevant until the data collected had fewer phase artefacts.

5.4.4 Variation within the HSS build

It is common for the bottom layers of a polymer PBF to include sacrificial parts [16]. The mechanical results from the first pair of tensile test specimens demonstrate why this is needed, see Figure 5.13. The first parts built are likely to experience a colder powder bed when consolidating since there is no residual heat from previously consolidated parts below them. Drop due to consolidation would be a good candidate for detecting such issues in-process. However, the dark, and therefore cold, region seen in Figure 5.10 does not explain the consistently worse mechanical performance of tensile test specimens built towards the front of the build chamber. Further investigation would be required to confirm if a thermal gradient between the front and back of the build bed was the cause of the improved mechanical properties at the back of the build chamber.

The infrared images also show cold powder dropped from the powder spreading system during sintering. Occasionally this cold powder would fall on the consolidated region, a potential cause of porosity in the final part. However, the apparently random additions of cold powder to the consolidated regions did not seem to strongly influence the mechanical properties. This could be because the cold powder was dropped after consolidation had finished, making minimal difference to the spreading of the next layer of powder and subsequent consolidation.

5.4.5 Future improvements

Monitoring the powder bed from above would be the most obvious and possibly simplest improvement. Although this would require a different PBF system, a bespoke system with the fringe projector and camera designed into the system would eliminate many of the difficulties of data collection and post-processing encountered in this study. Another benefit would be to

reduce vibrations caused by the acceleration and deceleration of the powder recoating mechanism.

The presented in-process measurements would benefit from: a stronger signal; a brighter projector with greater contrast combined with a camera with higher sensitivity to incoming light; lower noise, reduced stray light and fewer specular surfaces close to the measured surfaces. These improvements would reduce the phase noise in the phase maps, leading to fewer errors in phase unwrapping. A projector designed for metrology applications would also reduce potential sources of phase noise, instead of a consumer grade projector. This would also reduce the drift in brightness of the projected patterns, as well as improve the ability to load patterns and synchronise their projection with the camera taking images. A selection of phase encoding schemes could also be trialled, along with improving a priori information that can be used during phase unwrapping to reduce ambiguity.

Assuming the issues regarding optical access and the quality of collected data can be overcome with a bespoke system, there remain the problems associated with the speed of data processing and large volumes of data to be collected and then generated during analysis. With further development, it is expected that GPU acceleration could enable both point cloud generation and analysis. If in-process analysis was achieved, then communication between the monitoring system and the polymer PBF system would allow for closed loop in-process control and therefore a much greater impact on the manufacturing process. If speed of process feedback is most important, a less capable phase unwrapping technique such as Fourier unwrapping could be used [211, 212]. This could provide information on powder bed surface irregularities, but the lack of absolute reference height would mean that some process signatures such as drop due to consolidation might not be measureable. However, simpler process signatures such as detecting debris might be better measured with techniques such as camera based

differential lighting and machine learning processing.

With further development, the presented system is capable of high speed measurements of the consolidated regions of the powder bed and therefore their rates of consolidation. This could inform the selection of optimum processing parameters as well as providing the first in-process measurements of the rate of polymer powder consolidation since Steinberger et al. [40]. The camera used can capture at higher frame rates if the region of interest is smaller than the full resolution of 5120 px $\times$ 5120 px. If captured at a colour depth of 10 bits, a 200 px $\times$ 200 px region of interest (6 mm $\times$ 6 mm area on the powder bed) can be captured at a maximum rate of 58.3 frames per second. This rises to 115.1 frames per second if only 8 bit colour depth is used. Whilst the projector has a native frame rate of 120 frames per second, the brightness of the projected image on the powder bed would have to be increased significantly for the shorter exposure times needed for high speed capture.

5.5 Conclusion

HSS presents unique challenges for powder bed monitoring because of the high contrast between the consolidated regions and the surrounding powder bed. Fringe projection has been shown to be an in-process monitoring technique capable of detecting both defects and process status in laser PBF. However, the dark consolidated regions of HSS provide difficult measurement conditions for attempting to replicate the success of fringe projection in LS. Fringe projection provides the possibility of high quality measurements of the in-process geometry of the polymer powder bed that is unlikely to be significantly improved upon by a different technique. This is because coaxial monitoring is not possible in HSS, due to the lack of a scanning energy beam. A HSS system with fringe projection in-process

monitoring equipment built into its design would solve many of the problems described in this chapter, and would bring in-process monitoring of HSS closer to a commercial reality.

Chapter 6

General discussion and Conclusion

6.1 General discussion

In-process fringe projection measurements of the polymer PBF powder bed have provided insights into the polymer consolidation process. This shows that the measurement technique has the potential for further integration into polymer PBF, and suggestions for future work have been made. The combined results of Chapter 4 and Chapter 5 provide several insights and indicate the direction of future work.

The fact that the evolution of drop due to consolidation did not fit the expected geometric series proposed by Zhang et al. [106], see section 4.2.2, shows that the full melting assumption of metal PBF might not hold in all polymer PBF situations. Computer simulations could be used to explore which properties of the polymer melt control the evolution of drop due to consolidation. For example, it is possible that the boundary between consolidated and unconsolidated powder is gradual enough to break the assumption that all layers consolidate equally, made by the model of Zhang

et al. Simulations could predict the presence of such gradual boundaries, and their impact on the measured drop due to consolidation.

The observation of heaping of powder at the edges of parts before hatched consolidation, shows the effects that previously consolidated material can have on the layer being processed. Because the border scan consolidation had occurred before the powder bed surface had been measured it is unclear what the exact mechanisms that drove the heaping were. Understanding these interactions is very important because even small cumulative interactions can have large impacts over builds with thousands of layers.

The infrared images of the powder bed in Chapter 5 demonstrate the need for thermal monitoring to be part of any in-process monitoring of the polymer PBF process because they contained information that was not possible to collect with a surface form measurement. The positioning of the part towards the right hand side of the build area was to avoid curling build failures caused by the powder bed being too cold towards the left hand edge of the build chamber. This colder region could be seen in the uncalibrated infrared images. Whilst fringe projection, or another geometrical monitoring technique, can detect process errors caused by such temperature issues, they cannot directly monitor the cause of such process issues.

Comparisons of HSS and polymer laser PBF have previously been constrained to mechanical properties of parts produced [75]. Unfortunately, the results of Chapter 5 cannot be compared to those in Chapter 4, because of the phase unwrapping errors when processing data collected from the HSS system. The main cause of the phase unwrapping errors was high levels of noise in the calculated phase maps, the source of which is unknown. However, fringe projection has been shown to be a candidate for such comparative investigations between related processes in the future. Both in-process measurement solutions did not interrupt the process for

measurements and the results in Chapter 4 showed the detection of a failure before it happened. A comparison of the fidelity of part geometries produced could identify if the very different heating mechanisms translate into different accuracies. Going beyond current performances, it is clear that increased in-process monitoring and eventually in-process control will be incorporated into PBF systems, and fringe projection is a clear candidate for such integrations. A direct measure of drop due to consolidation is the only measurement quantity described in literature than can measure the process signatures needed to compensate for excess z dimension consolidation. Fringe projection can be used to measure this drop due to consolidation and it can also detect in-plane consolidation errors that require correcting. This dynamic correction of process variability is especially important as both polymer and metal PBF are increasingly used for production runs of end-use parts. With further improvements (see section 6.1.1), in-process fringe projection measurements of the polymer PBF powder bed could provide a unique ability to probe the fundamental dynamics of polymer PBF in real-world processing conditions.

The greatest challenge faced when performing the in-process measurements of polymer PBF powder beds was data processing and analysis. Not only does it take significant computing power to process point clouds from the many layers in a typical polymer PBF build, the data produced can require large amounts of storage space. For example, one fully monitored build (as described in Chapter 5) produced 500 GB of images, 100 GB of point cloud data and approximately 2 TB of intermediate data. This does not include the in-process thermal images and the temperature monitoring information for the system that were collected separately by the PBF system. The Nub3D used a 1.5 Mpixel camera to produce point clouds with 300 000 points. Despite this the processing times and storage requirements were still significant. A partial solution to the large volumes of data could be to

segment the captured images to only process pixels that belong to the build region of the powder. To reduce the data processed further, it would be possible to use a-priori information, of where the powder bed will be consolidated on every layer, to only measure the heights of the consolidated regions. This would require the detecting of powder spreading defects to be of low priority since the the powder bed surface would not be measured in such a situation. Long term storage of the data produced, or more likely the analysis of the data, is desirable for long term trend analysis as well as for part quality certification purposes. Minimising the economic impact of such storage is a high priority for future integration of in-process monitoring into industrial polymer PBF.

There are many in-process monitoring techniques that have been demonstrated in PBF, and their varying data outputs are unlikely to be as easy to compare and contrast as the more common surface metrology techniques such as CSI or FV [213, 214]. Therefore, high resolution geometric in-process monitoring of the powder bed surface could provide a vital reference measurement for other in-process monitoring techniques. An alternative to a reference measurement would be a standardised reference artefact that could be measured ex-situ with techniques such as CSI. Such an artefact has not been described in literature, and the need for a powder bed analogue to be included would complicate the design and construction.

6.1.1 Future research

The analysis of the in-process monitoring data has shown it is possible to probe the polymer consolidation dynamics as well as providing information for in-process control.

Further investigation of the polymer consolidation dynamics would require a brighter projector to enable higher speed data capture, possibly up

to tens of frames per second. Investigations enabled by such measurements would include the variation in consolidation between different polymers, the influence of the rate of energy delivery on consolidation and the effect of consolidation using multiple exposures. To the best of the author's knowledge, such measurements would be the first since Steinberger et al.'s report in 1999 [40]. Combining in-process and post-process measurements would enable correlation studies such as those by Thompson et al. [215].

Making the presented fringe projection techniques suitable for real-time in-process monitoring and in-process control would require substantial increases in processing speed and acquisition rate. GPU processing could be applied to temporal phase unwrapping techniques, but high resolution imaging such as in Chapter 5 could still overwhelm modern hardware. It is expected that significant processing optimisation would also be required to improve the data processing rate. If the desired pitch of measurements on the powder bed was as low as the Nub3D configuration presented in Chapter 4, significant processing speed improvements could be realised. Reducing the amount of data collected would have a large effect throughout the whole chain of data processing and analysis. This could be achieved by only processing pixels in the images that correspond to the region of the powder bed that can be built in. A more complex data reduction strategy could be to only process the areas in the image that contain consolidated powder. Beyond reducing the amount of data needing to be processed, high performance computing hardware could also improve some of the processing times.

Designing an fringe projection data collection procedure optimised for in-process monitoring is essential for obtaining the most valuable in-process insights possible. Not only do the hardware and optics require tailoring to the measurement situation, the fringe projection analysis has to be robust to the levels of phase noise produced by the system whilst also collecting

and processing the data fast enough. Real-time data analysis of the powder bed point clouds has not been demonstrated, and it is expected that this will become a research priority as high bandwidth in-process monitoring systems are increasingly integrated into industrial PBF systems [105]. Progress in high speed point cloud analysis will also benefit post-process measurement systems, which are already commonly used. The high contrast seen in the HSS powder bed was an example of the variations between different PBF systems that could require radically different monitoring solutions to obtain suitable fringe projection data from the process. It is also likely that the most detailed insights into a process might not be required for all PBF fusion systems, so lower resolution and cheaper measurement systems could be developed for wider deployment as warning systems of build failure. In contrast a high resolution monitoring system would likely be utilised on systems processing new or difficult to process materials.

The greatest utility of in-process monitoring with fringe projection would be to provide real-time feedback on process state. This would allow for the development of in-process control system with a deep level of process awareness. If a control algorithm had process maps such as Figure 4.5 and Figure 4.6 anticipatory algorithm modifications to process parameters could be made to optimise processing outcomes based on process state information. Another potential application of real-time feedback would be for automated process mapping. This would consist of many coupon builds being built and and managed by a system's in-process control routine. If a coupon's process signatures indicated it was going to fail, or would complete but with insufficient part properties, the build of that coupon could be cancelled and a new coupon with more favourable processing parameters. In this way, the routine could determine a process map much faster than an experienced machine user and it could be quickly established for any new material, which is a significant investment of time if testing and developing

new materials for a system. Finally, this process insight is not limited to treating a whole part as one monolithic set of process parameters. High quality in-process monitoring allows for the detection of the process state in different regions of a part, such as a thin wall section compared to a large fully dense region. This increases the design freedom for producing additively manufactured parts, whilst potentially improving the performance of existing designs being produced. Whilst a technique similar to this has been demonstrated with thermal imaging [96], modifications were applied to layers as a whole and did not tailor processing parameters to each regions of a part.

Given the recent descriptions of polymer projection PBF [75, 95], it could be possible to develop a polymer PBF system that both consolidated and monitored with the same energy source. Because of the early development stage of both processes, it is unlikely to be feasible in the short term. However, there would be unique processing and control strategies enabled by such a system. For example, during consolidation, the system could continue energy delivery until the desired drop due to consolidation is measured.

For all the reasons outlined in this section, in-process monitoring of PBF with fringe projection could have significant economic benefits. Reduced build failures, optimised build parameters and increased dimensional control of parts are just some of the potential benefits of successful integration of a system in a commercial PBF system. With PBF increasingly being used for wider applications it is clear that in-process monitoring, especially the high resolution powder bed monitoring demonstrated here, has the potential to significantly improve the economic case for PBF production even for large batch production of parts.

6.2 Conclusion

- In-process monitoring of the geometry of the polymer powder bed has been shown to quantify the progress of consolidation through measuring the drop due to consolidation;
- In-process monitoring of the geometry of the polymer powder bed has been shown to predict the occurrence of future process issues, by detecting when the maximum height above the powder bed increases above acceptable levels;
- The fringe projection measurements of process state are suitable for input into in-process control because of the large magnitude changes when the process state becomes undesirable and the measurements do not have to interrupt the process to measure it;
- In-process signatures were resolved with enough detail to identify some process failures before they happened;
- Real-time fringe projection measurements and analysis would require significant improvements in the speed of data processing, the calibration routine, and potentially the speed of acquisition. This would improve the suitability of fringe projection for industrial in-process monitoring of polymer PBF.

References

[1] N. Hopkinson and P. Erasenthiran. ‘Method and apparatus for combining particulate material’. U.S. pat. 7879282B2. L. U. E. Ltd. 2011.

[2] *Additive manufacturing. General principles. Terminology*. BS EN ISO/ASTM 52900:2017. ISO, 2017.

[3] G. Boothroyd. *Fundamentals of Metal Machining and Machine Tools, Third Edition*. CRC Press, 1988. 566 pp.

[4] E. Atzeni, L. Iuliano, G. Marchiandi, P. Minetola, A. Salmi, E. Bassoli, L. Denti and A. Gatto. ‘Additive manufacturing as a cost-effective way to produce metal parts’. In: *High Value Manufacturing: Advanced Research in Virtual and Rapid Prototyping*. Ed. by P. da Silva Bártolo, A. de Lemos, A. Pereira, A. Mateus, C. Ramos, C. Santos, D. Oliveira, E. Pinto, F. Craveiro, H. da Rocha Terreiro Galha Bártolo, H. de Amorim Almeia, I. Sousa, J. Matias, L. Durão, M. Gaspar, N. Fernandes Alves, P. Carreira, T. Ferreira and T. Marques. CRC Press, 2013, pp. 3–8.

[5] P. A. Kobryn, N. R. Ontko, L. P. Perkins and J. S. Tiley. ‘Additive Manufacturing of Aerospace Alloys for Aircraft Structures’. In: *Cost Effective Manufacture via Net-Shape Processing*. Meeting Proceedings RTO-MP-AVT-139, Paper 3. Neuilly-sur-Seine, France: RTO. Air Force Research Lab Wright-patterson Afb Oh Materials and Manufacturing Directorate, 2006, pp. 3–1 – 3–14.

[6] B. T. Astrom. *Manufacturing of Polymer Composites*. CRC Press, 1997. 500 pp.

[7] R. Huang, M. Riddle, D. Graziano, J. Warren, S. Das, S. Nimbalkar, J. Cresko and E. Masanet. ‘Energy and emissions saving potential of additive manufacturing: the case of lightweight aircraft components’. *Journal of Cleaner Production* 135 (2016), pp. 1559–1570.

[8] A. R. Studart. ‘Additive manufacturing of biologically-inspired materials’. *Chem. Soc. Rev.* 45.2 (2016), pp. 359–376.

[9] C. G. Sandström. ‘The non-disruptive emergence of an ecosystem for 3D Printing — Insights from the hearing aid industry’s transition 1989–2008’. *Technological Forecasting and Social Change* 102 (2016), pp. 160–168.

[10] M. Baumers, P. Dickens, C. Tuck and R. Hague. 'The cost of additive manufacturing: machine productivity, economies of scale and technology-push'. *Technological Forecasting and Social Change* 102 (2016), pp. 193–201.

[11] A. Uriondo Del Pozo. 'Development of a qualification procedure, and quality assurance and quality control concepts and procedures for repairing and reproducing parts with additive manufacturing in MRO processes'. PhD thesis. 2015.

[12] *Additive manufacturing. Design. Requirements, guidelines and recommendations*. International Standard 52910:2018. ISO, 2018, p. 32.

[13] C. R. Deckard. 'Method and apparatus for producing parts by selective sintering'. U.S. pat. 4863538A. U. of Texas System. 1989.

[14] T. Grimm. *User's Guide to Rapid Prototyping*. Society of Manufacturing Engineers, 2004. 423 pp.

[15] R. Liu, Z. Wang, T. Sparks, F. Liou and J. Newkirk. '13 - Aerospace applications of laser additive manufacturing'. In: *Laser Additive Manufacturing*. Ed. by M. Brandt. Woodhead Publishing Series in Electronic and Optical Materials. Woodhead Publishing, 2017, pp. 351–371.

[16] R. D. Goodridge, C. J. Tuck and R. J. M. Hague. 'Laser sintering of polyamides and other polymers'. *Progress in Materials Science* 57.2 (2012), pp. 229–267.

[17] Materialgeeza. *SLS system schematic*. bibtex: PBFimage. URL: `https://commons.wikimedia.org/wiki/File:Selective_laser_melting_system_schematic.jpg` (visited on 22/05/2016).

[18] Y. Shi, Z. Li, H. Sun, S. Huang and F. Zeng. 'Effect of the properties of the polymer materials on the quality of selective laser sintering parts'. *Proceedings of the IMechE* 218.3 (2004), pp. 247–252.

[19] D. L. Bourell, T. J. Watt, D. K. Leigh and B. Fulcher. 'Performance limitations in polymer laser sintering'. *Physics Procedia*. 8th International Conference on Laser Assisted Net Shape Engineering LANE 2014 56 (2014), pp. 147–156.

[20] C. Majewski, H. Zarringhalam and N. Hopkinson. 'Effect of the degree of particle melt on mechanical properties in selective laser-sintered Nylon-12 parts'. *Proceedings of the IMechE* 222.9 (2008), pp. 1055–1064.

[21] N. Hopkinson and P. Erasenthiran. 'High Speed Sintering – Early Research into a New Rapid Manufacturing Process'. In: *Proceedings of the Solid Freeform Fabrication Symposium*. Solid Freeform Fabrication Symposium. Austin, Texas, 2004, p. 9.

[22] H. R. Thomas, N. Hopkinson and P. Erasenthiran. 'High Speed Sintering - Continuing research into a new Rapid Manufacturing process'. In: *Proc. Solid Freeform Fabrication Symposium*. Solid Freeform Fabrication Symposium. Austin, TX, 2006, p. 10.

[23] K. Dotchev and W. Yusoff. 'Recycling of polyamide 12 based powders in the laser sintering process'. *Rapid Prototyping Journal* 15.3 (2009), pp. 192–203.

[24] *HP 3D printing materials*. HP Development Company, L.P, 2018, p. 12.

[25] M. Grasso and B. M. Colosimo. 'Process defects and in situ monitoring methods in metal powder bed fusion: a review'. *Meas. Sci. Technol.* 28.4 (2017), p. 044005.

[26] S. K. Everton, M. Hirsch, P. Stravroulakis, R. K. Leach and A. T. Clare. 'Review of in-situ process monitoring and in-situ metrology for metal additive manufacturing'. *Materials & Design* 95 (2016), pp. 431–445.

[27] S. P. Soe, D. R. Eyers and R. Setchi. 'Assessment of non-uniform shrinkage in the laser sintering of polymer materials'. *Int J Adv Manuf Technol* 68.1 (2013), pp. 111–125.

[28] M. Vasquez, B. Haworth and N. Hopkinson. 'Methods for quantifying the stable sintering region in laser sintered polyamide-12'. *Polym. Eng. Sci.* 53.6 (2013), pp. 1230–1240.

[29] A. Wegner, G. Witt and S. C. Jana. 'Understanding the decisive thermal processes in laser sintering of polyamide 12'. *AIP Conference Proceedings* 1664.1 (2015), p. 160004.

[30] P. Peyre, Y. Rouchausse, D. Defauchy and G. Régnier. 'Experimental and numerical analysis of the selective laser sintering (SLS) of PA12 and PEKK semi-crystalline polymers'. *Journal of Materials Processing Technology* 225 (2015), pp. 326–336.

[31] O. R. Ghita, E. James, R. Trimble and K. E. Evans. 'Physico-chemical behaviour of Poly (Ether Ketone) (PEK) in High Temperature Laser Sintering (HT-LS)'. *Journal of Materials Processing Technology* 214.4 (2014), pp. 969–978.

[32] J. P. Kruth, G. Levy, F. Klocke and T. H. C. Childs. 'Consolidation phenomena in laser and powder-bed based layered manufacturing'. *CIRP Annals - Manufacturing Technology* 56.2 (2007), pp. 730–759.

[33] M. Vasquez, B. Haworth and N. Hopkinson. 'Optimum sintering region for laser sintered nylon-12'. *Proceedings of the Institution of Mechanical Engineers, Part B: Journal of Engineering Manufacture* 225.12 (2011), pp. 2240–2248.

[34] J. T. Rimell and P. M. Marquis. 'Selective laser sintering of ultra high molecular weight polyethylene for clinical applications'. *Journal of Biomedical Materials Research* 53.4 (2000), pp. 414–420.

[35] J. Frenkel. 'Viscous flow of crystalline bodies under the action of surface tension'. *Journal of Physics, Publication House of the Academy of Sciences of the USSR* 9.5 (1945), pp. 385–391.

[36] A. J. Shaler. 'Seminar on the kinetics of sintering'. *JOM* 1.11 (1949), pp. 796–813.

[37] C. T. Bellehumeur, M. Kontopoulou and J. Vlachopoulos. ‘The role of viscoelasticity in polymer sintering’. *Rheol. Acta* 37.3 (1998), pp. 270–278.

[38] O. Pokluda, C. T. Bellehumeur and J. Vlachopoulos. ‘Modification of Frenkel’s model for sintering’. *AIChE Journal* 43.12 (1997), pp. 3253–3256.

[39] C. Balemans, M. Hulsen, P. Anderson, C. Balemans, M. A. Hulsen and P. D. Anderson. ‘Sintering of Two Viscoelastic Particles: A Computational Approach’. *Applied Sciences* 7.5 (2017), p. 516.

[40] J. Steinberger, K. Manetsberger, J. Shen and J. Müllers. ‘Measurement of the Sintering Dynamics of polymeric powders at Near SLS Conditions’. In: *Proc. Solid Freeform Fabrication Symposium*. Austin, Texas, 1999, p. 8.

[41] B. Haworth, N. Hopkinson, D. Hitt and X. Zhong. ‘Shear viscosity measurements on Polyamide-12 polymers for laser sintering’. *Rapid Prototyping Journal* 19.1 (2013), pp. 28–36.

[42] T. G. Spears and S. A. Gold. ‘In-process sensing in selective laser melting (SLM) additive manufacturing’. *Integr. Mater. Manuf. Innov.* 5.1 (2016), pp. 1–25.

[43] M. Hirsch, R. Patel, W. Li, G. Guan, R. K. Leach, S. D. Sharples and A. T. Clare. ‘Assessing the capability of in-situ nondestructive analysis during layer based additive manufacture’. *Additive Manufacturing* 13 (2017), pp. 135–142.

[44] D. K. Leigh. ‘A comparison of polyamide 11 mechanical properties between laser sintering and traditional molding’. In: *Proceedings of the Solid Freeform Fabrication Symposium*. Austin, TX, 2012.

[45] T. Stichel, T. Frick, T. Laumer, F. Tenner, T. Hausotte, M. Merklein and M. Schmidt. ‘A Round Robin study for Selective Laser Sintering of polyamide 12: Microstructural origin of the mechanical properties’. *Optics & Laser Technology* 89 (2017), pp. 31–40.

[46] M. Pavan, T. Craeghs, J.-P. Kruth and W. Dewulf. ‘Understanding the laser sinterting of polymers at microscale level by using X-ray computed tomography’. In: *Proceedings of the Solid Freeform Fabrication Symposium*. Solid Freeform Fabrication 2016. Austin, TX, 2016.

[47] John D. Williams and Carl R. Deckard. ‘Advances in modeling the effects of selected parameters on the SLS process’. *Rapid Prototyping Journal* 4.2 (1998), pp. 90–100.

[48] B. K. Foster, E. W. Reutzel, A. R. Nassar, B. T. Hall, S. W. Brown and C. J. Dickman. ‘Optical, layerwise monitoring of powder bed fusion’. In: *Proceedings of the Solid Freeform Fabrication Symposium*. Austin, TX, 2015.

[49] G. Galimberti, E. L. Doubrovski, M. Guagliano, B. Previtali and J. C. Verlinden. 'Investigating the links between the process parameters and their influence on the aesthetic evaluation of selective laser melted parts'. In: *27th Annual International Solid Freeform Fabrication Symposium*. 2016, pp. 2367–2387.

[50] H. Zarringhalam, N. Hopkinson, N. F. Kamperman and J. J. de Vlieger. 'Effects of processing on microstructure and properties of SLS Nylon 12'. *Materials Science and Engineering: A* 435-436 (2006), pp. 172–180.

[51] C. L. Lewis, K. Stewart and M. Anthamatten. 'The Influence of Hydrogen Bonding Side-Groups on Viscoelastic Behavior of Linear and Network Polymers'. *Macromolecules* 47.2 (2014), pp. 729–740.

[52] T. J. Gornet, K. R. Davis, D. T. L. Starr and K. M. Mulloy. 'Characterization of Selective Laser Sintering Materials to Determine Process Stability'. In: *Proceedings of the Solid Freeform Fabrication Symposium*. Solid Freeform Fabrication Symposium. 2002, p. 8.

[53] M. Launhardt, A. Wörz, A. Loderer, T. Laumer, D. Drummer, T. Hausotte and M. Schmidt. 'Detecting surface roughness on SLS parts with various measuring techniques'. *Polymer Testing* 53 (2016), pp. 217–226.

[54] M. A. Beard, O. R. Ghita and K. E. Evans. 'Using Raman spectroscopy to monitor surface finish and roughness of components manufactured by selective laser sintering'. *J. Raman Spectrosc.* 42.4 (2011), pp. 744–748.

[55] G. de Oliveira Setti, M. Fernandes de Oliveira, I. Alves Maia, J. Vicente Lopes da Silva, R. Savu and E. Joanni. 'Correlation between mechanical and surface properties of SLS parts'. *Rapid Prototyping Journal* 20.4 (2014), pp. 285–290.

[56] G. Guan, M. Hirsch, Z. H. Lu, D. T. D. Childs, S. J. Matcher, R. Goodridge, K. M. Groom and A. T. Clare. 'Evaluation of selective laser sintering processes by optical coherence tomography'. *Materials & Design* 88 (2015), pp. 837–846.

[57] M. Grasso, V. Laguzza, Q. Semeraro and B. M. Colosimo. 'In-Process Monitoring of Selective Laser Melting: Spatial Detection of Defects Via Image Data Analysis'. *J. Manuf. Sci. Eng* 139.5 (2016), pp. 051001–051001–16.

[58] M. Berzins, T. H. C. Childs, K. W. Dalgarno, G. R. Ryder and G. Stein. 'Densification and distortion in selective laser sintering of polycarbonate'. In: *Proceedings of the solid freeform fabrication symposium*. Vol. 6. 1995, pp. 196–203.

[59] R. D. Goodridge, R. J. M. Hague and C. J. Tuck. 'An empirical study into laser sintering of ultra-high molecular weight polyethylene (UHMWPE)'. *Journal of Materials Processing Technology* 210.1 (2010), pp. 72–80.

[60] B. Partee, S. J. Hollister and S. Das. 'Selective laser sintering process optimization for layered manufacturing of capa® 6501 polycaprolactone bone tissue engineering scaffolds'. *J. Manuf. Sci. Eng.* 128.2 (2005), pp. 531–540.

[61] N. Raghunath and P. M. Pandey. 'Improving accuracy through shrinkage modelling by using Taguchi method in selective laser sintering'. *International Journal of Machine Tools and Manufacture* 47.6 (2007), pp. 985–995.

[62] S. Moylan, A. Cooke, K. Jurrens, J. Slotwinski and M. A. Donmez. *A review of test artifacts for additive manufacturing*. NISTIR 7858. Gaithersburg, MD: National Institute of Standards and Technology (NIST), 2012.

[63] J. Allison, C. Sharpe and C. C. Seepersad. 'Powder bed fusion metrology for additive manufacturing design guidance'. *Additive Manufacturing* (2018).

[64] *Additive Manufacturing Simulation | Netfabb Features | Autodesk*. 2018. URL: https://www.autodesk.co.uk/products/netfabb/features/simulation (visited on 26/11/2018).

[65] *Additive Works - Simulation-based Process Software for Laser Beam Melting*. 2018. URL: https://additive.works/ (visited on 26/11/2018).

[66] *Additive Manufacturing | ANSYS*. 2018. URL: https://www.ansys.com/en-gb/products/structures/additive-manufacturing (visited on 26/11/2018).

[67] I. Flores Ituarte, E. Huotilainen, O. Wiikinkoski and J. Tuomi. 'Experiments With Machine Vision For Polymer Flowability Analysis In Powder Bed Fusion'. In: *Proc. Of the 3rd Intl. Conf. on Progress in Additive Manufacturing (Pro-AM 2018)*. Progress in Additive Manufacturing. Singapore: Nanyang Technological University, 2018, pp. 401–406.

[68] S. Yang and J. R. G. Evans. 'Metering and dispensing of powder; the quest for new solid freeforming techniques'. *Powder Technology* 178.1 (2007), pp. 56–72.

[69] T. L. Starr, T. J. Gornet and J. S. Usher. 'The effect of process conditions on mechanical properties of laser-sintered nylon'. *Rapid Prototyping Journal* 17.6 (2011), pp. 418–423.

[70] B. Caulfield, P. E. McHugh and S. Lohfeld. 'Dependence of mechanical properties of polyamide components on build parameters in the SLS process'. *Journal of Materials Processing Technology* 182.1 (2007), pp. 477–488.

[71] N. Kumar, H. Kumar and J. S. Khurmi. 'Experimental investigation of process parameters for rapid prototyping technique (selective laser sintering) to enhance the part quality of prototype by taguchi method'. *Procedia Technology*. 3rd International Conference on Innovations in Automation and Mechatronics Engineering 2016, ICIAME 2016 05-06 February, 2016 23 (2016), pp. 352–360.

[72] *Standard Test Method for Tensile Properties of Plastics ASTM D638-14*. West Conshohocken, PA: ASTM International, 2014.

[73] C. Kamath. 'Data mining and statistical inference in selective laser melting'. *Int J Adv Manuf Technol* 86.5 (2016), pp. 1659–1677.

[74] *HP Multi Jet Fusion technology*. Technical white paper. HP Development Company, L.P, 2018, p. 8.

[75] G. Craft, J. Nussbaum, N. Crane and J. P. Harmon. 'Impact of extended sintering times on mechanical properties in PA-12 parts produced by powderbed fusion processes'. *Additive Manufacturing* 22 (2018), pp. 800–806.

[76] M. Mani, B. M. Lane, M. A. Donmez, S. C. Feng, S. P. Moylan and R. R. F. Jr. 'Measurement science needs for real-time control of additive manufacturing powder bed fusion processes'. *NIST Interagency/Internal Report (NISTIR) - 8036* (2015).

[77] M. Seifi, A. Salem, J. Beuth, O. Harrysson and J. J. Lewandowski. 'Overview of Materials Qualification Needs for Metal Additive Manufacturing'. *JOM* 68.3 (2016), pp. 747–764.

[78] *Senvol ML*. Senvol. URL: http://senvol.com/ml/ (visited on 24/09/2018).

[79] M. Thomas, G. J. Baxter and I. Todd. 'Normalised model-based processing diagrams for additive layer manufacture of engineering alloys'. *Acta Materialia* 108 (2016), pp. 26–35.

[80] H. Gong, K. Rafi, H. Gu, T. Starr and B. Stucker. 'Analysis of defect generation in Ti–6Al–4V parts made using powder bed fusion additive manufacturing processes'. *Additive Manufacturing*. Inaugural Issue 1-4 (2014), pp. 87–98.

[81] B. M. Gopalsamy, B. Mondal and S. Ghosh. 'Taguchi method and ANOVA: An approach for process parameters optimization of hard machining while machining hardened steel'. *Journal of Scientific & Industrial Research* 68 (2009), pp. 686–695.

[82] S. Rama Rao and G. Padmanabhan. 'Application of Taguchi methods and ANOVA in optimization of process parameters for metal removal rate in electrochemical machining of Al/5%SiC composites'. *International Journal of Engineering Research and* 2.3 (2012), p. 6.

[83] İ. Asiltürk, S. Neşeli and M. A. İnce. 'Optimisation of parameters affecting surface roughness of Co28Cr6Mo medical material during CNC lathe machining by using the Taguchi and RSM methods'. *Measurement* 78 (2016), pp. 120–128.

[84] W. E. King, A. T. Anderson, R. M. Ferencz, N. E. Hodge, C. Kamath, S. A. Khairallah and A. M. Rubenchik. 'Laser powder bed fusion additive manufacturing of metals; physics, computational, and materials challenges'. *Applied Physics Reviews* 2.4 (2015), p. 041304.

[85] Renishaw. *InfiniAM Spectral schematic - simple: software laser powder bed fusion additive manufacturing metal*. 2018. URL: https://resources.renishaw.com/en/details/infiniam-spectral-schematic-simple--99581 (visited on 21/12/2018).

[86] D. Miller, C. Deckard and J. Williams. 'Variable beam size SLS workstation and enhanced SLS model'. *Rapid Prototyping Journal* 3.1 (1997), pp. 4–11.

[87] J. C. Nelson, N. K. Vail and J. W. Barlow. 'Laser sintering model for composite materials'. In: *Proceedings of the Solid Freeform Fabrication Symposium*. Austin, TX, 1993.

[88] D. B. Hann, J. Iammi and J. Folkes. 'A simple methodology for predicting laser-weld properties from material and laser parameters'. *J. Phys. D: Appl. Phys.* 44.44 (2011), p. 445401.

[89] W. E. King, H. D. Barth, V. M. Castillo, G. F. Gallegos, J. W. Gibbs, D. E. Hahn, C. Kamath and A. M. Rubenchik. 'Observation of keyhole-mode laser melting in laser powder-bed fusion additive manufacturing'. *Journal of Materials Processing Technology* 214.12 (2014), pp. 2915–2925.

[90] T. Purtonen, A. Kalliosaari and A. Salminen. 'Monitoring and adaptive control of laser processes'. *Physics Procedia*. 8th International Conference on Laser Assisted Net Shape Engineering LANE 2014 56 (2014), pp. 1218–1231.

[91] P. Stavropoulos, D. Chantzis, C. Doukas, A. Papacharalampopoulos and G. Chryssolouris. 'Monitoring and Control of Manufacturing Processes: A Review'. *Procedia CIRP*. 14th CIRP Conference on Modeling of Machining Operations (CIRP CMMO) 8 (2013), pp. 421–425.

[92] R. Teti, K. Jemielniak, G. O'Donnell and D. Dornfeld. 'Advanced monitoring of machining operations'. *CIRP Annals* 59.2 (2010), pp. 717–739.

[93] N. Ambhore, D. Kamble, S. Chinchanikar and V. Wayal. 'Tool Condition Monitoring System: A Review'. *Materials Today: Proceedings*. 4th International Conference on Materials Processing and Characterzation 2.4 (2015), pp. 3419–3428.

[94] Z. Li, X. Liu, S. Wen, P. He, K. Zhong, Q. Wei, Y. Shi and S. Liu. 'In Situ 3D Monitoring of Geometric Signatures in the Powder-Bed-Fusion Additive Manufacturing Process via Vision Sensing Methods'. *Sensors* 18.4 (2018), p. 1180.

[95] J. Nussbaum and N. B. Crane. 'Evaluation of processing variables in polymer projection sintering'. *Rapid Prototyping Journal* 24.5 (2018), pp. 880–885.

[96] M. Abdelrahman and T. L. Starr. 'Feedforward control for polymer laser sintering process using part geometry'. In: *Proceedings of the Solid Freeform Fabrication Symposium*. Austin, TX, 2015.

[97] A. Wegner and G. Witt. ‘Process monitoring in laser sintering using thermal imaging’. In: *Proceedings of the Solid Freeform Fabrication Symposium*. Austin, TX, 2011, pp. 8–10.

[98] B. Zhang, M. Duemmler, L. Sripragash, O. Adewumi, A. Davies, J. Ziegert, C. Waters and C. Evans. ‘Detection of Subsurface Defect for Metal Additive Manufacturing Using Flash Thermography’. In: 2018 ASPE and euspen Summer Topical Meeting. Berkeley, USA, 2018, p. 6.

[99] B. A. Fisher, B. Lane, H. Yeung and J. Beuth. ‘Toward determining melt pool quality metrics via coaxial monitoring in laser powder bed fusion’. *Manufacturing Letters*. Industry 4.0 and Smart Manufacturing 15 (2018), pp. 119–121.

[100] S. Clijsters, T. Craeghs, S. Buls, K. Kempen and J.-P. Kruth. ‘In situ quality control of the selective laser melting process using a high-speed, real-time melt pool monitoring system’. *Int J Adv Manuf Technol* 75.5 (2014), pp. 1089–1101.

[101] P. Lott, H. Schleifenbaum, W. Meiners, K. Wissenbach, C. Hinke and J. Bültmann. ‘Design of an optical system for the in situ process monitoring of selective laser melting (slm)’. *Physics Procedia*. Lasers in Manufacturing 2011 - Proceedings of the Sixth International WLT Conference on Lasers in Manufacturing 12, Part A (2011), pp. 683–690.

[102] C. Gobert, E. W. Reutzel, J. Petrich, A. R. Nassar and S. Phoha. ‘Application of supervised machine learning for defect detection during metallic powder bed fusion additive manufacturing using high resolution imaging.’ *Additive Manufacturing* 21 (2018), pp. 517–528.

[103] M. Abdelrahman, E. W. Reutzel, A. R. Nassar and T. L. Starr. ‘Flaw detection in powder bed fusion using optical imaging’. *Additive Manufacturing* 15 (2017), pp. 1–11.

[104] *.quality management*. 2018. URL: https://www.concept-laser.de/en/products/quality-management.html (visited on 19/11/2018).

[105] A. Dickins, T. Widjanarko, S. Lawes, P. Stravroulakis and R. Leach. ‘Design of a Multi-Sensor in-Situ Inspection System for Additive Manufacturing’. In: *Proc. ASPE/euspen Advancing Precision in Additive Manufacturing*. Berkeley, USA, 2018, p. 6.

[106] B. Zhang, J. Ziegert, F. Farahi and A. Davies. ‘In situ surface topography of laser powder bed fusion using fringe projection’. *Additive Manufacturing* 12, Part A (2016), pp. 100–107.

[107] A. Neef, V. Seyda, D. Herzog, C. Emmelmann, M. Schönleber and M. Kogel-Hollacher. ‘Low coherence interferometry in selective laser melting’. *Physics Procedia*. 8th International Conference on Laser Assisted Net Shape Engineering LANE 2014 56 (2014), pp. 82–89.

[108] P. J. DePond, G. Guss, S. Ly, N. P. Calta, D. Deane, S. Khairallah and M. J. Matthews. 'In situ measurements of layer roughness during laser powder bed fusion additive manufacturing using low coherence scanning interferometry'. *Materials & Design* 154 (2018), pp. 347–359.

[109] D. Kouprianoff, N. Luwes, E. Newby, I. Yadroitsava and I. Yadroitsev. 'On-line monitoring of laser powder bed fusion by acoustic emission: Acoustic emission for inspection of single tracks under different powder layer thickness'. In: *2017 Pattern Recognition Association of South Africa and Robotics and Mechatronics (PRASA-RobMech)*. 2017 Pattern Recognition Association of South Africa and Robotics and Mechatronics (PRASA-RobMech). 2017, pp. 203–207.

[110] D. Ye, G. S. Hong, Y. Zhang, K. Zhu and J. Y. H. Fuh. 'Defect detection in selective laser melting technology by acoustic signals with deep belief networks'. *Int J Adv Manuf Technol* 96.5 (2018), pp. 2791–2801.

[111] S. Everton, P. Dickens, C. Tuck and B. Dutton. 'Using Laser Ultrasound to Detect Subsurface Defects in Metal Laser Powder Bed Fusion Components'. *JOM* 70.3 (2018), pp. 378–383.

[112] R. Patel, M. Hirsch, P. Dryburgh, D. Pieris, S. Achamfuo-Yeboah, R. Smith, R. Light, S. Sharples, A. Clare, M. Clark, R. Patel, M. Hirsch, P. Dryburgh, D. Pieris, S. Achamfuo-Yeboah, R. Smith, R. Light, S. Sharples, A. Clare and M. Clark. 'Imaging Material Texture of As-Deposited Selective Laser Melted Parts Using Spatially Resolved Acoustic Spectroscopy'. *Applied Sciences* 8.10 (2018), p. 1991.

[113] A. Thompson, N. Senin and R. K. Leach. 'Towards an Additive Surface Atlas'. In: ASPE/euspen Conf. Dimensional Accuracy and Surface Finish in Additive Manufacturi. Rayleigh, NC, USA, 2016, p. 6.

[114] F. Cabanettes, A. Joubert, G. Chardon, V. Dumas, J. Rech, C. Grosjean and Z. Dimkovski. 'Topography of as built surfaces generated in metal additive manufacturing: A multi scale analysis from form to roughness'. *Precision Engineering* 52 (2018), pp. 249–265.

[115] A. Thompson, N. Senin, I. Maskery, L. Körner, S. Lawes and R. Leach. 'Internal surface measurement of metal powder bed fusion parts'. *Additive Manufacturing* 20 (2018), pp. 126–133.

[116] A. Townsend, R. Racasan, R. Leach, N. Senin, A. Thompson, A. Ramsey, D. Bate, P. Woolliams, S. Brown and L. Blunt. 'An interlaboratory comparison of X-ray computed tomography measurement for texture and dimensional characterisation of additively manufactured parts'. *Additive Manufacturing* 23 (2018), pp. 422–432.

[117] S. Carmignato, W. Dewulf and R. Leach, eds. *Industrial X-Ray Computed Tomography*. Springer International Publishing, 2018.

[118] C. L. A. Leung, S. Marussi, R. C. Atwood, M. Towrie, P. J. Withers and P. D. Lee. 'In situ X-ray imaging of defect and molten pool dynamics in laser additive manufacturing'. *Nature Communications* 9.1 (2018), p. 1355.

[119] P. Bidare, R. R. J. Maier, R. J. Beck, J. D. Shephard and A. J. Moore. 'An open-architecture metal powder bed fusion system for in-situ process measurements'. *Additive Manufacturing* 16 (2017), pp. 177–185.

[120] L. Newton, N. Senin and R. Leach. 'Focus Variation Measurement of Metal Additively Manufactured Surfaces'. In: *Proc. ASPE/euspen Advancing Precision in Additive Manufacturing*. ASPE/euspen Advancing Precision in Additive Manufacturing. Berkeley, USA, 2018, p. 6.

[121] C. Gomez, R. Su, A. Thompson, J. DiSciacca, S. Lawes and R. K. Leach. 'Optimization of surface measurement for metal additive manufacturing using coherence scanning interferometry'. *OE* 56.11 (2017), p. 111714.

[122] J. A. Kanko, A. P. Sibley and J. M. Fraser. 'In situ morphology-based defect detection of selective laser melting through inline coherent imaging'. *Journal of Materials Processing Technology* 231 (2016), pp. 488–500.

[123] G. Guan, M. Hirsch, W. P. Syam, R. K. Leach, Z. Huang and A. T. Clare. 'Loose powder detection and surface characterization in selective laser sintering via optical coherence tomography'. *Proc Math Phys Eng Sci* 472.2191 (2016).

[124] A. Lewis, M. Gardner, A. McElroy, T. Milner, S. Fish and J. Beaman. 'In-Situ Process Monitoring and Ex-Situ Part Quality Assessment of Selective Laser Sintering Using Optical Coherence Tomography'. In: *Proc. Solid Freeform Fabrication Symposium*. Solid Freeform Fabrication Symposium. Austin, TX, 2016, p. 15.

[125] A. Lewis, N. Katta, A. McElroy, T. Milner, S. Fish and J. Beaman. 'Investigation of Optical Coherence Tomography Imaging in Nylon 12 Powder'. In: *Proc. Solid Freeform Fabrication Symposium*. Solid Freeform Fabrication Symposium. Austin, Texas, 2017, p. 12.

[126] S. E. MEng. 'Ensuring the quality of components produced by metal additive manufacturing using laser generated ultrasound'. PhD thesis. Nottingham: University of Nottingham, 2017. 286 pp.

[127] L. Claes, T. Meyer, F. Bause, J. Rautenberg and B. Henning. 'Determination of the material properties of polymers using laser-generated broadband ultrasound'. *Journal of Sensors and Sensor Systems* 5.1 (2016), pp. 187–196.

[128] M. Dubois, P. W. Lorraine, R. J. Filkins and T. E. Drake. 'Experimental comparison between optical spectroscopy and laser-ultrasound generation in polymer-matrix composites'. *Appl. Phys. Lett.* 79.12 (2001), pp. 1813–1815.

[129] L. Scime and J. Beuth. ‘A multi-scale convolutional neural network for autonomous anomaly detection and classification in a laser powder bed fusion additive manufacturing process’. *Additive Manufacturing* 24 (2018), pp. 273–286.

[130] M. J. Matthews, G. Guss, S. A. Khairallah, A. M. Rubenchik, P. J. Depond and W. E. King. ‘Denudation of metal powder layers in laser powder bed fusion processes’. *Acta Materialia* 114 (2016), pp. 33–42.

[131] U. Scipioni Bertoli, G. Guss, S. Wu, M. J. Matthews and J. M. Schoenung. ‘In-situ characterization of laser-powder interaction and cooling rates through high-speed imaging of powder bed fusion additive manufacturing’. *Materials & Design* 135 (2017), pp. 385–396.

[132] B. Yuan, G. M. Guss, A. C. Wilson, S. P. Hau-Riege, P. J. DePond, S. McMains, M. J. Matthews and B. Giera. ‘Machine-Learning-Based Monitoring of Laser Powder Bed Fusion’. *Advanced Materials Technologies* (2018).

[133] K. A. Mumtaz and N. Hopkinson. ‘Selective Laser Melting of thin wall parts using pulse shaping’. *Journal of Materials Processing Technology* 210.2 (2010), pp. 279–287.

[134] Y. Zhang, G. S. Hong, D. Ye, K. Zhu and J. Y. H. Fuh. ‘Extraction and evaluation of melt pool, plume and spatter information for powder-bed fusion AM process monitoring’. *Materials & Design* 156 (2018), pp. 458–469.

[135] A. N. D. Gasper, B. Szost, X. Wang, D. Johns, S. Sharma, A. T. Clare and I. A. Ashcroft. ‘Spatter and oxide formation in laser powder bed fusion of Inconel 718’. *Additive Manufacturing* 24 (2018), pp. 446–456.

[136] M. Grasso, A. G. Demir, B. Previtali and B. M. Colosimo. ‘In situ monitoring of selective laser melting of zinc powder via infrared imaging of the process plume’. *Robotics and Computer-Integrated Manufacturing* 49 (2018), pp. 229–239.

[137] C. Barrett, E. MacDonald, B. Conner and F. Persi. ‘Micron-Level Layer-Wise Surface Profilometry to Detect Porosity Defects in Powder Bed Fusion of Inconel 718’. *JOM* 70.9 (2018), pp. 1844–1852.

[138] Y. Zhang, J. Y. H. Fuh, D. Ye and G. S. Hong. ‘In-situ Monitoring of Laser-based PBF via off-axis Vision and Image Processing Approaches’. *Additive Manufacturing* (2018).

[139] O. Faugeras. *Three-dimensional Computer Vision: A Geometric Viewpoint*. MIT Press, 1993. 700 pp.

[140] C. Restif, C. Ibáñez-Ventoso, M. M. Vora, S. Guo, D. Metaxas and M. Driscoll. ‘CeleST: Computer Vision Software for Quantitative Analysis of C. elegans Swim Behavior Reveals Novel Features of Locomotion’. *PLOS Computational Biology* 10.7 (2014), e1003702.

[141] E. H. W. Meijering, W. J. Niessen, J. P. W. Pluim and M. A. Viergever. 'Quantitative Comparison of Sinc-Approximating Kernels for Medical Image Interpolation'. In: *Medical Image Computing and Computer-Assisted Intervention – MICCAI'99*. Ed. by C. Taylor and A. Colchester. Lecture Notes in Computer Science. Springer Berlin Heidelberg, 1999, pp. 210–217.

[142] I. Aicardi, F. Chiabrando, A. Maria Lingua and F. Noardo. 'Recent trends in cultural heritage 3D survey: The photogrammetric computer vision approach'. *Journal of Cultural Heritage* 32 (2018), pp. 257–266.

[143] D. Sims-Waterhouse, P. Bointon, S. Piano and R. K. Leach. 'Experimental comparison of photogrammetry for additive manufactured parts with and without laser speckle projection'. In: *Optical Measurement Systems for Industrial Inspection X*. Optical Measurement Systems for Industrial Inspection X. Vol. 10329. International Society for Optics and Photonics, 2017, 103290W.

[144] *Monitoring TruPrint*. URL: https://www.trumpf.com/de_INT/produkte/services/services-maschinen-systeme-und-laser/monitoring-analyse/monitoring-truprint/ (visited on 17/11/2018).

[145] G. Stephanopoulos and C. Han. 'Intelligent systems in process engineering: a review'. *Computers & Chemical Engineering*. Fifth International Symposium on Process Systems Engineering 20.6 (1996), pp. 743–791.

[146] Y. LeCun, Y. Bengio and G. Hinton. 'Deep learning'. *Nature* 521.7553 (2015), pp. 436–444.

[147] D. Shen, G. Wu and H.-I. Suk. 'Deep Learning in Medical Image Analysis'. *Annual Review of Biomedical Engineering* 19.1 (2017), pp. 221–248.

[148] D. Ciresan, U. Meier, J. Masci and J. Schmidhuber. 'Multi-Column Deep Neural Network for Traffic Sign Classification'. *Neural Networks* (2012), pp. 1–15.

[149] D. Silver, J. Schrittwieser, K. Simonyan, I. Antonoglou, A. Huang, A. Guez, T. Hubert, L. Baker, M. Lai, A. Bolton, Y. Chen, T. Lillicrap, F. Hui, L. Sifre, G. v. d. Driessche, T. Graepel and D. Hassabis. 'Mastering the game of Go without human knowledge'. *Nature* 550.7676 (2017), p. 354.

[150] F. Imani, A. Gaikwad, M. Montazeri, P. Rao, H. Yang and E. Reutzel. 'Process Mapping and In-Process Monitoring of Porosity in Laser Powder Bed Fusion Using Layerwise Optical Imaging'. *J. Manuf. Sci. Eng* 140.10 (2018), pp. 101009–101009–14.

[151] L. Scime and J. Beuth. 'Using machine learning to identify in-situ melt pool signatures indicative of flaw formation in a laser powder bed fusion additive manufacturing process'. *Additive Manufacturing* 25 (2019), pp. 151–165.

[152] D. Ye, J. Y. Hsi Fuh, Y. Zhang, G. S. Hong and K. Zhu. 'In situ monitoring of selective laser melting using plume and spatter signatures by deep belief networks'. *ISA Transactions* 81 (2018), pp. 96–104.

[153] T. Karras, T. Aila, S. Laine and J. Lehtinen. 'Progressive Growing of GANs for Improved Quality, Stability, and Variation'. In: *arXiv:1710.10196 [cs, stat]*. ICLR 2018. 2018.

[154] D. Maturana and S. Scherer. 'VoxNet: A 3D Convolutional Neural Network for Real-Time Object Recognition'. In: *2015 IEEE/RSJ International Conference on Intelligent Robots and Systems (IROS)*. 2015 IEEE/RSJ International Conference on Intelligent Robots and Systems (IROS). Hamburg, Germany: IEEE, 2015, pp. 922–928.

[155] M. Grasso, F. Gallina and B. M. Colosimo. 'Data fusion methods for statistical process monitoring and quality characterization in metal additive manufacturing'. *Procedia CIRP*. The 15th CIRP Conference on Computer Aided Tolerancing, CIRP CAT 2018, 11-13 June 2018, Milan, Italy 75 (2018), pp. 103–107.

[156] J. Williams, P. Dryburgh, A. Clare, P. Rao and A. Samal. 'Defect Detection and Monitoring in Metal Additive Manufactured Parts through Deep Learning of Spatially Resolved Acoustic Spectroscopy Signals'. *Smart and Sustainable Manufacturing Systems* 2.1 (2018), p. 20180035.

[157] Z. Zhang. 'Microsoft Kinect Sensor and Its Effect'. *IEEE MultiMedia* 19.2 (2012), pp. 4–10.

[158] K. Khoshelham and S. O. Elberink. 'Accuracy and Resolution of Kinect Depth Data for Indoor Mapping Applications'. *Sensors* 12.2 (2012), pp. 1437–1454.

[159] S. S. Gorthi and P. Rastogi. 'Fringe projection techniques: Whither we are?' *Optics and Lasers in Engineering*. Fringe Projection Techniques 48.2 (2010), pp. 133–140.

[160] L. Huang, Q. Kemao, B. Pan and A. K. Asundi. 'Comparison of Fourier transform, windowed Fourier transform, and wavelet transform methods for phase extraction from a single fringe pattern in fringe projection profilometry'. *Optics and Lasers in Engineering* 48.2 (2010), pp. 141–148.

[161] M. Takeda and K. Mutoh. 'Fourier transform profilometry for the automatic measurement of 3-D object shapes'. *Appl. Opt., AO* 22.24 (1983), pp. 3977–3982.

[162] S. Zhang. *High-Speed 3D Imaging with Digital Fringe Projection Techniques*. CRC Press, 2016. 218 pp.

[163] C. Zuo, L. Huang, M. Zhang, Q. Chen and A. Asundi. 'Temporal phase unwrapping algorithms for fringe projection profilometry: A comparative review'. *Optics and Lasers in Engineering* 85 (2016), pp. 84–103.

[164] M. A. Herráez, D. R. Burton, M. J. Lalor and M. A. Gdeisat. 'Fast two-dimensional phase-unwrapping algorithm based on sorting by reliability following a noncontinuous path'. *Appl. Opt., AO* 41.35 (2002), pp. 7437–7444.

[165] C. Zuo, Q. Chen, G. Gu, S. Feng, F. Feng, R. Li and G. Shen. 'High-speed three-dimensional shape measurement for dynamic scenes using bi-frequency tripolar pulse-width-modulation fringe projection'. *Optics and Lasers in Engineering* 51.8 (2013), pp. 953–960.

[166] J. Zhong and M. Wang. 'Phase unwrapping by lookup table method: application to phase map with singular points'. *OE* 38.12 (1999), pp. 2075–2081.

[167] Y. Ding, J. Xi, Y. Yu, W. Cheng, S. Wang and J. F. Chicharo. 'Frequency selection in absolute phase maps recovery with two frequency projection fringes'. *Optics express* 20.12 (2012), pp. 13238–13251.

[168] P. Stavroulakis, D. Sims-Waterhouse, S. Piano and R. Leach. 'Flexible decoupled camera and projector fringe projection system using inertial sensors'. *OE* 56.10 (2017), p. 104106.

[169] F. Zhu, H. Shi, P. Bai, D. Lei and X. He. 'Nonlinear calibration for generalized fringe projection profilometry under large measuring depth range'. *Appl. Opt., AO* 52.32 (2013), pp. 7718–7723.

[170] S. Zhang. 'Comparative study on passive and active projector nonlinear gamma calibration'. *Appl. Opt., AO* 54.13 (2015), pp. 3834–3841.

[171] G. H. Notni and G. Notni. 'Digital fringe projection in 3D shape measurement: an error analysis'. In: *Optical Measurement Systems for Industrial Inspection III*. Optical Measurement Systems for Industrial Inspection III. Vol. 5144. International Society for Optics and Photonics, 2003, pp. 372–381.

[172] *Geometrical product specifications (GPS). Acceptance and reverification tests for coordinate measuring machines (CMM). CMMs equipped with imaging probing systems*. ISO 10360-7. 2011.

[173] *Optical 3-D measuring systems: Optical systems based on area scanning*. VDI/VDE 2634 Part 2. 2012.

[174] D. Li and J. Kofman. 'Adaptive fringe-pattern projection for image saturation avoidance in 3D surface-shape measurement'. *Opt. Express, OE* 22.8 (2014), pp. 9887–9901.

[175] R. B. Rusu, N. Blodow, Z. C. Marton and M. Beetz. 'Aligning point cloud views using persistent feature histograms'. In: *2008 IEEE/RSJ International Conference on Intelligent Robots and Systems*. 2008 IEEE/RSJ International Conference on Intelligent Robots and Systems. 2008, pp. 3384–3391.

[176] A. V. Segal, D. Haehnel and S. Thrun. 'Generalized-ICP'. *Robotics: science and systems* 2.4 (2009), p. 435.

[177] I. Douros and B. Buxton. ‘Three-dimensional surface curvature estimation using quadric surface patches’. In: *Scanning 2002 Proceedings*. 2002.

[178] E. Kreysig. *Introduction to Differential Geometry and Riemannian Geometry*. 1968.

[179] I. Jovančević, H.-H. Pham, J.-J. Orteu, R. Gilblas, J. Harvent, X. Maurice and L. Brèthes. ‘3D Point Cloud Analysis for Detection and Characterization of Defects on Airplane Exterior Surface’. *J Nondestruct Eval* 36.4 (2017), p. 74.

[180] P. K. Rao, J. (Liu, D. Roberson, Z. (Kong and C. Williams. ‘Online real-time quality monitoring in additive manufacturing processes using heterogeneous sensors’. *J. Manuf. Sci. Eng* 137.6 (2015), pp. 061007–061007–12.

[181] M. L. Vlasea, B. Lane, F. Lopez, S. Mekhontsev and A. Donmez. ‘Development of Powder Bed Fusion Additive Manufacturing Test Bed for Enhanced Real-Time Process Control’. In: *Proceedings of Solid Free Form Fabrication Symposium*. Solid Freeform Fabrication Symposium. 2015, p. 14.

[182] S. Afazov, A. Okioga, A. Holloway, W. Denmark, A. Triantaphyllou, S.-A. Smith and L. Bradley-Smith. ‘A methodology for precision additive manufacturing through compensation’. *Precision Engineering* 50 (2017), pp. 269–274.

[183] M. Hirsch, P. Dryburgh, S. Catchpole-Smith, R. Patel, L. Parry, S. D. Sharples, I. A. Ashcroft and A. T. Clare. ‘Targeted rework strategies for powder bed additive manufacture’. *Additive Manufacturing* 19 (2018), pp. 127–133.

[184] J. A. Benda. ‘Temperature-Controlled Selective Laser Sintering’. In: *Proc. Solid Freeform Fabrication Symposium*. Solid Freeform Fabrication Symposium. 1994, p. 8.

[185] W. W. Wroe, J. Gladstone, T. Phillips, S. Fish, J. Beaman et al. ‘In-situ thermal image correlation with mechanical properties of nylon-12 in SLS’. *Rapid Prototyping Journal* 22.5 (2016), pp. 794–800.

[186] M. Berzins, T. H. C. Childs and G. R. Ryder. ‘The Selective Laser Sintering of Polycarbonate’. *CIRP Annals - Manufacturing Technology* 45.1 (1996), pp. 187–190.

[187] W. King, A. T. Anderson, R. M. Ferencz, N. E. Hodge, C. Kamath and S. A. Khairallah. ‘Overview of modelling and simulation of metal powder bed fusion process at Lawrence Livermore National Laboratory’. *Materials Science and Technology* 31.8 (2015), pp. 957–968.

[188] M. Mani, B. M. Lane, M. A. Donmez, S. C. Feng and S. P. Moylan. ‘A review on measurement science needs for real-time control of additive manufacturing metal powder bed fusion processes’. *International Journal of Production Research* 55.5 (2017), pp. 1400–1418.

[189] J. Mireles, C. Terrazas, S. M. Gaytan, D. A. Roberson and R. B. Wicker. 'Closed-loop automatic feedback control in electron beam melting'. *Int J Adv Manuf Technol* 78.5 (2015), pp. 1193–1199.

[190] M. Abdelrahman and T. L. Starr. 'Quality certification and control of polymer laser sintering: layerwise temperature monitoring using thermal imaging'. *Int. J. Adv. Manuf. Technol.* 84.5 (2015), pp. 831–842.

[191] B. Zhang, A. Davies, J. Ziegert and C. J. Evans. 'Application of the instrument transfer function to a fringe projection system for measuring rough surfaces'. In: Applied Optical Metrology II. Vol. 10373. International Society for Optics and Photonics, 2017, 103730S.

[192] A. Youssef, S. J. Hollister and P. D. Dalton. 'Additive manufacturing of polymer melts for implantable medical devices and scaffolds'. *Biofabrication* 9.1 (2017), p. 012002.

[193] N. Southon, P. Stavroulakis, R. Goodridge and R. Leach. 'In-process measurement and monitoring of a polymer laser sintering powder bed with fringe projection'. *Materials & Design* 157 (2018), pp. 227–234.

[194] A. C. C. Law, N. Southon, N. Senin, P. Stavroulakis, R. Leach, R. Goodridge and Z. Kong. 'Curvature-Based Segmentation of Powder Bed Point Clouds for In-Process Monitoring'. In: *Proceedings of Solid Free Form Fabrication Symposium*. Solid Free Form Fabrication Symposium. Austin, Texas, 2018, p. 15.

[195] *PA2200 Material Data Sheet*. EOS GmbH, 2008, p. 2.

[196] A. Pilipović, B. Valentan and M. Šercer. 'Influence of SLS processing parameters according to the new mathematical model on flexural properties'. *Rapid Prototyping Journal* 22.2 (2016), pp. 258–268.

[197] P. K. Venuvinod and W. Ma. *Rapid Prototyping - Laser-based and Other Technologies*. 1st ed. New York: Springer US, 2004. 390 pp.

[198] S. Josupeit and H.-J. Schmid. 'Three-dimensional in-process temperature measurement of laser-sintered part cakes'. In: *Proceedings of the Solid Freeform Fabrication Symposium*. Austin, TX, 2014, pp. 49–58.

[199] S. Zhang and P. S. Huang. 'Novel method for structured light system calibration'. *Optical Engineering* 45.8 (2006), p. 083601.

[200] B. Li, N. Karpinsky and S. Zhang. 'Novel calibration method for structured-light system with an out-of-focus projector'. *Appl. Opt., AO* 53.16 (2014), pp. 3415–3426.

[201] N. M. Jamal and K. W. Dalgarno. 'Analysis of the influence of viscoelasticity in curl development in sls'. In: *Proceedings of the solid freeform fabrication symposium. Texas: Austin*. Proceedings of the Solid Freeform Fabrication Symposium. Austin, TX, 2002.

[202] N. Otsu. 'A Threshold Selection Method from Gray-Level Histograms'. *IEEE Transactions on Systems, Man, and Cybernetics* 9.1 (1979), pp. 62–66.

[203] C. A. Brown, H. N. Hansen, X. J. Jiang, F. Blateyron, J. Berglund, N. Senin, T. Bartkowiak, B. Dixon, G. Le Goïc, Y. Quinsat, W. J. Stemp, M. K. Thompson, P. S. Ungar and E. H. Zahouani. 'Multiscale analyses and characterizations of surface topographies'. *CIRP Annals* 67.2 (2018), pp. 839–862.

[204] K. P. McAlea, P. F. Forderhase and R. B. Booth. 'Selective laser sintering of polymer powder of controlled particle size distribution'. U.S. pat. 5817206 A. D. Corporation. U.S. Classification 156/272.8, 156/308.4, 264/497, 156/308.2; International Classification B29C67/00, C08J3/12; Cooperative Classification B33Y10/00, C08J2333/06, B29C67/0077, C08J2325/04, B33Y70/00, C08J3/122; European Classification C08J3/12A, B29C67/00R4B. 1998.

[205] H. Zarringhalam. 'Investigation into crystallinity and degree of particle melt in selective laser sintering'. Thesis. Loughborough University, 2007.

[206] M. Abdelrahman and T. L. Starr. 'Layerwise Monitoring of Polymer Laser Sintering Using Thermal Imaging'. In: *Proceedings of Solid Free Form Fabrication Symposium*. Solid Free Form Fabrication Symposium. Austin, Texas, 2014.

[207] N. L. Karpinsky, M. Hoke, V. Chen and S. Zhang. 'High-resolution, real-time three-dimensional shape measurement on graphics processing unit'. *OE, OPEGAR* 53.2 (2014), p. 024105.

[208] H. M. Merklinger. *View Camera Focus*. 1996. URL: `http://www.trenholm.org/hmmerk/HMbook18.html` (visited on 20/12/2018).

[209] L. J. Hornbeck. 'Digital Light Processing for high-brightness high-resolution applications'. In: *Projection Displays III*. Projection Displays III. Vol. 3013. International Society for Optics and Photonics, 1997, pp. 27–41.

[210] D. C. Brown. 'Decentering distortion of lenses'. *Photogrammetric Engineering and Remote Sensing* (1966).

[211] Q. Kemao. 'Windowed Fourier transform for fringe pattern analysis'. *Applied Optics* 43.13 (2004), p. 2695.

[212] U. Paul Kumar, U. Somasundaram, M. P. Kothiyal and N. Krishna Mohan. 'Single frame digital fringe projection profilometry for 3-D surface shape measurement'. *Optik* 124.2 (2013), pp. 166–169.

[213] A. Thompson, N. Senin, C. Giusca and R. Leach. 'Topography of selectively laser melted surfaces: A comparison of different measurement methods'. *CIRP Annals* 66.1 (2017), pp. 543–546.

[214] N. Senin, A. Thompson and R. K. Leach. 'Characterisation of the topography of metal additive surface features with different measurement technologies'. *Meas. Sci. Technol.* 28.9 (2017), p. 095003.

[215] A. Thompson, S. Tammas-Williams, N. Senin and I. Todd. 'Correlating Volume and Surface Features in Additively Manufactured Metal Parts'. In: *Proc. ASPE/euspen Advancing Precision in Additive Manufacturing*. Berkeley, USA, 2018, p. 5.